

Water Chemistry and Corrosion Inhibition in High Pressure CO₂ Corrosion of Mild Steel

A thesis presented to
the faculty of
the College of Arts and Sciences of Ohio University

In partial fulfillment
of the requirements for the degree
Master of Science

Mohd Farid Mohamed

May 2015

© 2015 Mohd Farid Mohamed. All Rights Reserved.

This thesis titled

Water Chemistry and Corrosion Inhibition in High Pressure CO₂ Corrosion of Mild Steel

by

MOHD FARID MOHAMED

has been approved for

the Department of Chemistry and Biochemistry

and the College of Arts and Sciences by

Jeffrey J. Rack

Professor of Chemistry and Biochemistry

Robert Frank

Dean, College of Arts and Sciences

ABSTRACT

MOHAMED, MOHD FARID, M.S., May 2015, Chemistry

Water Chemistry and Corrosion Inhibition in High Pressure CO₂ Corrosion of Mild Steel

Director of Thesis: Jeffrey J. Rack

In the water chemistry part of the present study, the solubility of CO₂ in water, solubility of water in CO₂ and solution pH were measured at 25°C, 40°C and 60°C at partial pressures of CO₂ up to 80 bar. Experiments were set up to validate the water chemistry model for temperatures up to 100°C and pCO₂ up to 600 bar, these were conducted in a 20 liter autoclave equipped for solubility and pH measurements. The water chemistry model developed in this study will be incorporated into a corrosion prediction model for high pCO₂ environments.

In the inhibition part of the present study, two generic corrosion inhibitors were selected: diethylenetriamine imidazoline with and without thiosulfate; these were studied at various concentrations at 70°C and a CO₂ partial pressure of 80 bar. The imidazoline-type corrosion inhibitor was labeled K1 and the imidazoline plus thiosulfate was labeled as K4. The experiments were designed to determine the inhibitive effects at particular inhibitor concentrations as well as the effect of thiosulfate. The experiments were conducted in a 2 liter autoclave equipped for electrochemical measurements. Pitting (localized corrosion) was observed at low concentrations of imidazoline-type inhibitor. At 800 parts per million (ppm) and 1500 ppm, corrosion rates were reduced to 0.8 mm/yr and 0.2 mm/yr from the 18 mm/yr uninhibited corrosion rate, respectively. However, these concentrations are beyond the feasible limits in actual field operations. Addition of

thiosulfate was shown to confer improved inhibitor performance; a corrosion rate of 0.1 mm/yr can be reached by adding only 400ppm of corrosion inhibitor K4.

DEDICATION

To

Nurulhidayah (my wife)

and

Danish Basil and Nuha Amani (my kids)

ACKNOWLEDGMENTS

It is a matter of great privilege for me to express my sincere appreciation and gratitude to my project supervisor Dr. Srdjan Nesic, and to my academic advisor Dr. Jeffrey Rack for their patience and helpfulness under their guidance. They showed their patience and dedication to support me to solve any problem related to coursework and research. Both of them always encouraged me to be a successful researcher.

I owe a great many thanks to my project leader, Mr. Singer for his dedication and attention to assist me in day-to-day work in ICMT and a great many thanks to Dr. Choi for his advice and sharing his expertise that was really useful for my research. A great many thanks go also to Dr. Young for his patience to review this thesis.

I would like to acknowledge all ICMT staff for their assistance in the technical and non-technical work during my tenure in ICMT. I am very thankful to my project members, Azmi, Firdaus and Zaki, for their support in finishing my project and my Masters degree. Again, I thank all my colleagues for their sharing with me in ICMT.

Ultimately, I am very grateful to my beloved parents and my family, who gives enormous moral support and prays for the successful completion of my Masters degree in Ohio University and achievement of my dream.

TABLE OF CONTENTS

	Page
Abstract.....	3
Dedication.....	5
Acknowledgments.....	6
List of Tables	9
List of Figures.....	10
Chapter 1: Introduction.....	23
Background.....	23
Water chemistry in high pressure CO ₂ environments.....	24
Corrosion inhibition in high pressure CO ₂ environments.....	25
Chapter 2: Literature Review.....	27
Water chemistry in high pressure CO ₂ environments.....	27
Corrosion inhibition in high pressure CO ₂ environments.....	30
Chapter 3: Research Objectives and Test Matrices	38
Water chemistry in high pressure CO ₂ environments.....	38
Text matrix.....	39
Corrosion inhibition in high pressure CO ₂ environments.....	39
Test matrix	40
Chapter 4: The Theoretical Background and Modeling.....	43
Dissolution of carbon dioxide.....	44
Carbon dioxide hydration	46
Carbonic acid dissociation	47
Bicarbonate anion dissociation.....	47
Water dissociation.....	48
Electroneutrality.....	48
Speciation of carbonic species.....	48
Electrochemical reaction.....	49
Chapter 5: Experimental Setup and Procedures.....	50
Water chemistry in high pressure CO ₂ environments.....	50
Solubility of CO ₂ in water (xCO ₂).....	50

	8
Solubility of water in CO ₂ (yH ₂ O).....	53
pH of the system	55
Corrosion inhibition in high pressure CO ₂ environment	56
Weight loss test.....	58
Linear polarization resistance (LPR) test.....	59
Electrochemical impedance spectroscopy (EIS) test	60
Potentiodynamic sweep test.....	61
Scanning electron microscopy and energy-dispersive X-ray spectroscopy.....	61
Optical measurement and analysis using infinite focus microscope (IFM).....	61
Chapter 6: Results and Discussions	62
Water chemistry in high pressure CO ₂ environments.....	62
Solubility of CO ₂ in water (xCO ₂).....	62
pH of the system	72
Corrosion inhibition in high pressure CO ₂ environment	75
Baseline experiments	75
Imidazoline-type corrosion inhibitor (K1).....	81
Imidazoline-type corrosion inhibitor plus thiosulfate (K4)	103
Chapter 7: Conclusions	122
Chapter 8: Recommendation for Further Studies	123
References.....	124
Appendix A: Nomenclature	136
Appendix B: Supporting Figures	139

LIST OF TABLES

	Page
Table 1: The properties of corrosion inhibitors K1 and K4.....	37
Table 2: Test parameters for pH measurement and solubility of CO ₂ and water	39
Table 3: Test matrix for corrosion inhibition study	40
Table 4: Chemical composition of the API 5L X65 carbon steel used in this work (mass %, balance Fe).....	42

LIST OF FIGURES

	Page
Figure 1: Formulation of corrosion inhibitor K1	41
Figure 2: Formulation of corrosion inhibitor K4	41
Figure 3: Phase diagram of carbon dioxide.	43
Figure 4: 20 liter high pressure autoclave used in this study	51
Figure 5: Schematic diagram for the solubility of water in CO ₂ and CO ₂ in water experimental set-up	52
Figure 6: Experimental set-up developed to measure the solubility of CO ₂ in water.....	53
Figure 7: Experimental set-up for the measurement of the solubility of water in CO ₂	54
Figure 8: High pressure glass pH probe and Ag/AgCl reference electrode used to measure hydrogen ion (hydronium ion) concentration.	56
Figure 9: 2 liter autoclave equipped for electrochemistry measurements.	57
Figure 10: Specimens for electrochemistry measurement and weight loss.	59
Figure 11: Calculated CO ₂ content in water with partial pressure of CO ₂	62
Figure 12: Calculated H ₂ CO ₃ with partial pressure of CO ₂	63
Figure 13: Calculated HCO ₃ ⁻ with partial pressure of CO ₂	64
Figure 14: Calculated CO ₃ ²⁻ with partial pressure of CO ₂	65
Figure 15: Comparison between experimental results and modeling for the solubility of CO ₂ in water at 25°C	66
Figure 16: Comparison between experimental results and modeling for the solubility of CO ₂ in water at 40°C	67

	11
Figure 17: Comparison between experimental results and modeling for the solubility of CO ₂ in water at 60°C	68
Figure 18: Calculated water content in CO ₂ (gas phases).....	69
Figure 19: Comparison between experimental results and modeling for the solubility of water in CO ₂ at 25°C	70
Figure 20: Comparison between experimental results and modeling for the solubility of water in CO ₂ at 40°C	71
Figure 21: Comparison between experimental results and modeling for the solubility of water in CO ₂ at 60°C	72
Figure 22: Comparison between pH measurements and modeling results at 25°C	73
Figure 23: Comparison between pH measurements and modeling results at 40°C	74
Figure 24: Comparison between pH measurements and modeling results at 60°C	75
Figure 25: Corrosion rate with time by linear polarization resistance at 70°C and 80 bar of CO ₂ in absence of corrosion inhibitor.....	76
Figure 26: Solution resistance (R_s) and polarization resistance (R_p) by electrochemical impedance spectroscopy at 70°C and 80 bar of CO ₂ in absence of corrosion inhibitor. ..	77
Figure 27: Potentiodynamic sweep at 70°C and 80 bar of CO ₂ in absence of corrosion inhibitor.....	78
Figure 28: Surface of weight loss coupon at x1000 magnification for experiment condition of 70°C and 80 bar of CO ₂ in absence of corrosion inhibitor.....	79
Figure 29 : Corrosion product layer composition by EDS at x1000 magnification for experiment condition of 70°C and 80 bar of CO ₂ in absence of corrosion inhibitor.....	80

Figure 30: Surface of weight loss coupon at x1000 magnification after corrosion product was removed by Clarke solution for experiment condition of 70°C and 80 bar of CO ₂ in absence of corrosion inhibitor.....	80
Figure 31 : Composition of bare surface by EDS at x1000 magnification after corrosion product was removed by Clarke solution for experiment condition of 70°C and 80 bar of CO ₂ in absence of corrosion inhibitor.....	81
Figure 32: Corrosion rate with time by linear polarization resistance at 70°C, 80 bar of CO ₂ and various concentrations of corrosion inhibitor K1.....	82
Figure 33: Solution resistance (R _s) and Polarization resistance (R _p) by electrochemical impedance spectroscopy at 70°C, 80 bar of CO ₂ and various concentrations of corrosion inhibitor K1.....	83
Figure 34: Result of potentiodynamic sweep at 70°C, 80 bar pressure of CO ₂ and various concentrations of corrosion inhibitor K1.....	84
Figure 35: Surface of weight loss coupon at x1000 magnification and experiment condition of 70°C, 80 bar of CO ₂ and 50ppm of K1.....	85
Figure 36: Composition of corrosion product layer by EDS at x1000 magnification and experiment condition of 70°C, 80 bar of CO ₂ and 50ppm of K1.....	85
Figure 37: Surface of weight loss coupon at x1000 magnification after corrosion product was removed by Clarke solution and experiment condition of 70°C, 80 bar of CO ₂ and 50ppm of K1.....	86
Figure 38: Composition of bare surface by EDS at x1000 magnification after corrosion product was removed by Clarke solution for experiment condition of 70°C, 80 bar of CO ₂ and 50ppm of K1.....	87

Figure 39: Surface image for experiment condition of 70°C, 80 bar of CO ₂ and 50ppm of K1 and after immersion in Clarke solution.	88
Figure 40: Depth profile of pitting on the steel surface after corrosion product was removed using Clarke solution.	89
Figure 41 : Corrosion Inhibitor K1; Cross-section of pitting using infinite focus microscopy after corrosion product layer was removed using Clarke solution.....	89
Figure 42: Surface of weight loss coupon at x1000 magnification and experiment condition of 70°C, 80 bar of CO ₂ and 100ppm of K1.....	90
Figure 43 : Composition of corrosion product layer by EDS at x1000 magnification and experiment condition of 70°C, 80 bar of CO ₂ and 100ppm of K1.....	91
Figure 44: Surface of weight loss coupon at x1000 magnification after corrosion product layer was removed by Clarke solution and experiment condition of 70°C, 80 bar of CO ₂ and 100ppm of K1.	92
Figure 45: Surface image for experiment condition of 70°C, 80 bar of CO ₂ and 100ppm of K1 after immersion in Clarke solution.	92
Figure 46: Depth profile of pitting on the steel surface after corrosion product layer was removed using Clarke solution.	93
Figure 47: Cross-section of pitting using infinite focus microscopy after film was removed using Clarke solution.	93
Figure 48: Composition of bare surface by EDS at x1000 magnification after corrosion product was removed by Clarke solution and experiment condition of 70°C, 80 bar of CO ₂ and 100ppm of K1.....	94

Figure 49: Surface of weight loss coupon at x1000 magnification and experiment condition of 70°C, 80 bar of CO ₂ and 400ppm of K1.....	95
Figure 50: Composition of corrosion product layer by EDS at x1000 magnification and experiment condition of 70°C, 80 bar of CO ₂ and 400ppm of K1.....	96
Figure 51: Surface of weight loss coupon at x1000 magnification after film was removed by Clarke solution for experiment condition of 70°C, 80 bar of CO ₂ and 400ppm of K1.	96
Figure 52 : Composition of bare surface by EDS at x1000 magnification after corrosion product was removed by Clarke solution for experiment condition of 70°C, 80 bar of CO ₂ and 400ppm of K1.	97
Figure 53: Surface image for experiment condition of 70°C, 80 bar of CO ₂ and 400ppm of K1 and after immersion in Clarke solution.	97
Figure 54: Surface of weight loss coupon at x1000 magnification and experiment condition of 70°C, 80 bar of CO ₂ and 800ppm of K1.....	98
Figure 55: Composition of corrosion product layer by EDS at x1000 magnification and experiment condition of 70°C, 80 bar of CO ₂ and 800ppm of K1.....	99
Figure 56: Surface of weight loss coupon at x1000 magnification after corrosion product was removed by Clarke solution for experiment condition of 70°C, 80 bar of CO ₂ and 800ppm of K1.	99
Figure 57: Composition of bare surface by EDS at x1000 magnification after corrosion product was removed by Clarke solution for experiment condition of 70°C, 80 bar of CO ₂ and 800ppm of K1.	100

Figure 58: Surface image for experiment condition of 70°C, 80 bar of CO ₂ and 800ppm of K1 and after immersion in Clarke solution.	100
Figure 59: Surface of weight loss coupon at x1000 magnification and experiment condition of 70°C, 80 bar of CO ₂ and 1500ppm of K1.....	101
Figure 60: Composition of corrosion product layer by EDS at x1000 magnification and experiment condition of 70°C, 80 bar of CO ₂ and 1500ppm of K1.....	102
Figure 61: Surface image for experiment condition of 70°C, 80 bar of CO ₂ and 1500ppm of K1 and after immersion in Clarke solution.	102
Figure 62: Corrosion rate with time by linear polarization resistance at 70°C, 80 bar of CO ₂ and various concentrations of corrosion inhibitor formulation K4.....	104
Figure 63: Solution resistance (R _s) and Polarization resistance (R _p) by electrochemical impedance spectroscopy at 70°C, 80 bar of CO ₂ and various concentrations of corrosion inhibitor formulation K4.....	105
Figure 64: Potentiodynamic sweeps at 70°C, 80 bar pressure of CO ₂ and various concentration of corrosion inhibitor K4.....	106
Figure 65: Surface of weight loss coupon at x1000 magnification and experiment condition of 70°C, 80 bar of CO ₂ and 50ppm of K4.....	107
Figure 66: Composition of corrosion product layer by EDS at x1000 magnification and experiment condition of 70°C, 80 of CO ₂ and 50ppm of K4.....	107
Figure 67: Surface of weight loss coupon at x1000 magnification after corrosion product was removed by Clarke solution for experiment condition of 70°C, 80 bar of CO ₂ and 50ppm of K4.	108

Figure 68: Composition of bare surface by EDS at x1000 magnification after corrosion product layer was removed by Clarke solution for experiment condition of 70°C, 80 bar of CO ₂ and 50ppm of K4.	109
Figure 69: Surface image for experiment condition of 70°C, 80 bar CO ₂ and 50ppm of K4 and after immersion in Clarke solution.....	109
Figure 70: Surface of weight loss coupon at x1000 magnification and experiment condition at 70°C, 80 of CO ₂ and 100ppm of K4.	111
Figure 71: Composition of corrosion product layer by EDS at x1000 magnification and experiment condition of 70°C, 80 bar of CO ₂ and 100ppm of K4.....	111
Figure 72: Surface of weight loss coupon at x1000 magnification after corrosion product was removed by Clarke solution and experiment condition of 70°C, 80 bar of CO ₂ and 100ppm of K4.	112
Figure 73: Composition of bare surface by EDS at x1000 magnification after corrosion product was removed by Clarke solution for experiment condition of 70°C, 80 bar of CO ₂ and 100ppm of K4.	113
Figure 74: Surface image for experiment condition of 70°C, 80 bar of CO ₂ and 100ppm of K4 and after immersion in Clarke solution.	114
Figure 75: Surface of weight loss coupon at x1000 magnification and experiment condition of 70°C, 80 bar of CO ₂ and 200ppm of K4.....	115
Figure 76: Composition of corrosion product layer by EDS at x1000 magnification and experiment condition of 70°C, 80 bar of CO ₂ and 200ppm of K4.....	115

Figure 77: Surface of weight loss coupon at x1000 magnification after film was removed by Clarke solution for experiment condition of 70°C, 80 bar of CO ₂ and 200ppm of K4.	116
Figure 78: Composition of bare surface by EDS at x1000 magnification after corrosion product was removed by Clarke solution for experiment condition of 70°C, 80 bar of CO ₂ and 200ppm of K4.	116
Figure 79: Surface image for experiment condition of 70°C, 80 bar of CO ₂ and 200ppm of K4 and after immersion in Clarke solution.	117
Figure 80: Surface of weight loss coupon at x1000 magnification and experiment condition of 70°C, 80 bar of CO ₂ and 400ppm of K4.....	118
Figure 81: Composition of corrosion product layer by EDS at x1000 magnification for experiment condition of 70°C, 80 bar of CO ₂ and 400ppm of K4.....	118
Figure 82: Surface of weight loss coupon at x1000 magnification after corrosion product was removed by Clarke solution and experiment condition at 70°C, 80 bar of CO ₂ and 400ppm of K4.	119
Figure 83: Composition of bare surface by EDS at x1000 magnification after corrosion product was removed by Clarke solution and experiment condition of 70°C, 80 bar of CO ₂ and 400ppm of K4.....	120
Figure 84: Surface image for experiment condition at 70°C, 80 bar of CO ₂ and 400ppm of K4 and after immersion in Clarke solution.....	121
Figure 85: Surface of weight loss coupon at x100 magnification for experiment condition of 70°C and 80 bar of CO ₂ in absence of corrosion inhibitor.	139

Figure 86: Corrosion product layer composition by EDS at x100 magnification for experiment condition of 70°C and 80 bar of CO ₂ in absence of corrosion inhibitor.....	140
Figure 87: Surface of weight loss coupon at x100 magnification after corrosion product was removed by Clarke solution for experiment condition of 70°C and 80 bar of CO ₂ in absence of corrosion inhibitor.....	140
Figure 88: Composition of bare surface by EDS at x100 magnification after corrosion product was removed by Clarke solution for experiment condition of 70°C and 80 bar of CO ₂ in absence of corrosion inhibitor.....	141
Figure 89: Surface of weight loss coupon at x100 magnification and experiment condition of 70°C, 80 bar of CO ₂ and 50ppm of K1.....	141
Figure 90: Composition of corrosion product layer by EDS at x100 magnification and experiment condition of 70°C, 80 bar of CO ₂ and 50ppm of K1.....	142
Figure 91: Surface of weight loss coupon at x100 magnification after corrosion product was removed by Clarke solution for experiment condition of 70°C, 80 bar of CO ₂ and 50ppm of K1.....	142
Figure 92: Composition of bare surface by EDS at x100 magnification after corrosion product was removed by Clarke solution and experiment condition of 70°C, 80 bar of CO ₂ and 50ppm of K1.....	143
Figure 93: Surface of weight loss coupon at x100 magnification and experiment condition of 70°C, 80 bar of CO ₂ and 100ppm of K1.....	143
Figure 94 : Composition of corrosion product layer by EDS at x100 magnification and experiment condition of 70°C, 80 bar of CO ₂ and 100ppm of K1.....	144

Figure 95: Surface of weight loss coupon at x100 magnification after corrosion product layer was removed by Clarke solution and experiment condition of 70°C, 80 bar of CO ₂ and 100ppm of K1.	144
Figure 96: Compositional of bare surface by EDS at x100 magnification after film was removed by Clarke solution. The experiment condition was 70°C, 80 bar of CO ₂ and 100ppm of K1.	145
Figure 97: Surface of weight loss coupon at x100 magnification and experiment condition of 70°C, 80 bar of CO ₂ and 400ppm of K1.....	145
Figure 98: Composition of corrosion product layer by EDS at x100 magnification and experiment condition at 70°C, 80 bar of CO ₂ and 400ppm of K1.....	146
Figure 99: Surface of weight loss coupon at x100 magnification after film was removed by Clarke solution and experiment condition of 70°C, 80 bar of CO ₂ and 400ppm of K1.	146
Figure 100: Composition of bare surface by EDS at x100 magnification after corrosion product was removed by Clarke solution for experiment condition of 70°C, 80 bar of CO ₂ and 400ppm of K1.	147
Figure 101: Surface of weight loss coupon at x100 magnification and experiment condition of 70°C, 80 bar of CO ₂ and 800ppm of K1.....	147
Figure 102: Composition of corrosion product layer by EDS at x100 magnification and experiment condition of 70°C, 80 bar of CO ₂ and 800ppm of K1.....	148
Figure 103: Surface of weight loss coupon at x100 magnification after corrosion product was removed by Clarke solution for experiment condition of 70°C, 80 bar of CO ₂ and 800ppm of K1.	148

Figure 104: Composition of bare surface by EDS at x100 magnification after corrosion product was removed by Clarke solution for experiment condition of 70°C, 80 bar of CO ₂ and 800ppm of K1.	149
Figure 105: Surface of weight loss coupon at x100 magnification and experiment condition of 70°C, 80 bar of CO ₂ and 1500ppm of K1.....	149
Figure 106: Composition of corrosion product layer by EDS at x100 magnification and experiment condition of 70°C, 80 bar of CO ₂ and 1500ppm of K1.....	150
Figure 107: Surface of weight loss coupon at x100 magnification and experiment condition of 70°C, 80 bar of CO ₂ and 50ppm of K4.....	150
Figure 108: Composition of corrosion product layer by EDS at x100 magnification and experiment condition of 70°C, 80 bar of CO ₂ and 50ppm of K4.....	151
Figure 109: Surface of weight loss coupon at x100 magnification after corrosion product was removed by Clarke solution for experiment condition of 70°C, 80 bar of CO ₂ and 50ppm of K4.	151
Figure 110: Composition of bare surface by EDS at x100 magnification after corrosion product layer was removed by Clarke solution for experiment condition of 70°C, 80 bar of CO ₂ and 50ppm of K4.	152
Figure 111: Surface of weight loss coupon at x100 magnification and experiment condition at 70°C, 80 of CO ₂ and 100ppm of K4.	152
Figure 112: Composition of corrosion product layer by EDS at x100 magnification and experiment condition of 70°C, 80 bar of CO ₂ and 100ppm of K4.....	153

Figure 113: Surface of weight loss coupon at x100 magnification after corrosion product was removed by Clarke solution and experiment condition of 70°C, 80 bar of CO ₂ and 100ppm of K4.....	153
Figure 114: Composition of bare surface by EDS at x100 magnification after corrosion product was removed by Clarke solution for experiment condition of 70°C, 80 bar of CO ₂ and 100ppm of K4.	154
Figure 115: Surface of weight loss coupon at x100 magnification and experiment condition at 70°C, 80 bar of CO ₂ and 200ppm of K4.	154
Figure 116: Composition of corrosion product layer by EDS at x100 magnification and experiment condition of 70°C, 80 bar of CO ₂ and 200ppm of K4.....	155
Figure 117: Surface of weight loss coupon at x100 magnification after film was removed by Clarke solution for experiment condition of 70°C, 80 bar of CO ₂ and 200ppm of K4.	155
Figure 118: Composition of bare surface by EDS at x100 magnification after corrosion product was removed by Clarke solution for experiment condition of 70°C, 80 bar of CO ₂ and 200ppm of K4.	156
Figure 119: Surface of weight loss coupon at x100 magnification for experiment condition at 70°C, 80 bar of CO ₂ and 400ppm of K4.	156
Figure 120: Composition of corrosion product layer by EDS at x100 magnification and experiment condition of 70°C, 80 bar of CO ₂ and 400ppm of K4.....	157
Figure 121: Surface of weight loss coupon at x100 magnification after corrosion product was removed by Clarke solution and experiment condition of 70°C, 80 bar of CO ₂ and 400ppm of K4.	157

Figure 122: Composition of bare surface by EDS at x100 magnification after corrosion product was removed by Clarke solution and experiment condition at 70°C, 80 bar of CO₂ and 400ppm of K4..... 158

CHAPTER 1: INTRODUCTION

Background

Geologic sequestration is one of the main initiatives to lessen global warming caused by emission of carbon dioxide to the atmosphere. Carbon dioxide is captured from natural gas, flue gas or syngas streams then transported to injection wells *via* pipeline transmission systems. Captured carbon dioxide is usually transported over a long distance in large diameter, high pressure pipelines (1) (2) (3). The carbon dioxide stream has to be dried and free from impurities such as hydrogen sulfide, methane and nitrogen (4). Determination of maximum allowable water concentration in the CO₂ pipeline is important to prevent free water formation. When free water is present, CO₂ will partially dissolve therein and form carbonic acid (5). This will cause corrosion problems with the carbon steel commonly used to make pipelines (6). Consequently, it is desirable to establish a minimum quality specification for CO₂ pipelines relating to the presence of water (1), (2). The maximum allowable water for CO₂ pipelines operated by Kinder Morgan is 600ppm and for Mitra Dinamis is 500ppm (7) (8) (9). Some CO₂ pipelines are transporting anthropogenic CO₂ which was captured and treated from industrial facilities such as the Val Verde natural gas plant, Great Plains Synfuels coal gasification plant (for subsequent injection at Weyburn) and Bairoil CO₂ capture plant (3). Currently, there are some 2400km of large capacity CO₂ pipelines in operations, mostly in the United States of America (10). Some CO₂ pipelines transport CO₂ captured from well streams such as at Cortez, Sheep Mountain and Bravo (3). Compressed CO₂ in liquid and supercritical phase has been identified as an efficient medium for pipeline transportation of CO₂ over the longer pipeline distances. This is due to the lower friction drop along the pipeline per

unit mass of CO₂ compared to transportation of CO₂ in low pressure condition when CO₂ is in the gas phase (11) (12). Along the pipeline, pressure is reduced with decreasing temperature, due to heat loss, consistent with Gay-Lussac's gas law (13) (12).

The design of the CO₂ pipelines should meet the requirements of appropriate regulations and guidelines in terms of materials, wall thickness, diameter, monitoring facilities and pressure (6) (4) (14). The guidelines are important for safe, reliable and cost efficient transportation of CO₂ in pipelines (15). Carbon steel pipelines can be subject to very severe internal corrosion due to insufficient removal of water from the sources gas. From the operational point of view, a fully "dry" CO₂ pipeline stream is difficult to achieve during the process set-up and is not a feasible option, especially for offshore pipelines. (12)

Water chemistry in high pressure CO₂ environments

The presence of water in pipelines causes a serious problem for internal corrosion. Carbon dioxide gas forms carbonic acid (H₂CO₃) when dissolved into and hydrated by water. Bicarbonate (HCO₃⁻), carbonate (CO₃²⁻) and hydrogen/hydronium ions (H⁺/H₃O⁺) are produced from the dissociation processes, involving carbonic acid in such systems; this is further described in Chapter 2 (16) (17). Pipelines made from mild steel, an iron-based (Fe) material, are degraded by reducible species such as H₂CO₃, HCO₃⁻ and H⁺ in aqueous solution by oxidation processes.

In the research described herein, conditions were simulated in the laboratory to determine how particular parameters affected this corrosion mechanism. Conditions within the pipeline have been also modeled using well known software packages, used during design and material selection stages of project development, such as: ECE™,

Predict™, Multicorr™, Hydrocorr™ and Cassandra™ (18) (19). The development of corrosion prediction models began in the 1970s with de Waard's pioneering work (20) (21). The models that were subsequently developed used different approaches, with latter models being derived using a mechanistic basis (22) (23). Most models can only accurately predict corrosion rates at pressures of up to 10 bar of CO₂, overestimating corrosion rates if applied beyond this pressure. Most mechanistic models apply Henry's Law to determine the solubility of CO₂ in water. In high pressure CO₂, the gas/liquid system is not ideal and does not follow Henry's Law for solubility of CO₂ in water (24). This leads to serious deficiency in corrosion prediction modeling, which typically uses Henry's law.

Consequently, the study reported herein attempts to develop a water chemistry model relating to CO₂ corrosion that takes into consideration the non-ideal behavior in order to prevent overestimation of the concentration of dissolved CO₂ in water. A certain moiety of this aqueous CO₂ will undergo hydration to form H₂CO₃, a corrosive species which will also dissociate to form HCO₃⁻, CO₃²⁻ and H⁺. In high pressure CO₂ systems, both H₂CO₃ and H⁺ will be dominant, these are reducible species which oxidize iron to form ferrous ion (Fe²⁺). Experiments were then designed to validate the accuracy of the model.

Corrosion inhibition in high pressure CO₂ environments

Mild steel has long been used in the oil and gas industry due to its hardness, strength and weldability properties, as well as its economic value compared to other alloys used for pipeline fabrication (1) (12). The downside of carbon steel is that it does not offer sufficient protection against corrosion, due to reducible species such as H₂CO₃

and H^+ which are able to aggressively attack the internal surface of the mild steel pipelines. In order to confer protection, injection of corrosion inhibitors can be successfully employed. Corrosion inhibitors used in the oil and gas industry fall into four general categories based on mechanism and composition. These are categorized by: 1) barrier layer formation; 2) neutralizing potential; 3) scavenging capacity; and 4) ability to otherwise effect environmental modification (25). Typically, an internal pipeline surface can be thought of as being covered by a thin film of corrosion inhibitor which forms a barrier between the pipeline surface and the reducible species. This barrier slows down electrochemical reactions what leads to lower corrosion rates (26) (27).

Many commercial corrosion inhibitors are on the market but minimal information is usually released about them, due to their formulations being proprietary. Two type of generic corrosion inhibitor, based on imidazoline and imidazoline plus thiosulfate, have been evaluated in the present study, which are proven to protect pipeline surfaces in low pressure CO_2 environments. Within ICMT, these are known as K1 and K4, respectively (28). These have a film forming corrosion inhibition mechanism with a hydrophobic film attaching itself to the steel surface (29), (30). A final goal of the present research was to determine their efficacy in high pressure CO_2 environments.

CHAPTER 2: LITERATURE REVIEW

Water chemistry in high pressure CO₂ environments

Several prediction models for CO₂ corrosion have been developed over the last four decades. Most of these models have proven successful for prediction of corrosion rates for CO₂ pressures of up to 10 bars. However, inaccurate corrosion rates are predicted by these models if applied for pressures exceeding 10 bars of CO₂. The model simulation data highly overestimate the corrosion rates if compared to data produced from experiment (31), (32). The high pressure CO₂ experimental results from Seiersten, *et al.*, also show that the current model predicts corrosion rates to be ten times higher than the experimental result (31) (33) (34). Initial corrosion prediction models were derived from experimental data for low pressure systems (20) (21). Initially, nomograms combined with empirical correction factors were used for corrosion prediction by engineers in oil and gas companies, especially for material selection and design stages. Mechanistic corrosion prediction models were subsequently developed and described by Gray, *et al.*, and Nesic, *et al.*, using mechanisms of CO₂ corrosion described in the literature (22) (23) (35).

The equilibrium constants for the Multicorp™ corrosion prediction model, which is one of the most advanced mechanistic models available, developed within the Institute for Corrosion and Multiphase Technology, can be found in the open literature (24). The equilibrium constants that are valid for these systems were taken from Spycher, *et al.*, Palmer & Van Eldik, and Duan, *et al.*, (36) (37) (38) (39). At equilibrium, the reversible chemical reactions have no further change when they reach their lowest Gibbs energy level. This corresponds to a $dG = 0$, when a system reaches equilibrium (13).

$$\partial G = -S\partial T + V\partial P \quad [1]$$

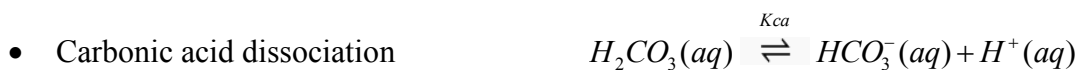
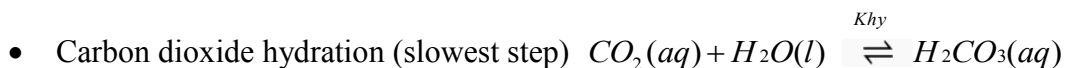
$$\partial G = \partial G^\circ - RT \ln K \quad [2]$$

At equilibrium: $0 = \partial G^\circ - RT \ln K \quad [3]$

$$\partial G^\circ = -RT \ln K \quad [4]$$

In a study relating to aqueous high pressure CO₂, Gibbs free energy and equilibrium constants were shown to be affected by temperature and pressure (37), (38).

The actual chemical reactions involved in a H₂O/CO₂ system are identical whatever the partial pressure of CO₂ (23) (17) (40). These reactions are listed below:



A key strength of the mechanistic models is their flexibility in extending the validity domain (24). New knowledge or parameters can be added without major modification of the existing model structure. Generally, constants of the reactions can be changed and matched to the required operating parameters. In the current work equilibrium constants for CO₂ pressures above 10 bars were selected from the open literature and implemented. Several papers relating to CO₂-H₂O water chemistry models and experiments have been published by Meyssami, *et. al.*, (41), Duan & Li (39),

Spycher, *et al.* (36) in high partial pressure CO₂ environments. Most of the constants used here are obtained from work reported by Spycher (2003) (36), Duan & Li (2008) (39) and Palmer & Van Eldik (37). The constants reported by Spycher, *et al.*, are valid for CO₂-H₂O systems in the temperature range of 12-100°C and pressures up to 600 bar (36); while the constants from Duan & Li are valid at 1-100°C and pressures up to 2000 bar (39).

The newly developed water chemistry model will be used as a basis for the corrosion prediction model for high pressure CO₂ and provide the relative concentrations of CO₂ (aqueous), H₂CO₃, H⁺, OH⁻, HCO₃⁻ and CO₃²⁻ in the bulk solution of the CO₂-H₂O system. Once concentrations of these species are known, mass transport will be modeled to predict species concentration in the mass transfer boundary layer region. Predictions can then be made for the corrosion rate and protective film formation. H₂CO₃ and H⁺ will serve as the main oxidizing agents at low pH while HCO₃⁻ will dominate at high pH.

In the current work, experiments were set up to validate the accuracy of the water chemistry model in the temperature range of 25°C to 100°C and CO₂ pressures of up to 600 bars. At low pressures of CO₂, below 10 bars, and temperature below 100°C, CO₂ acts like an ideal gas. Henry's law can be used to explain the solubility of CO₂ in this condition (13). As CO₂ transitions to the liquid then supercritical state, this will no longer apply. The deviation from ideal behavior is large at high pressure and low temperature while at lower pressures and high temperatures, the deviation from ideal behavior is typically small, and the ideal gas law can be used to predict behavior with little error. Henry's law can be modified by introducing intermolecular factors that are

determined from experiment. In the high pressure conditions, the intermolecular distances can become quite short, and attractive forces between molecules become significant. The observed pressure exerted by the gas under these conditions will be less than that for an ideal gas. (13) (42) (36). The correction for molecular attraction (constant a) and correction for volume of molecules (constant b) follow the Redlich-Kwong equation of state (36) (43).

Corrosion inhibition in high pressure CO₂ environments

Use of corrosion inhibitors is one of the key corrosion control measures to mitigate internal corrosion of pipeline transmission systems. They are routinely applied in oil and gas operations as an economical and effective method to mitigate carbon dioxide corrosion at partial pressures of carbon dioxide of less than 20 bar (44) (45). The application of corrosion inhibitor to protect carbon steel pipeline is significant to reduce cost of the construction and new gas field development (46) (45).

Typically, corrosion inhibitors are surface active compounds that possess a polar hydrophilic head and a non-polar hydrophobic tail within its molecular structure. This combined hydrophilicity/hydrophobicity facilitates inhibitor adsorption onto metal surfaces, forming a barrier that retards the electrochemical corrosion process (47) (48).

These surface active agents are required to reduce corrosion rates to a manageable rate of corrosion rate (<0.1 mm/yr) to ensure facility integrity (49). These corrosion inhibitors can interfere with the anodic or cathodic reaction sites as well as form a barrier on the metal surface against corrosive agents, or work by a combination of these actions. For the cathodic reaction, corrosion inhibitor will retard the reduction of hydrogen ions to form hydrogen gas. Zinc hydroxide and zinc phosphate are examples of corrosion

inhibitors which are able to retard cathodic reactions on the metal surface (50) (51). A cathodic corrosion inhibitor can form insoluble compounds that deposit on the cathodic sites and form a barrier film. Anodic type corrosion inhibitor is able to depress the anodic reaction on the metal surface (52), (51). The oxidation of iron can be hindered by anodic type corrosion inhibitor, such as chromate (CrO_4^{2-}). Chromate type corrosion inhibitors are widely used in aviation applications when the material is made from aluminum (53).

The nature of the adsorption process is of key importance for inhibition when the surfactant functional groups adsorb onto the metal and displace water from the surface. There are three types of adsorption mechanism between corrosion inhibitor and steel surfaces (54):

- Physical adsorption (physisorption)
- Chemical adsorption (chemisorption)
- Combination of physical adsorption and chemisorption.

Physical adsorption, or physisorption, is an adsorption of corrosion inhibitor on the metal surface by intermolecular forces (van der Waals forces) and does not involve a significant change in the electronic orbital arrangements of the species involved (55). Chemisorption (or chemical adsorption) is an adsorption of corrosion inhibitor to the metal surface and can involve transferring and sharing of electrons with the metal surface (55) (50). Pure chemisorption would imply bond formation. Some corrosion inhibitors have shown a hybrid adsorption on metal surfaces (50).

The adsorption of the corrosion inhibitor (CI) is determined by the concentration of the CI, head group functionality and environment (44) (56). The chemisorption

strength depends on the electron density on the donor atom (S, N or O) of the functional group and its ability to form a chemical bond with the surface (30) (54) (57) (56). Nitrogen and sulfur have the potential to act as a Lewis base electron-pair donor if the character of the steel surface is such that it can act as an electron-pair acceptor (58), (59). Compounds with π -electrons and functional groups containing heteroatoms, in particular, have the potential to donate lone pair electrons and are important as corrosion inhibitors to protect metals (58), (52), (59). Heteroatom (N, S) electrons have been described as interacting with vacant orbitals of iron during this bond formation process (56) (60).

The adsorption of inhibitors on metal surfaces can be explained by adsorption isotherms, such as the Langmuir, Freundlich and BET types (61) (62). In order to obtain an isotherm, the surface coverage θ , as a function of concentration of CI is obtained by experiment. In the high partial pressure CO_2 condition, when the quantities of reducible species are elevated compared to the low partial pressure of CO_2 condition, the surface coverage of corrosion inhibition on the metal surface is really important to prevent the reducible species from reacting with the metal surface. The Langmuir adsorption model is the most common model used to quantify the amount of adsorbed corrosion inhibitor on a metal surface at a given temperature (63); it is valid specifically for a single layer of corrosion inhibitor on the metal surface. Among the assumptions for the Langmuir model is that the metal surface is a perfectly flat plane, corrosion inhibitor adsorbs into an immobile state, all sites are equivalent, and there are no interactions among adjacent corrosion inhibitor molecules. For a rough metal surface, the Freundlich model is considered a good model (64) (65). The Temkin model takes into account interaction

between corrosion inhibitor molecules (63) (66) (67). The BET model is used for multilayer adsorption, that is, surface coverage by one, two, and three corrosion inhibitor layers attached on the metal surface (63) (68) (69).

Film persistency is also important for corrosion inhibitor application and selection (70). The persistency of corrosion inhibitor is related to the adsorption enthalpy (44) (71). The effect of flow velocity on film persistency was studied by other researchers when the flow velocity is up to 20m/s. The flow velocity is proportional to the shear stress per unit area and follows the Newton law of viscosity (72). A study by Gulbrandsen showed that shear stresses of up to 1400 Pa of flowing solution didn't affect the adsorption of corrosion inhibitor on the metal surface. The thickness of corrosion inhibitor is thinner than the viscous sub-layer even in a turbulent flow condition when the flow velocity is 20m/s (73). In the mass transfer controlled systems, the flow velocity can increase the inhibited corrosion rate and when trace dissolved oxygen higher than 40ppm is in the solution (73) (74). The persistence of corrosion inhibitor film on the metal surface is affected by increasing temperature (75). The kinetic energy of the molecules increases with increasing temperature and facilitates their detachment from the metal surface. When an adsorbed molecule receives energy equal to or greater than the energy of adsorption, it will leave the surface. For physisorption, this energy is in the range of 8 to 25 kJ/mole whereas a much larger energy, comparable to chemical bonding energy, leads to chemisorption (76) (77) (56).

Imidazoline-type molecules represent one class of nitrogen based organic corrosion inhibitors. They have been successfully applied in pipelines at low pressures of CO₂ (78) (79) (80). The nitrogen atoms in the imidazoline act as Lewis base electron

donors and the steel surface acts as an electron acceptor (81). Adsorption of imidazoline-type corrosion inhibitor is governed by the length of its alkyl tail, the nature of its hydrophilic head and solution properties (79). This last point will likely be of key importance for the efficacy of N-containing inhibitors in high pressure CO₂ systems as supercritical CO₂ can act as an excellent solvent for amines. Imidazoline-type corrosion inhibitor can retard the anodic and cathodic reactions (82).

In 1983, a combination of sulfur with an imidazoline-type corrosion inhibitor was patented by Oppenlaender, *et al.*, for H₂S and CO₂ oilfield applications. This patent stated that performance of corrosion inhibitor is enhanced after addition of the sulfur (83). A similar effect for addition of a sulfur-containing compound was also found by Zhang, *et al.*, where the inhibition performance of an imidazoline derivative plus thiourea was shown to be superior to that for the imidazoline-type inhibitor alone (82). Sulfide derived from thiosulfates will act as a Lewis base, electron pair donor, interacting with the steel surface behaving akin to a Lewis acid, electron pair acceptor (82). In 1996, Phillip, *et al.*, observed that combination of sodium thiosulfate with cationic corrosion inhibitor gave superior performance compared with cationic corrosion inhibitor (*i.e.*, quaternary alkyl ammonium or imidazolium) alone. This report has mentioned that the addition of a small concentration of thiosulfate can form a passive film which is resistant to corrosion (84). Phillip, *et al.*, showed that the inhibiting mechanism of thiosulfate on the metal surface is not by absorption (84). The data from X-ray photoelectron spectroscopy (XPS) and time of flight secondary ion mass spectrometry (TOFSIMS) indicated no thiosulfate is adsorbed on the metal surface. These findings were supported by Yao's dissertation on the adsorption of corrosion inhibitor to the metal surface using

atomic force microscopy (85). Yao reported that the addition of small quantities of sodium thiosulfate did not have an effect of increasing adsorption of corrosion inhibitor molecules to a mica surface. This report also indicated that the additive sodium thiosulfate does not increase the film thickness and change the adsorption structure of inhibitor molecules (29), (86), (85). In high shear stress pipeline conditions, corrosion inhibitor containing sulfur has been reported to have been successfully used by pipeline operators (78). In the surface cleaning industry, corrosion inhibitors containing sulfur-containing species are also used in sulfuric acid media to protect the metal from undesired corrosion (54) (87).

Jovancicevic, *et. al.*, described a process whereby reduction of thiosulfate ion to sulfide ion results in formation of a protective film as iron is oxidized. The protective layer formed by this reaction is iron disulfide/pyrite (FeS_2) (78) (88). Kappes and Frenkel have stated that disproportionation of thiosulfate ion results in formation of elemental sulfur (S^0) and sulfide (S^{2-}), which reacts with iron on the corroded surface to form a thin layer of mackinawite-type iron sulfide (FeS). The chemical reaction is shown below (89) (90):

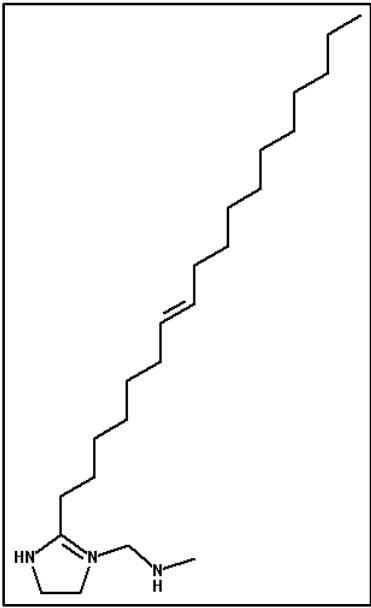
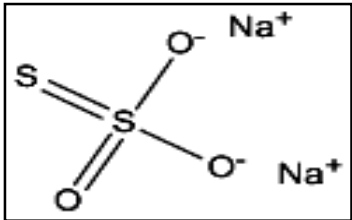


The thickness of the thin mackinawite/iron sulfide layer is less than 1 μm and it is very “tight”. In agreement with findings reported by Sun, *et al.*, diffusion is slowed through the generated thin layer (91).

In summary, corrosion inhibitor containing sulfur species can have superior protection on the steel surface compared to imidazoline-type corrosion inhibitor alone. Imidazoline-type is one class of nitrogen-typed organic corrosion inhibitor while

sulfur/sulfide from thiosulfate disproportionation reacts with iron to form a thin layer of iron sulfide, which is very protective and cannot be seen by SEM (91). This iron sulfide interaction is stronger than interactions between imidazoline nitrogen and the metal surface (58). The properties of the inhibitor compounds studied in this work are summarized in Table 1.

Table 1: The properties of corrosion inhibitors K1 and K4.

Imidazoline-type (K1)	Imidazoline plus Thiosulfate (K4)
 <p data-bbox="282 1094 846 1199">A chemical structure of DETA imidazoline (29) (85)</p>	 <p data-bbox="894 709 1409 741">A chemical structure of thiosulfate. (92)</p>
Molecular length of imidazoline-type inhibitor: 2.2 nm (29)	Diameter of thiosulfate: 0.2 nm (29)
Critical Micelle Concentration (CMC) in 1 wt. % NaCl solution: 36ppm K1 (28).	Critical Micelle Concentration (CMC) in 1 wt. % NaCl solution: 215ppm K4 (28).

CHAPTER 3: RESEARCH OBJECTIVES AND TEST MATRICES

Water chemistry in high pressure CO₂ environments

The specific purpose of this research project can be described as follows:

- I. Develop a water chemistry model for high partial pressure of CO₂ which can accurately quantify the concentrations of H⁺, H₂CO₃, HCO₃⁻, CO₃²⁻ and OH⁻ in solution. The scope of the model is up to 600 bars of CO₂ and temperature up to 100°C. The model will be used as input in the corrosion prediction model Supercorp™.
- II. Validate the accuracy of the water chemistry model in autoclave experiments to:
 - Determine the solubility of CO₂ in water, xCO₂. Water containing dissolved CO₂ is to be sampled in an equilibrium state relating to desired temperature and pressure. Sampled CO₂ in water will be released at low pressure condition governed by ideal gas laws. Dissolved CO₂ in solution will escape to the gas phase due to the low solubility of CO₂ in water at low pressure of CO₂ until equilibrium is reached. The solubility of CO₂ in water can be determined by increasing pressure in the gas phase and amount of dissolved CO₂ in the solution.
 - Determine the solubility of water in CO₂, yH₂O. CO₂ gas containing water vapor is sampled from a 20 liter autoclave and measured by gravimetric and sensor-based techniques.
 - Determine the concentration of species in the solution. The measured concentrations of hydrogen ions are determined by measuring the pH.

Text matrix

The text matrix for the experiments is shown in Table 2.

Table 2: Test parameters for pH measurement and solubility of CO₂ and water.

Temperature (°C)	25, 40 and 60
Partial Pressure of CO ₂ (bar)	10, 20, 30, 40, 50, 60, 70 and 80
Solution	Deionized water
Time Exposure (hours)	24
Flow Condition	Stagnant
Measurement technique	pH

Corrosion inhibition in high pressure CO₂ environments

Two types of generic corrosion inhibitor with known formulations are used in this study. The specific purposes of this part of the research project are to:

- I. Experimentally study the effect of corrosion inhibitor in high pressure CO₂ corrosion systems. Comparisons are conducted for the gas, liquid and supercritical phases of CO₂ in order to determine the:
 - effect of the active agent in the corrosion inhibitor
 - effect of concentration of corrosion inhibitor
 - effect of sulfur in the active agents

The test matrices for this study, as well as compositional information for the studied inhibitors and steel type, are shown in Table 3, Table 4, Figure 1 and Figure 2.

Test matrix

Table 3: Test matrix for corrosion inhibition study.

Material	Carbon Steel X65
Temperature (°C)	70
Pressure (bar)	80
pH	Natural pH
Corrosion inhibitor	K1, K4
Inhibitor concentration (ppm)	50, 100, 200, 500, 1000, 1500
Time exposure (hours)	24
Flow condition	Stagnant
Measurement techniques	Weight loss, OCP, LPR, EIS, Potentiodynamic
CI treatment method	Continuous injection

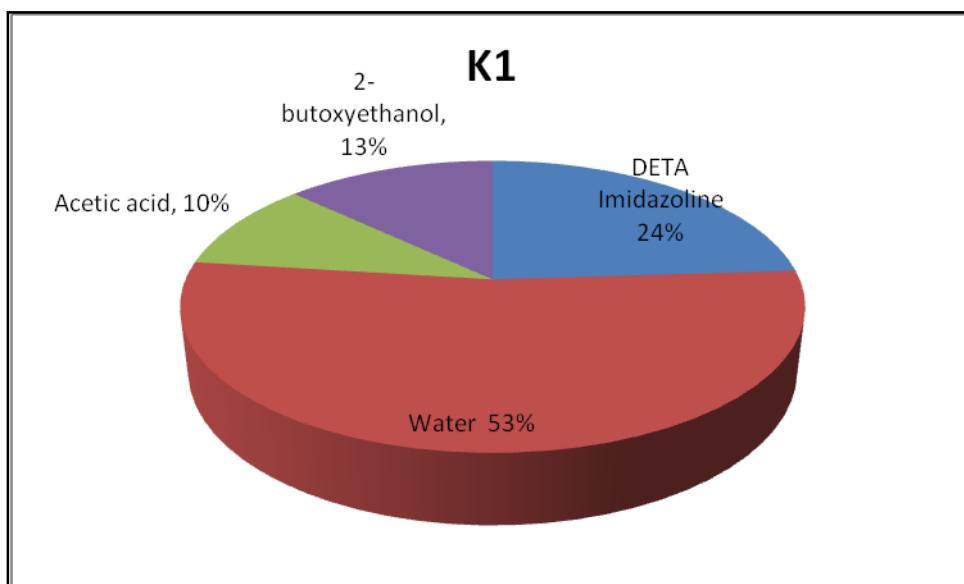


Figure 1: Formulation of corrosion inhibitor K1.

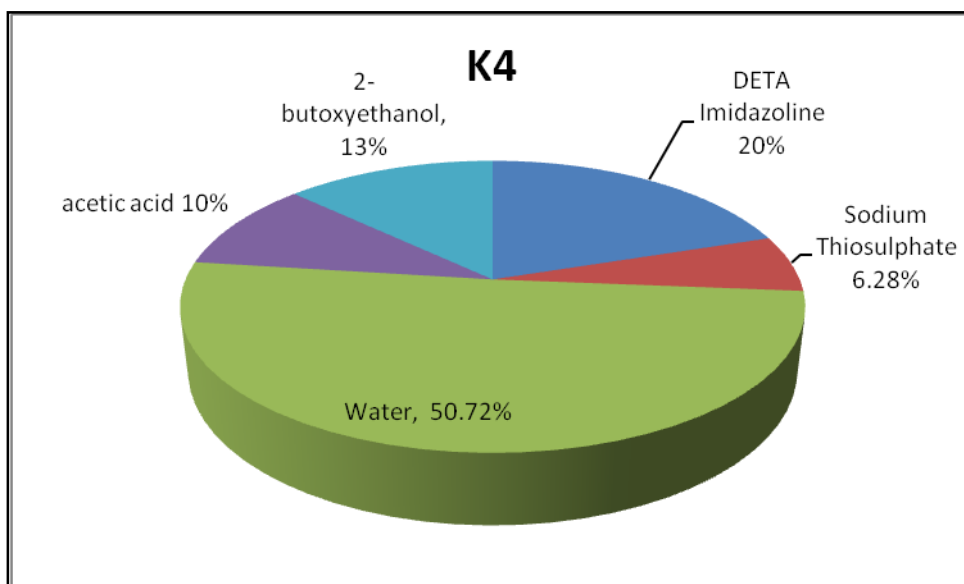


Figure 2: Formulation of corrosion inhibitor K4.

Table 4: Chemical composition of the API 5L X65 carbon steel used in this work

(mass %, balance Fe).

C	Mn	Si	Nb	V	P	S	Cr	Cu	Ni	Mo	Al
0.15	1.34	0.24	0.03	0.05 5	0.011	0.00 4	0.01 1	0.01	0.02	0.103	0.032

CHAPTER 4: THE THEORITICAL BACKGROUND AND MODELING

In high pressure environments, CO₂ can exist in gaseous, liquid and supercritical fluid phases. The phase of CO₂ will depend on the temperature and pressure of the systems. The critical temperature for carbon dioxide is 31.1°C, and the critical pressure is 73 bar. Supercritical CO₂ occurs when temperature and pressure is above its critical point (11) (13). The phase diagram of carbon dioxide is shown in Figure 3. In high partial pressure of CO₂, greater than 10 bars, its behavior deviates from the ideal gas law; this has implications for its dissolution and subsequent hydration (16).

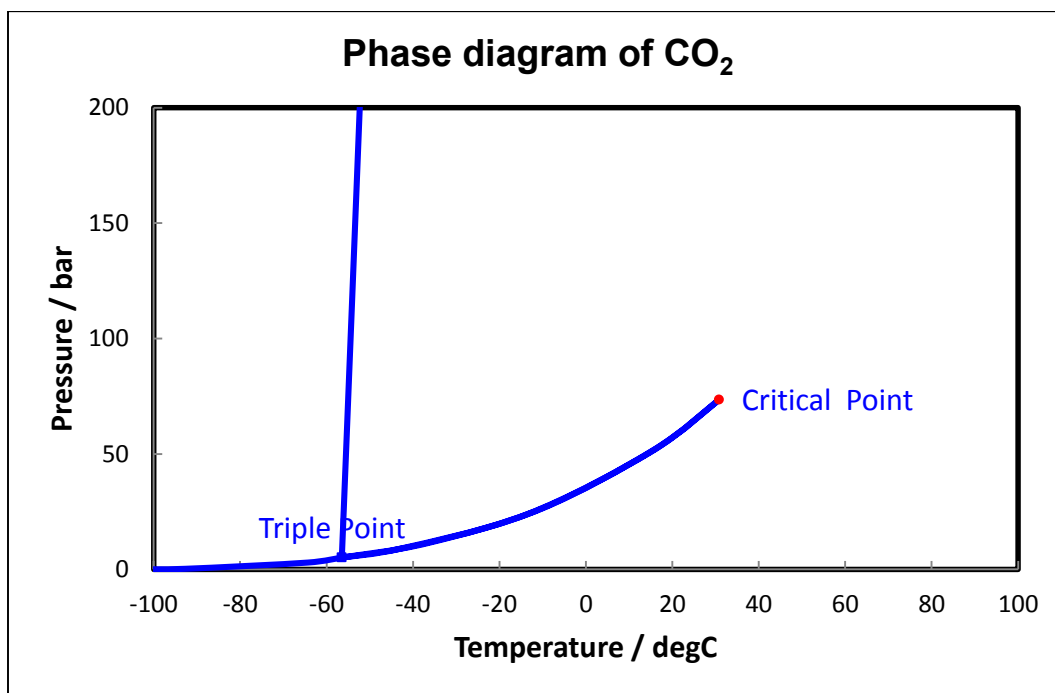


Figure 3: Phase diagram of carbon dioxide.

Dissolution of carbon dioxide

The dissolution of carbon dioxide at CO₂ partial pressure (pCO₂) of above 10 bars is different from that for partial pressure of 10 bars and below. In low pCO₂ systems, the solubility constant is calculated and derived from Henry's constant as the concentration of dissolved CO₂ as a solute is relatively small; hence Henry's law is applicable. In high pCO₂ systems, the non-ideal gas no longer follows Henry's law as the concentration of dissolved CO₂ is significant. Interactions between molecules become more significant at high pressure of CO₂. The equations of state which were taken into consideration for the non-ideal gas are those devised by Virial, Van der Waal, Redlich and Kwong (1949), and Peng and Robinson (93). The Redlich and Kwong (1949) equation is generally considered to be accurate enough for practical applications. Good results were shown by Spycher, *et al.*, using a modified Redlich-Kwong equation, with the intermolecular attraction parameter assumed to vary linearly with temperature (94) (95) . The Redlich-Kwong parameters for the attraction and repulsion were also taken from Spycher, *et al.*, for pure CO₂ (a_{CO_2} and b_{CO_2}), the repulsion parameter for pure water (b_{H_2O}), and the H₂O-CO₂ binary interaction parameter ($a_{H_2O-CO_2}$) (36).

Key reactions and equations can be written as follows:



$$K_{sol} = \frac{C_{CO_2(aq)}}{P_{CO_2(g)}} \quad [7]$$

C_{CO_2} represents the concentration of carbon dioxide dissolved in water and P_{CO_2} represents the partial pressure of carbon dioxide. The unit for the solubility constant is Molar/Bar.

In the equations below, y_{H_2O} and x_{CO_2} represent the mole fraction of water in carbon dioxide and the mole fraction of carbon dioxide in water, respectively.

$$y_{H_2O} = \frac{K_{H_2O}^o (1 - x_{CO_2})}{\phi_{H_2O} P_{Tot}} \exp \left(\frac{(P - P^o) \bar{V}_{H_2O}}{RT} \right) \quad [8]$$

$$x_{CO_2} = \frac{\phi_{CO_2} (1 - y_{H_2O}) P_{Tot}}{55.508 K_{CO_2(g)}^o} \exp \left(- \frac{(P - P^o) \bar{V}_{CO_2}}{RT} \right) \quad [9]$$

The below equations are the fugacity coefficients of CO_2 (ϕ_{CO_2}) and H_2O (ϕ_{H_2O}).

$$\begin{aligned} \ln(\phi_{H_2O}) = & \ln\left(\frac{V}{V - b_{CO_2}}\right) + \left(\frac{b_{H_2O}}{V - b_{CO_2}}\right) - \left(\frac{2 \sum_{i=1}^n y_{CO_2} a_{CO_2 - H_2O}}{RT^{1.5} b_{CO_2}}\right) x \\ & \ln\left(\frac{V + b_{CO_2}}{V}\right) + \\ & \left(\frac{a_{CO_2} b_{H_2O}}{RT^{1.5} b_{CO_2}^2}\right) \left[\ln\left(\frac{V + b_{CO_2}}{V}\right) - \left(\frac{b_{CO_2}}{V + b_{CO_2}}\right) \right] - \ln\left(\frac{PV}{RT}\right) \end{aligned} \quad [10]$$

$$\ln(\phi_{CO_2}) = \ln\left(\frac{V}{V - b_{CO_2}}\right) + \left(\frac{b_{CO_2}}{V - b_{CO_2}}\right) - \left(\frac{2\sum_{i=1}^n y_{H_2O} a_{CO_2 - H_2O}}{RT^{1.5} b_{CO_2}}\right) \times$$

$$\ln\left(\frac{V + b_{CO_2}}{V}\right) +$$

$$\left(\frac{a_{CO_2} b_{CO_2}}{RT^{1.5} b_{CO_2}^2}\right) \left[\ln\left(\frac{V + b_{CO_2}}{V}\right) - \left(\frac{b_{CO_2}}{V + b_{CO_2}}\right) \right] - \ln\left(\frac{PV}{RT}\right)$$
[11]

The volumes of compressed carbon dioxide gas V_{CO_2} and water V_{H_2O} can be obtained by solving the Redlich-Kwong equation of state. The cubic equation below is then solved using a Solver application in Microsoft Excel™.

$$V^3 - V^2\left(\frac{RT}{P}\right) - V\left(\frac{RTb_{CO_2}}{P} - \frac{a_{CO_2}}{PT^{0.5}} + b_{CO_2}^2\right) - \left(\frac{a_{CO_2}b_{CO_2}}{PT^{0.5}}\right) = 0$$
[12]

where, $R=83.1447$ bar.cm³/mol.K, V is in cm³/mol, P is in bar, and T is in K.

Once the cubic expression is solved and the values of compressed gas volume calculated, the carbon dioxide solubility constant can be obtained by evaluating each parameter in the above equations.

Carbon dioxide hydration

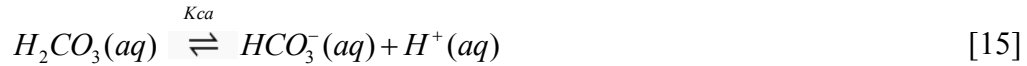
The equilibrium constant K_{hy} for carbon dioxide hydration is obtained from Palmer and Van Eldik (37). K_{hy} is a weak function of temperature and does not significantly change with temperature for the range of 20 – 100°C (17). Since it is not pressure dependent, the equilibrium constant of carbon dioxide hydration of 2.58×10^{-3} , which is used in the low pCO₂ environment model, is applicable for the high pressure CO₂ model (17) (96).



$$K_{hy} = C_{H_2CO_3} / C_{CO_2} \quad [14]$$

Carbonic acid dissociation

The constant K_{ca} is taken from Duan and Li. The equation is a function of temperature and pressure. K_{ca} has been calculated from 0°C to 100°C and pressure ranges from 1 to 3000 bar (39).



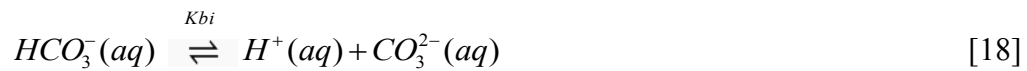
$$K_{ca} = C_{H^+} C_{HCO_3^-} / C_{H_2CO_3} \quad [16]$$

$$\begin{aligned} \ln K_{ca} = & 233.5159304 - 11974.38348 \cdot T^{-1} - 36.50633536 \ln T \\ & + (-45.08004597 \cdot T^{-1} + 2131.318848 \cdot T^{-2} + 6.714256299 \cdot T^{-1} \ln T)(P - P_s) \\ & + (0.008393915212 \cdot T^{-1} - 0.4015441404 \cdot T^{-2} - 0.00124018735 \cdot T^{-1})(P - P_s)^2 \end{aligned} \quad [17]$$

Where, P_s is saturation pressure of water and is assumed to be 1 bar at temperature below 100 °C. P is in bar, and T is in Kelvin.

Bicarbonate anion dissociation

K_{bi} can be calculated at various temperatures and pressures but the expression is only valid from 0°C to 100°C and from 1 to 3000 bar (39).



$$K_{bi} = C_{H^+} C_{CO_3^{2-}} / C_{HCO_3^-} \quad [19]$$

$$\begin{aligned} \ln K_{bi} = & -151.1815202 - 0.088695577T - 1362.259146 \cdot T^{-1} + 27.79798156 \ln T \\ & - (29.51448102 \cdot T^{-1} + 1389.015354 \cdot T^{-2} + 4.419625804 \cdot T^{-1} \ln T)(P - P_s) \\ & + (0.003219993525 \cdot T^{-1} - 0.1644471261 \cdot T^{-2} - \\ & 0.0004736672395 \cdot T^{-1} \ln T) \left(P - P_s \right)^2 \end{aligned} \quad [20]$$

Where, P_{H_2O} is saturation pressure of water and it is assumed 1 bar at temperature below 100°C. P is in bar, and T is in Kelvin.

Water dissociation

This data for this reaction are taken from Duan and Li (2007) (39).



$$K_{wa} = C_{H^+} C_{OH^-} \quad [22]$$

$$\begin{aligned} \text{Log}K_{wa} = & -4.098 - 3245.2 \cdot T^{-1} + 2.2362 \cdot 10^5 \cdot T^{-2} - 3.984 \cdot 10^7 \cdot T^{-3} + \\ & (13.957 - 1262.3 \cdot T^{-1} + 8.5641 \cdot 10^5 \cdot T^{-2}) \log \rho_{H_2O} \end{aligned} \quad [23]$$

Where ρ_{H_2O} is the density of water in unit g/cm³ and T is temperature in Kelvin.

Electroneutrality

The electroneutrality of the H₂O–CO₂ system can be described with the following equation:

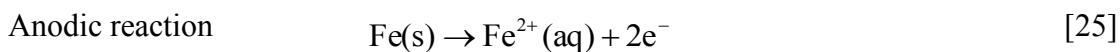
$$C_{H^+} = C_{OH^-} + C_{HCO_3^-} + 2C_{CO_3^{2-}} \quad [24]$$

Speciation of carbonic species

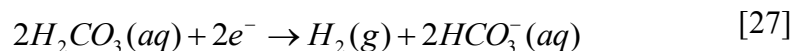
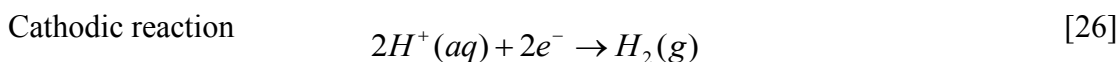
The species in the solution such as H₂CO₃, HCO₃⁻, CO₃²⁻, H⁺ and OH⁻ can be calculated using the above equations. H₂CO₃ and H⁺ are the main reactants in cathodic reactions at low pH while H₂CO₃ and HCO₃⁻ are the main reactants at high pH condition. CO₃²⁻ species is the main reactant for FeCO₃ (siderite) formation when it reacts with Fe²⁺. Fe²⁺ is a product of the anodic reaction.

Electrochemical reaction

Hydrogen ion (hydronium ion) and carbonic acid are the main reducible species for the metal. The concentration of hydrogen ion and carbonic acid will be used to calculate the current density from both reducible species and finally a corrosion rate.



Anodic reaction is an oxidation step of iron. Fe(s) is oxidized by oxidation agent to form Fe²⁺, this anodic reaction is pH dependent according to the mechanism described by Bockris, *et al.* (97) .



The cathodic reaction is a reduction step of carbonic acid and hydrogen ions. H₂CO₃ and H⁺ are the agents which oxidize Fe(s) to form Fe²⁺ (23)

CHAPTER 5: EXPERIMENTAL SETUP AND PROCEDURES

Water chemistry in high pressure CO₂ environments

The present experimental matrix was designed to validate the accuracy of the water chemistry model in a temperature range of up to 100°C and at CO₂ pressures of up to 600 bar.

Three types of experiments were selected for the model validation as follows:

- Solubility of CO₂ in Water.
- Solubility of Water in CO₂.
- pH of the system.

Solubility of CO₂ in water (x_{CO_2})

The objective of the experiments was to compare the mole fraction of dissolved CO₂ in water with predicted data. All of the experiments related to the study of the water chemistry were performed in the 20 liter autoclave pictured in Figure 4.



Figure 4: 20 liter high pressure autoclave used in this study.

The 20 liter autoclave was filled with 10 liters of de-ionized water and CO₂ was added to the required pressure. Care was taken to ensure that the system had reached equilibrium before any measurement was performed.

50 milliliter of water was sampled from the high pressure autoclave to the low pressure 500 milliliter sampling bomb. The sampling bomb was previously purged with CO₂ and its initial pressure was set at 2 bars. The 50 milliliter liquid sample taken under pressure from the 20 liter autoclave was then introduced inside the sampling bomb and allowed to de-gas and to reach equilibrium. The sampling bomb was designed so that the consequent rise in pressure (and change in temperature) would always be relatively small, keeping the overall pressure under 10 bars. In these conditions, Henry's law could be used to calculate the CO₂ content in the water. The total amount of CO₂ present in the

sampling bomb was then evaluated and enabled the calculation of the amount of dissolved CO_2 initially present in the 50 milliliters liquid sample taken from the autoclave. The key step in this measurement method was to have a very good control of the volume of liquid sampled. The experimental set-up for solubility CO_2 in water is shown in Figure 5 and Figure 6.

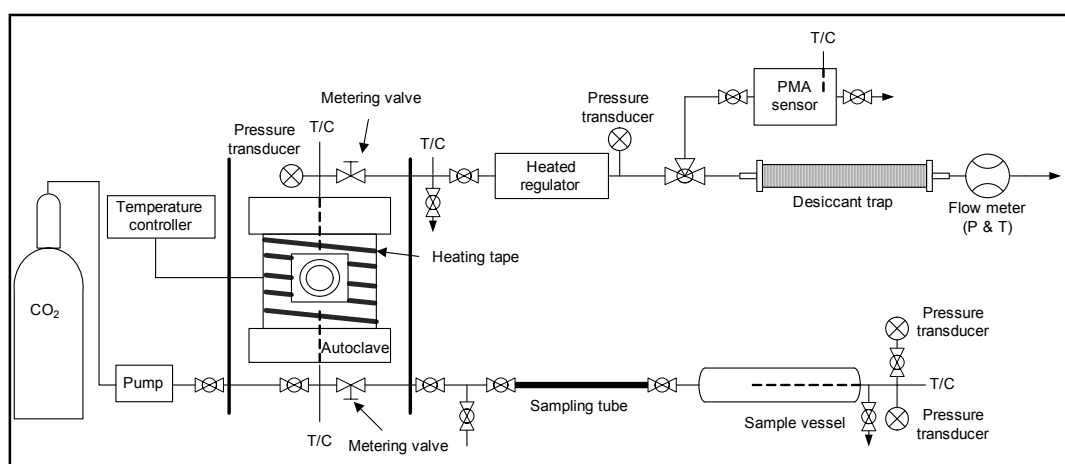


Figure 5: Schematic diagram for the solubility of water in CO_2 and CO_2 in water experimental set-up.

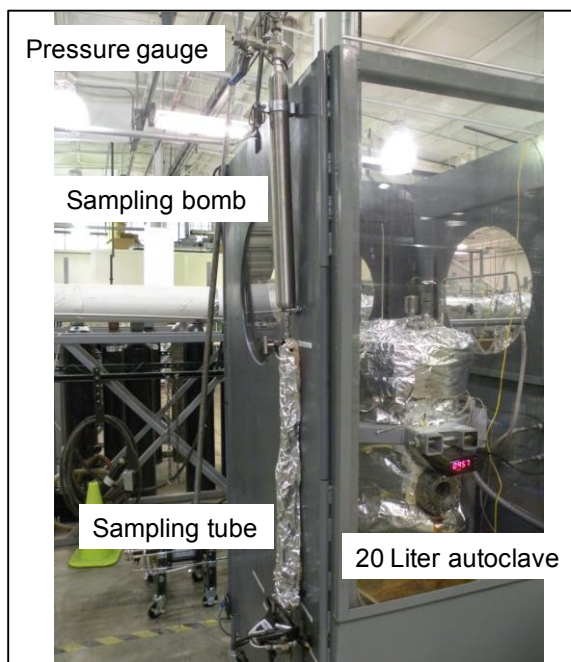


Figure 6: Experimental set-up developed to measure the solubility of CO₂ in water.

Solubility of water in CO₂ (yH₂O)

The objective of this part was to determine the mole fraction of water vapor in the CO₂ gas phase. The measured data was compared to predicted data that was developed using Equations 1 through 7. The 20 liter autoclave was filled with 4 liters of deionized water in order to simulate CO₂-water systems. Again, special care was taken to ensure that the system had reached equilibrium before any measurement was performed. Any condensation of water vapor due to the pressure drop during sampling was prevented by applying heating tape along the tubing from the autoclave to the measurement setup. Two independent methods were used to measure the amount of water vapor in the gas phase: an absolute humidity sensor and a desiccant trap. The screening and selection of measurement techniques for measuring water content in gas phase was completed by Yarrison, *et. al.* (98).

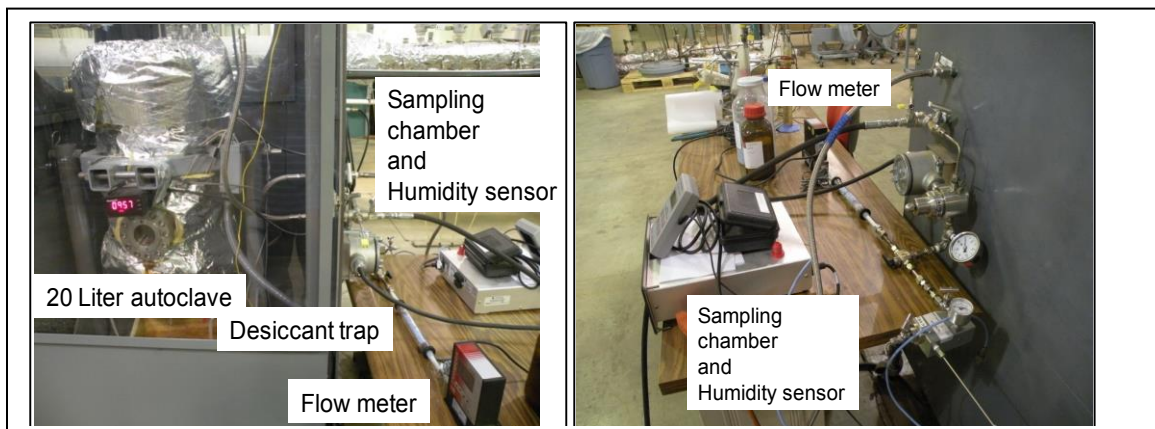


Figure 7: Experimental set-up for the measurement of the solubility of water in CO₂.

Figure 7 shows the experimental set-up for the desiccant trap and humidity sensor. The principle behind the humidity sensor method was to bleed and depressurize a small stream of the gas phase (containing water vapor) from the autoclave inside a small sampling chamber equipped with an absolute humidity sensor. A ‘Moisture monitor series 35’ sensor made by GE Infrastructure Sensing was used to monitor the dew point temperature and partial pressure of the water vapor. The temperature and pressure in the sampling chamber were carefully measured. The dew point measurement inside the small vessel was then used to back-calculate the molar percentage of water vapor in the gas stream (99). The ratio of the water vapor partial pressure to the total pressure of the systems was proportional to the water containing CO₂. The humidity sensor was made from an aluminum oxide with a working temperature range from -110 to 70°C. The tubing and sampling chamber was heated using the heating tape to prevent any condensation occurring on the surface.

The desiccant trap method involved the slow bleeding and depressurizing of a small stream of the gas phase (containing water vapor). This stream was passed through a

tube full of dehydrated desiccant material (CaCl_2 and zeolite molecular sieve A), which subsequently trapped the water. The CaCl_2 contained CoCl_2 as an indicator of its hydration, this changed color from blue to purple/pink once it became hydrated by water vapor. A mass flow meter located downstream from the tube measured the dry CO_2 mass flow rate. The molar content of the gas stream was calculated based on the mass change of the desiccant and the total CO_2 mass flow rate.

pH of the system

pH measurement is a very practical way to determine if the chemistry of the water/ CO_2 solution is modeled properly. A high-pressure glass pH probe and Ag/AgCl reference electrode were used to measure the concentration of hydrogen ions (hydronium ions) at three different temperatures and at pressures up to 80 bar, as shown in Figure 8. The pH probe and reference electrode were calibrated at ambient temperature and pressure using buffer solutions at pH 4.0, 7.0 and 10.0. The probe measurement error is ± 0.2 unit, as indicated by the probe manufacturer. The 20 liter autoclave was filled with 4 liters of deionized water and CO_2 was introduced in the vessel until equilibrium was reached. The challenge in such a test was to find a suitable pH probe and a methodology that can be applied in high partial pressure CO_2 environments. The current pH probe proved relatively reliable but was lacking in accuracy.



Figure 8: High pressure glass pH probe and Ag/AgCl reference electrode used to measure hydrogen ion (hydronium ion) concentration.

Corrosion inhibition in high pressure CO₂ environment

Two types of generic corrosion inhibitor were reviewed and selected for corrosion inhibitor testing, “DETA imidazoline” (K1) and “DETA imidazoline” plus thiosulfate (K4); see Figure 1 and Figure 2 above.

A Gamry Reference 600 potentiostat was used for electrochemistry measurements. Cylindrical platinized niobium was used as a counter electrode. A saturated Ag/AgCl reference electrode and pH electrode which can withstand pressures up to 2000psi and temperature 110°C are used for this experiment.



Figure 9: 2 liter autoclave equipped for electrochemistry measurements.

Experiments were conducted in a 2 liter autoclave, as shown in Figure 9. X65 carbon steel was used for specimens for all experiments. Cylindrical specimens were used for electrochemical measurements such as linear polarization, electrochemical impedance spectroscopy and potentiodynamic sweeps. Rectangular specimens were used for weight loss measurements and surface analyses, such as scanning electron microscopy with energy-dispersive X-ray spectroscopy and profilometry by infinite focus microscopy. Sample geometries are shown in Figure 10. Before the start of each experiment, the carbon steel specimen surfaces were polished with 200, 400 and 600 grit SiC paper and rinsed with isopropyl alcohol. The surface area is calculated from measurements obtained using a caliper after polishing. The autoclave was filled with 1 weight percent of NaCl. The required concentration of corrosion inhibitor was injected

into the autoclave. The solution was heated to the desired temperature and the CO₂ gas was pumped into the autoclave until the required pressure is reached.

Weight loss test

The pre-weighed specimens are immersed in the autoclave vessel and the desired amount of corrosion inhibitor was injected into the autoclave solution. The pressure and temperature were increased in the sealed autoclave until the desired equilibration point is achieved. After exposure, the specimens were washed with deionized water then isopropyl alcohol before weight loss is measured. This testing follows the ASTM standard G31 (100). For specimens that had a corrosion product such as siderite, Clarke solution was used to facilitate its removal followed by washing with deionized water and isopropyl alcohol. Clarke solution was prepared following the ASTM G1 Standard Practice for Preparing, Cleaning, and Evaluating Corrosion Test Specimens. 1000 milliliter hydrochloric acid (HCl, sp gr 1.19), 20 gram antimony trioxide (Sb₂O₃) and 50 gram stannous chloride (SnCl₂) are required to prepare Clarke solution to remove corrosion products. Specimens were fully immersed in the Clarke solution and stirred to form a homogenous solution. The cleaning process was repeated on specimens several times and the mass loss measured after each cleaning by weighing the specimen. The measured mass loss was plotted until the result showed a plateau (101).

The corrosion rate from the weight loss test was obtained as follows:

$$\text{Corrosion.rate(mm/ yr)} = (KxW)/(AxTxD) \quad [28]$$

Where:

K = a constant, 8.76×10^4

T = time of exposure in hours,

A = area in cm^2 ,

W = mass loss in grams, and

D = density of carbon steel in g/cm^3 , 7.86



Figure 10: Specimens for electrochemistry measurement and weight loss.

Linear polarization resistance (LPR) test

The linear polarization resistance technique was used to monitor in-situ corrosion rate. The specimen was polarized $\pm 5\text{mV}$ at corrosion potential during LPR measurement. A scan rate of $0.125\text{mV}/\text{s}$ is applied for the duration of the LPR test. The resistance measured using the LPR technique includes solution resistance, which can be determined by running Electrochemical Impedance Spectroscopy (EIS).

The Stern-Geary equation was used to calculate corrosion rates from linear polarization resistance measurements. The Stern-Geary constant can be empirically calibrated using the corrosion rate from weight loss and potentiodynamic sweeps. The second set is corrosion testing with addition of corrosion inhibitor K1. The B value of K1

was 17mV, which was obtained from Chokshi experiment when the b_a value was 60 mV/decade and the b_c value was 110 mV/decade (102) (103). The third set of experiments is corrosion testing with corrosion inhibitor K4. The same B value was applied for corrosion inhibitor K4.

$$B = \frac{b_a \cdot b_c}{2.3 \left(b_a + b_c \right)} \quad [29]$$

$$i_{\text{corr}} = \frac{B}{R_p \cdot A} \quad [30]$$

$$\text{Corrosion.rate}(mm/yr) = 1.16 * i_{\text{corr}} \quad [31]$$

Polarization resistance (R_p) measured by LPR included the solution resistance (R_s) and can be corrected manually. Solution resistance can be measured using the EIS technique at the end of the experiment. The Stern-Geary constant unit is in Volts while A is surface area of electrochemical specimen in m^2 .

Electrochemical impedance spectroscopy (EIS) test

Electrochemical impedance spectroscopy was conducted after completion of linear polarization resistance measurements. Impedance measurements were performed on X65 specimens in solution in the absence or presence of corrosion inhibitors in a frequency range 100 KHz to 5 mHz. All the measurements were carried out with a Gamry potentiostat. Solution resistance and polarization resistance can be measured using this method.

Potentiodynamic sweep test

In the potentiodynamic polarization technique, the metal electrode is anodically polarized 200mV over corrosion potential and cathodically polarized -600mV over corrosion potential at a constant rate (0.166mV/s). A scan rate 0.16mV/s was applied for cathodic sweep and 0.1mV/s scanned rate was used for anodic sweep. Potentiodynamic sweeps were done after electrochemical impedance spectroscopy measurements.

Scanning electron microscopy and energy-dispersive X-ray spectroscopy

Scanning electron microscopy (SEM) was used to study the morphology of the corroded surface in the presence and absence of the inhibitors while EDS was used to determine the chemical composition of surface specimens with and without corrosion inhibitor. The specimens were thoroughly washed with deionized water before placing in the SEM.

Optical measurement and analysis using infinite focus microscope (IFM)

Infinite focus microscopy (IFM), a type of profilometer, was used to characterize the surface topography of steel and measure the pitting width and depth. Penetration rate of pitting can be measured using this equipment. A color picture of the surface after experiment can also be taken using the IFM.

CHAPTER 6: RESULTS AND DISCUSSIONS

Water chemistry in high pressure CO₂ environments

Solubility of CO₂ in water (xCO₂)

The predicted concentration of CO₂, H₂CO₃, HCO₃⁻ and CO₃²⁻ over partial pressures of CO₂ up to 80 bar is shown in Figure 11 to Figure 14. The concentrations of H₂CO₃ and HCO₃⁻ follow the same trend as the solubility of CO₂ in water. That is, the concentrations increased with increasing pressure but decreased with increasing temperature. However, the concentration of CO₃²⁻ increased with increasing pressure and temperature.

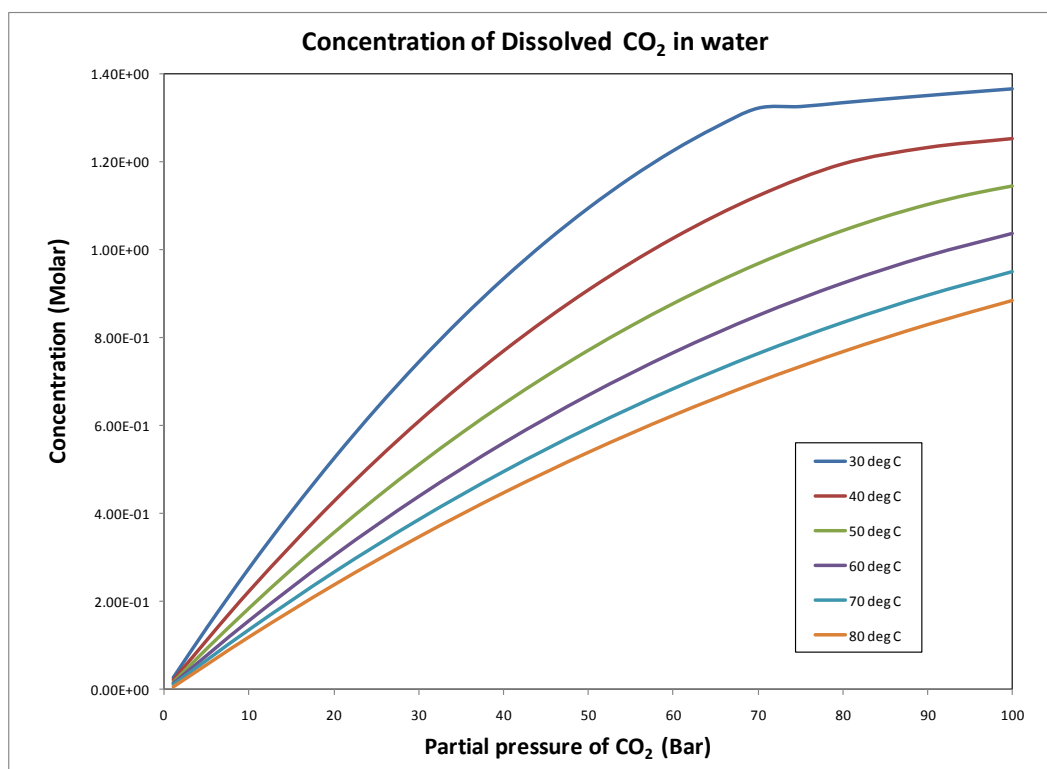


Figure 11: Calculated CO₂ content in water with partial pressure of CO₂.

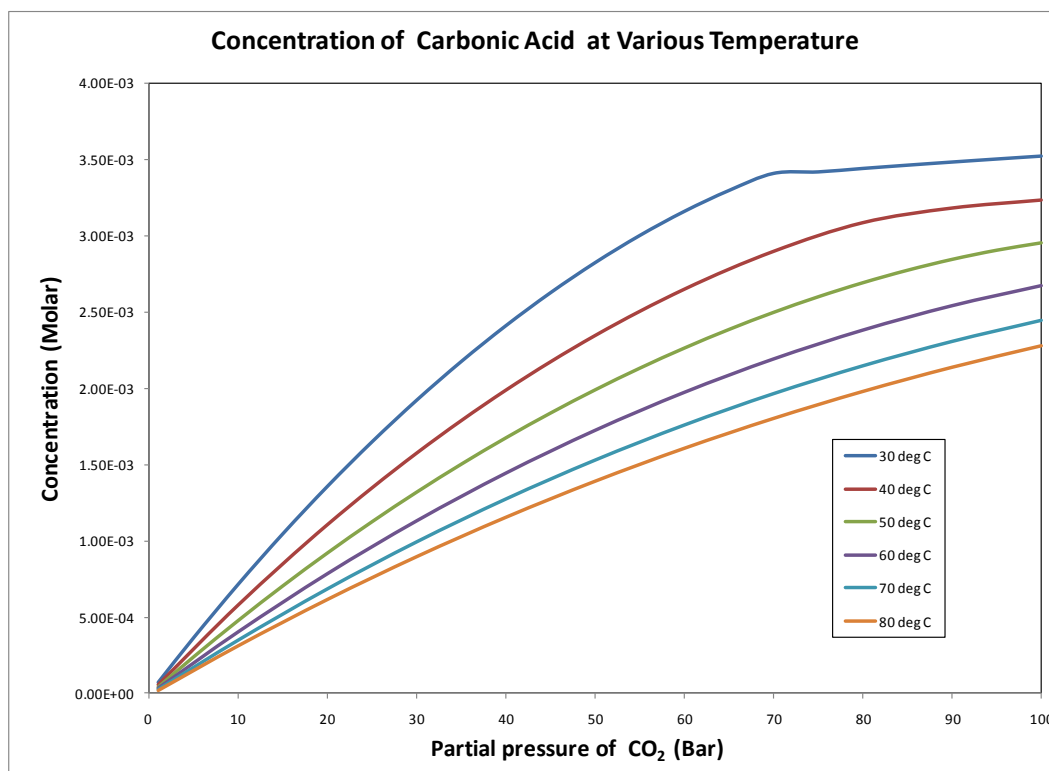


Figure 12: Calculated H₂CO₃ with partial pressure of CO₂.

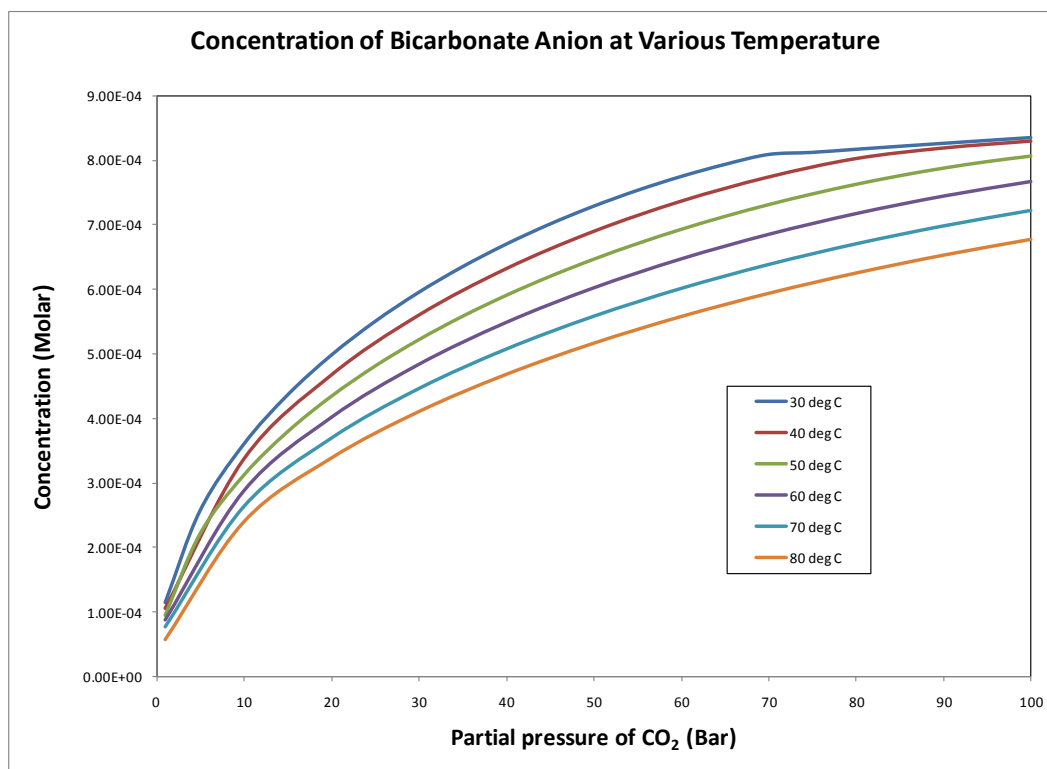


Figure 13: Calculated HCO_3^- with partial pressure of CO_2 .

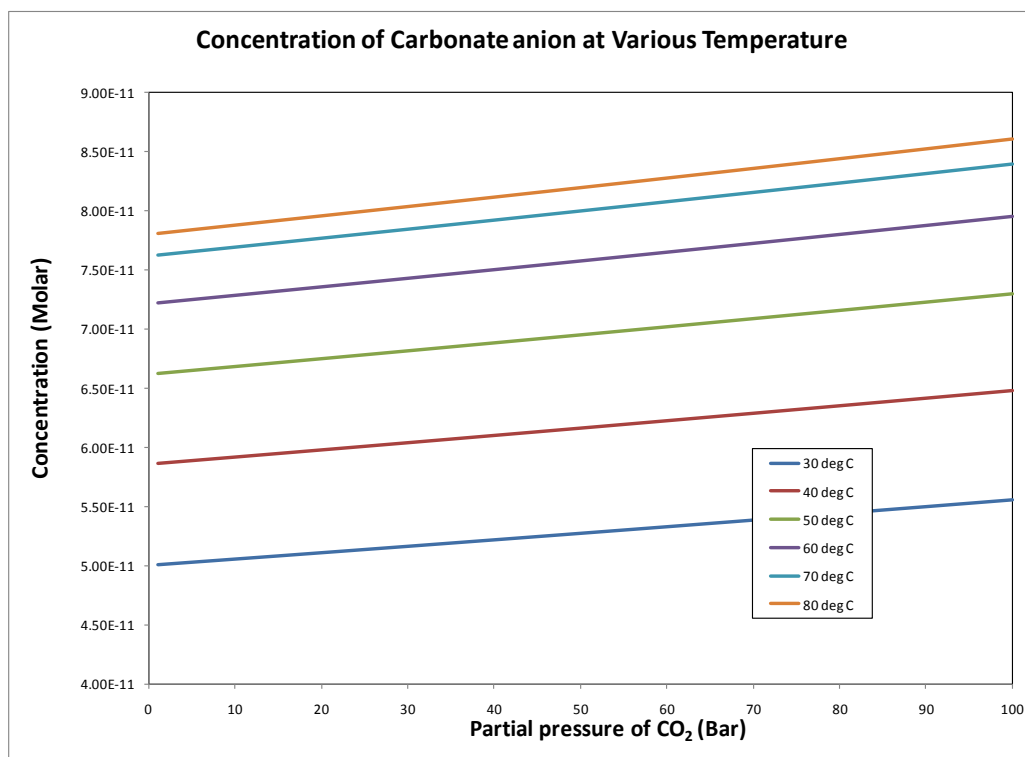


Figure 14: Calculated CO_3^{2-} with partial pressure of CO_2 .

Figure 15 to Figure 17 show the experimental data for the solubility of CO_2 in water with mole fraction (x_{CO_2}) as a function of CO_2 partial pressure (pressure from 0 to 100 bar at temperature of 25, 40, and 60° C, respectively). The figures suggest that, at the three temperatures, the amount of dissolved CO_2 increased as the CO_2 partial pressure increased. This is due to the increase in the amount of CO_2 molecules present in the gas phase and consequently dissolving in water. However, the increase in temperature led to a decrease in x_{CO_2} . It must be noted that as temperature increases, the solubility of CO_2 in water deviates further from Henry's law; that is, the domain of validity of Henry's law is 20 bars at 25° C, and only 8 bars at 60° C.

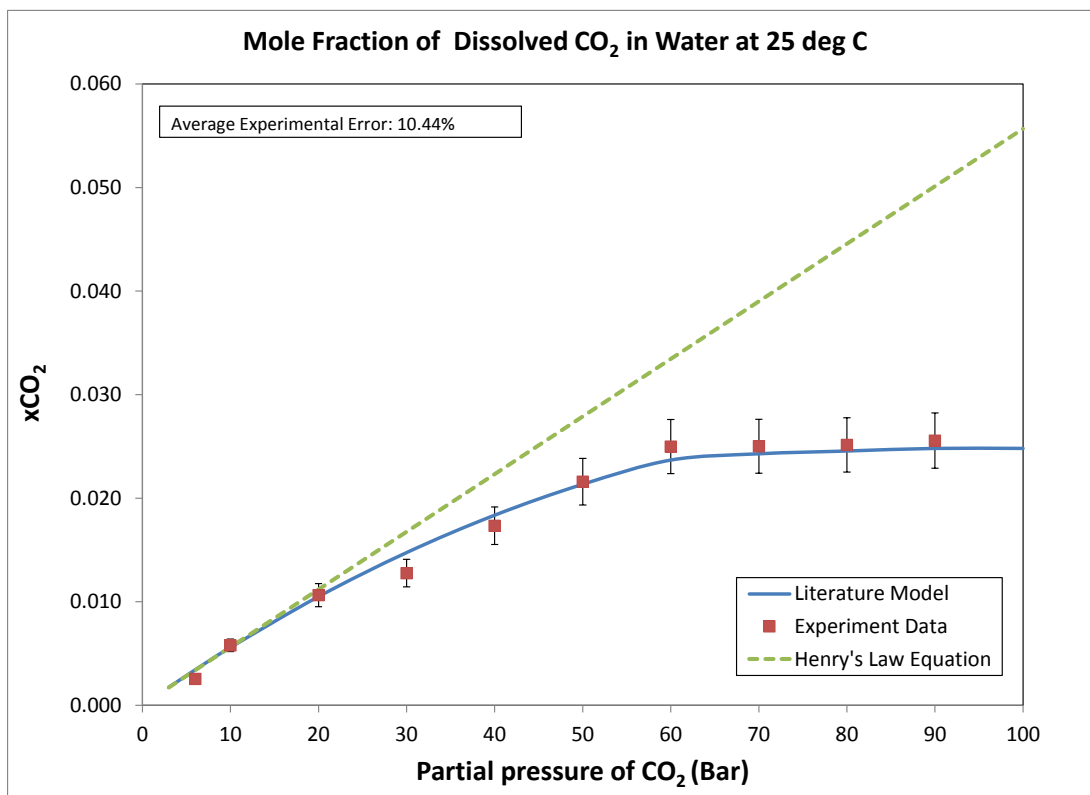


Figure 15: Comparison between experimental results and modeling for the solubility of CO₂ in water at 25°C.

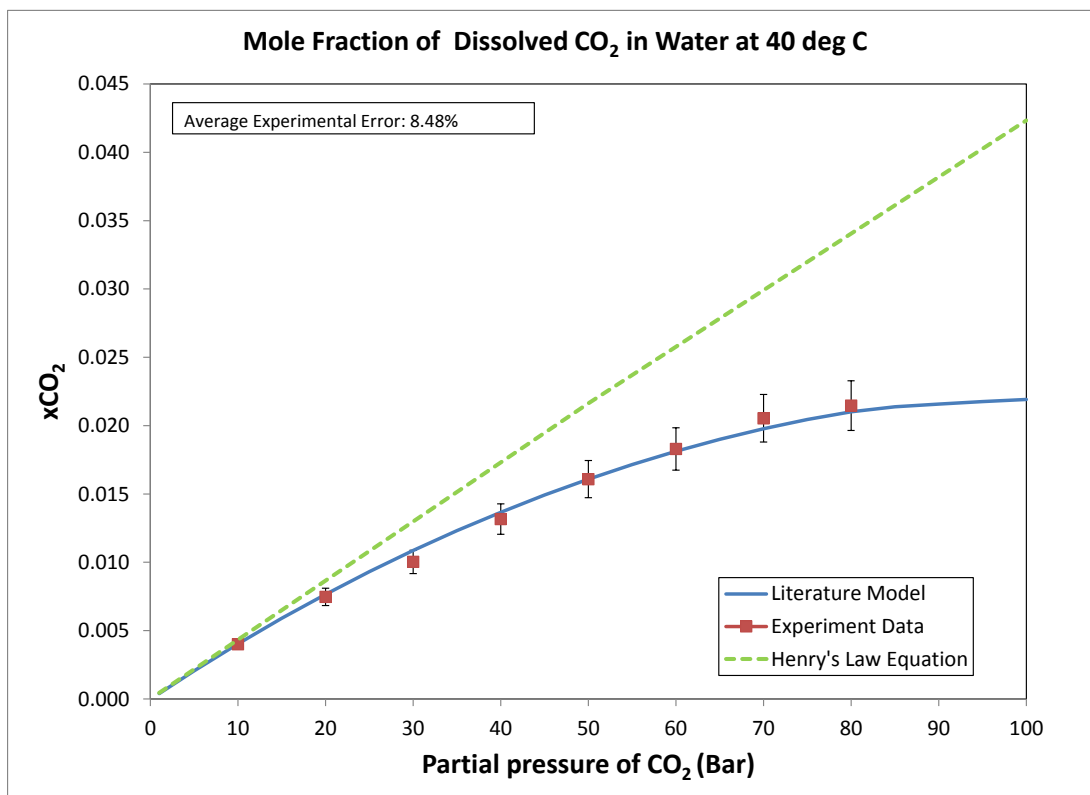


Figure 16: Comparison between experimental results and modeling for the solubility of CO₂ in water at 40°C.

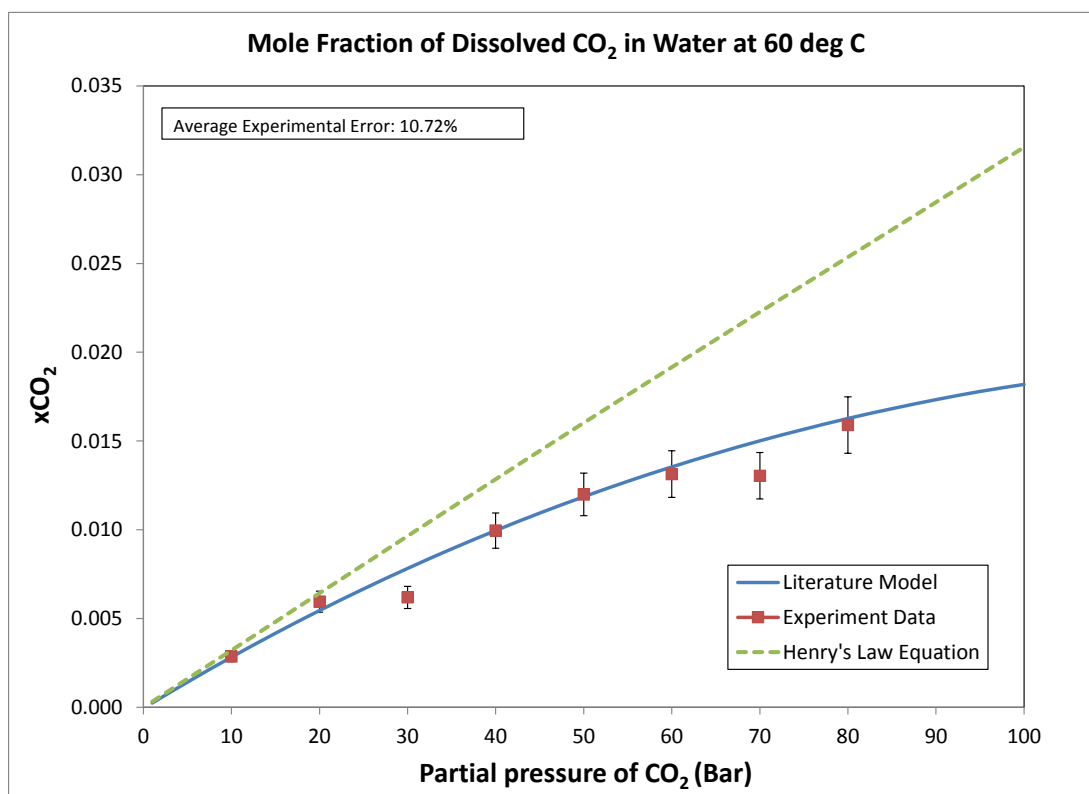


Figure 17: Comparison between experimental results and modeling for the solubility of CO₂ in water at 60°C.

Solubility of water in CO₂ (yH₂O)

Figure 18 shows the predicted mole fraction of H₂O in CO₂ in over partial pressure of CO₂ up to 100 bar. The solubility of water in CO₂ increased with increasing partial pressure of CO₂ and temperature.

Figure 19 to Figure 21 show the solubility of water in CO₂ in mole fraction (yH₂O) as a function of CO₂ partial pressure (pressure from 0 to 100 bar and temperatures of 25, 40, and 60° C, respectively). Two types of measurement, by humidity sensor and desiccant traps, were applied at temperatures of 25°C and 40°C; only the desiccant trap method was applied at 60°C. The figures suggest that at the three

temperatures, the amount of water soluble in liquid/supercritical CO₂ phase increases as the CO₂ partial pressure increases. The figures also show that the solubility of water in the CO₂ phase increases as the temperature increases.

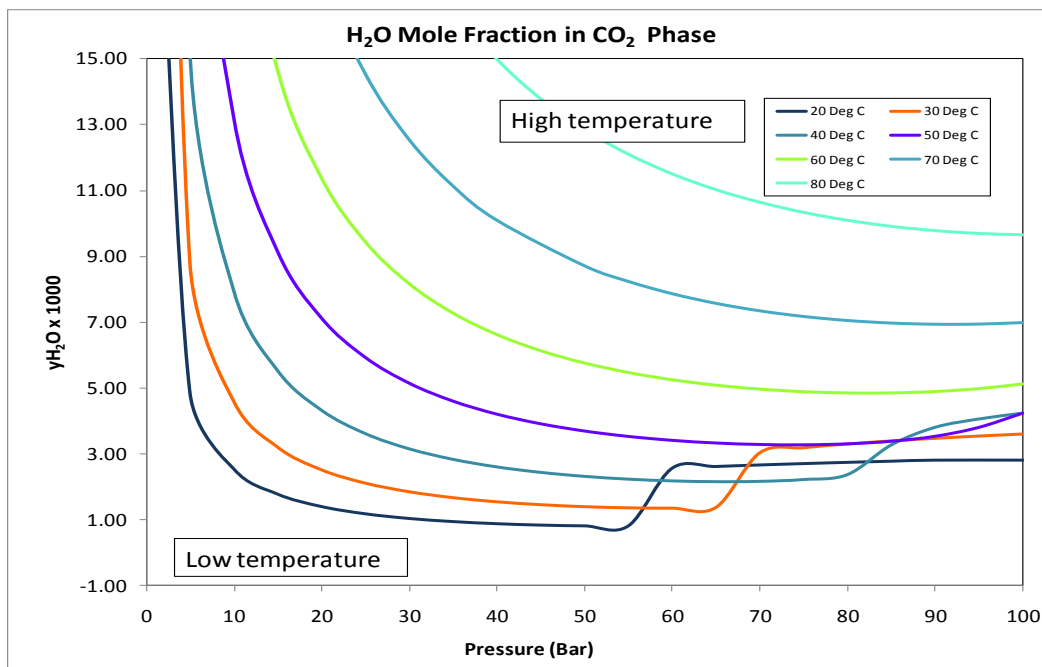


Figure 18: Calculated water content in CO₂ (gas phases).

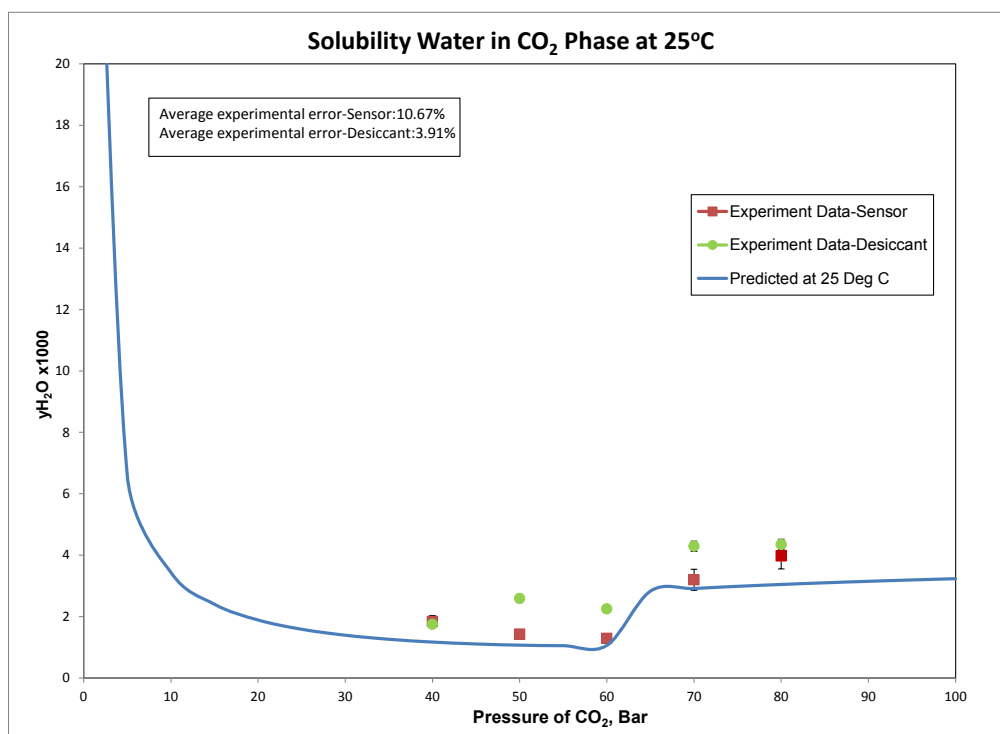


Figure 19: Comparison between experimental results and modeling for the solubility of water in CO₂ at 25°C.

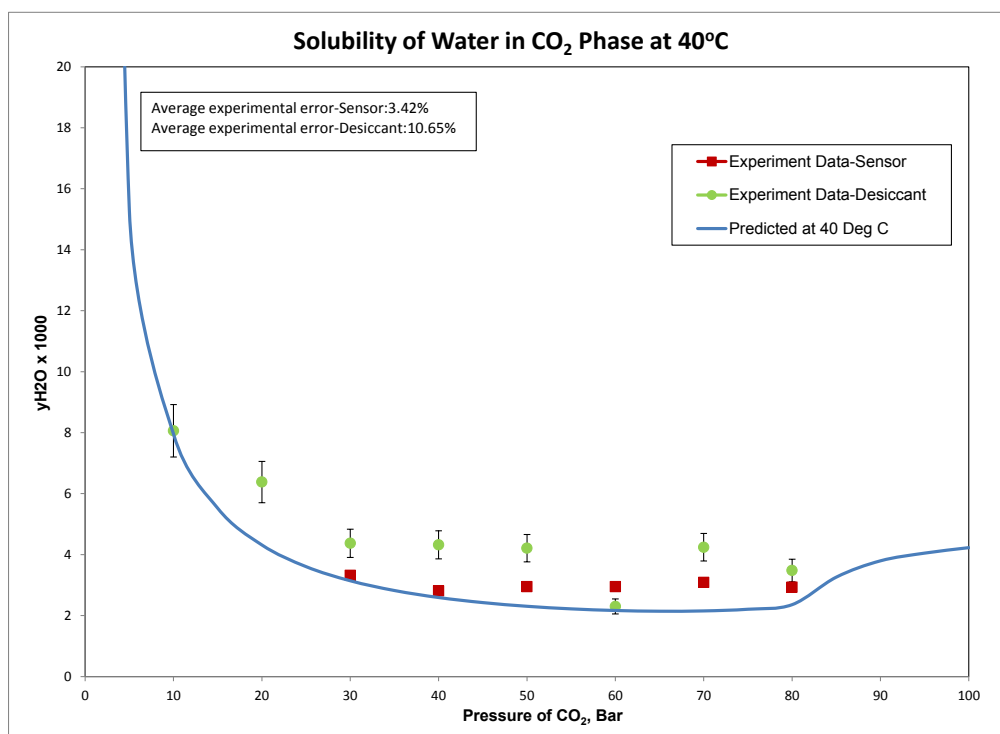


Figure 20: Comparison between experimental results and modeling for the solubility of water in CO₂ at 40°C.

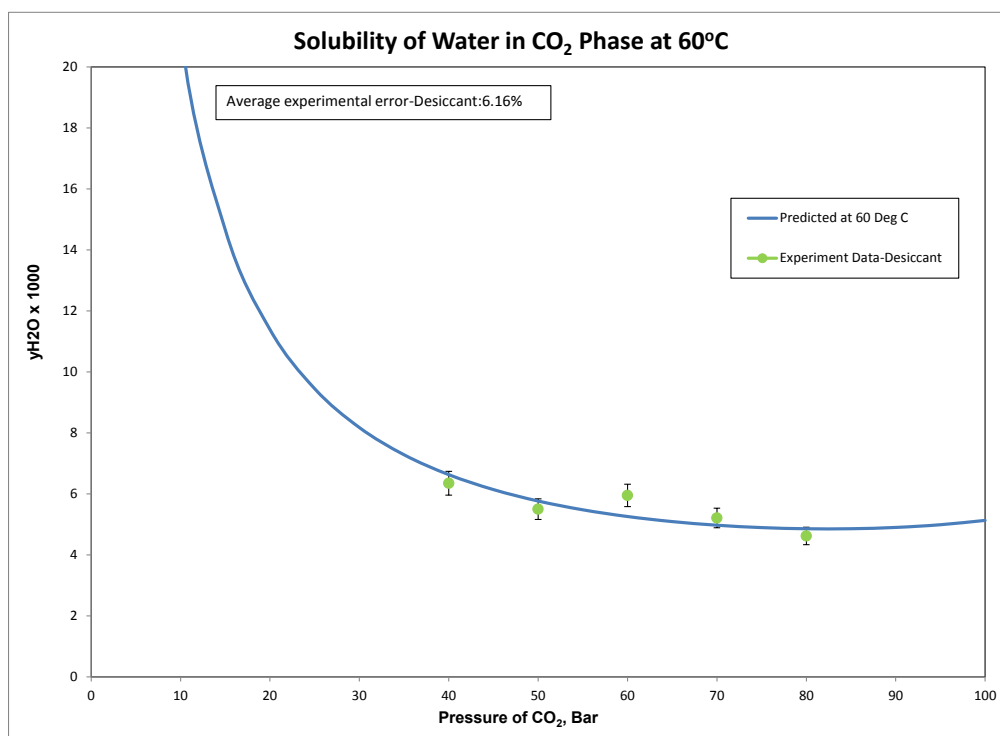


Figure 21: Comparison between experimental results and modeling for the solubility of water in CO₂ at 60°C.

pH of the system

Figure 22 to Figure 24 show pH measurement as a function of CO₂ partial pressure of 1 to 100 bar at 25°C, 40°C and 60°C, respectively. The results show that pH decreased with increasing partial pressure of CO₂. This is consistent with an increased carbonic acid concentration as the amount of dissolved CO₂ in water increases in line with increased CO₂ partial pressure. However, the increase in temperature led to no significant change in pH despite the fact that, as the temperature increased, a smaller amount of CO₂ was soluble in the water. Note that the probe measurement error is ± 0.2 pH units, as indicated by the probe manufacturer. The pH measurements started to deviate beyond the error bars at 30 bar of CO₂ when testing was conducted at 25°C and

40°C, as shown in Figure 22 and Figure 23. At 60°C, deviation out with the error bars commenced at 40 bar of partial pressure of CO₂ as shown in Figure 24.

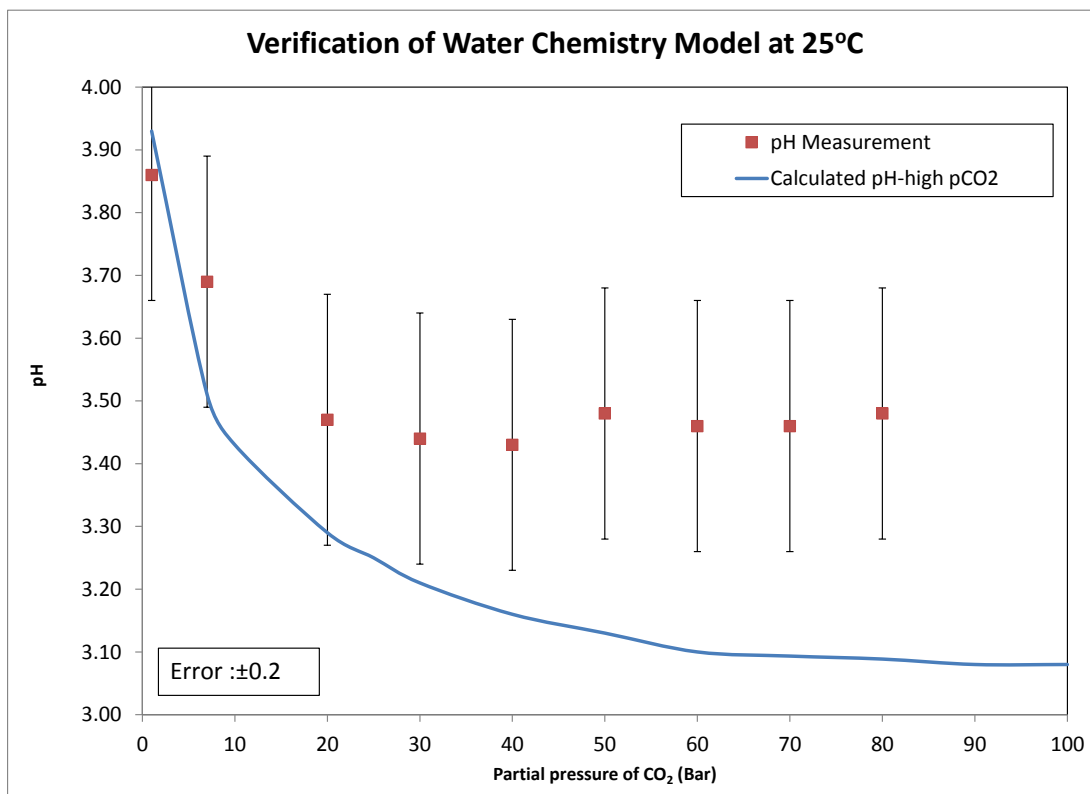


Figure 22: Comparison between pH measurements and modeling results at 25°C.

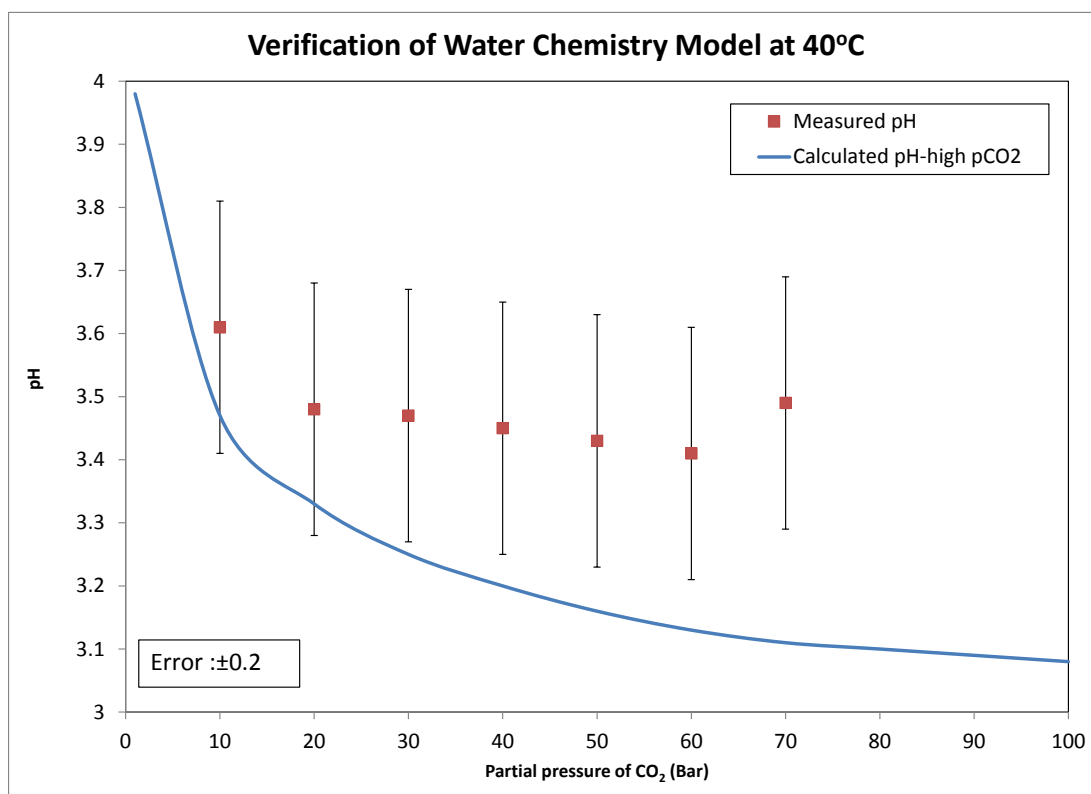


Figure 23: Comparison between pH measurements and modeling results at 40°C.

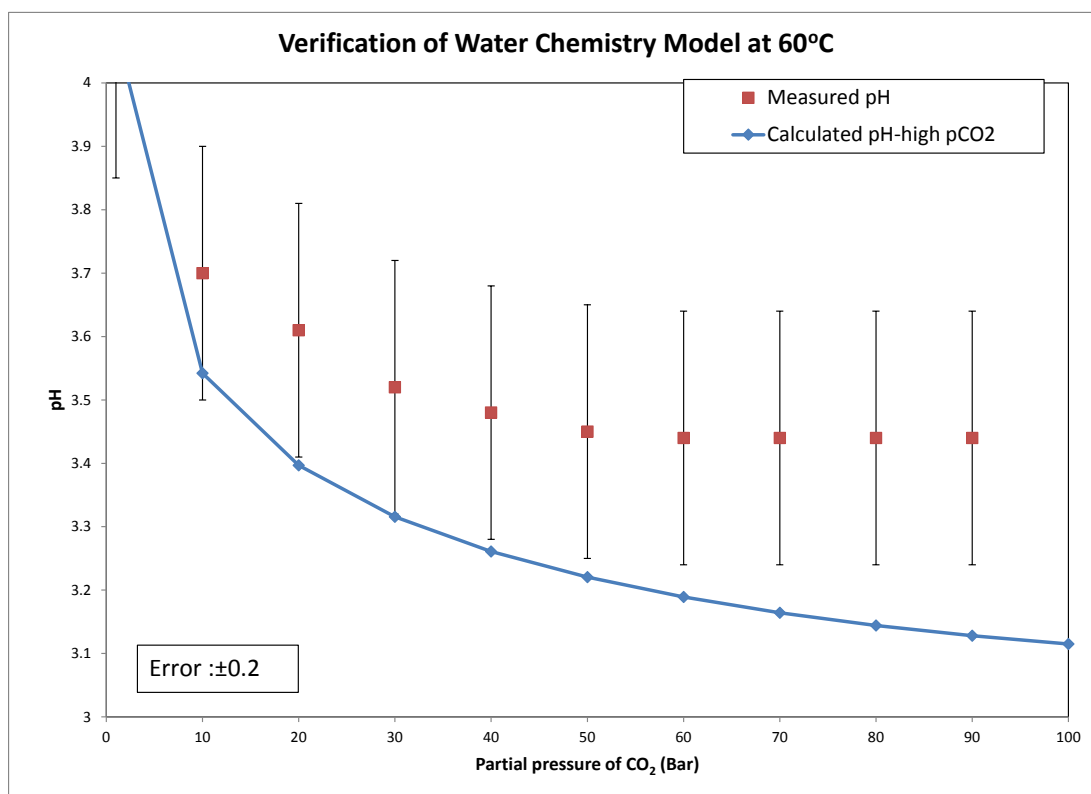


Figure 24: Comparison between pH measurements and modeling results at 60°C

Corrosion inhibition in high pressure CO₂ environment.

Two types of generic corrosion inhibitor were selected for evaluation at a high pressure and high temperature condition of 80 bar of CO₂ and 70°C. Three sets of experiments were run at this condition, including baseline testing where experiments were run without any corrosion inhibitor. Sets of experiments were run with corrosion inhibitor K1 (imidazoline-type) and K4 (which is K1 plus thiosulfate).

Baseline experiments

Figure 25 to Figure 27 show the results for corrosion experiments at 70°C and 80 bar of CO₂ by LPR, EIS and potentiodynamic sweep. The LPR results show that the corrosion rate remains low for the first 2 hours due to unsaturation with respect to CO₂ in

solution; gas phase CO_2 needs sufficient time to dissolve and hydrate to form carbonic acid. After formation of carbonic acid, it will partially dissociate to form H^+ . Consequently, in this system there are two principle reducible species, H_2CO_3 and H^+ . After two hours, the corrosion rate rapidly increases prior to decreasing and stabilizing at between 40 mm/yr and 60 mm/yr. The solution resistance was measured using the EIS technique at the end of the experiment. The solution was prepared from deionized water and consisted of 1 wt. % NaCl. The Tafel slope, see Figure 27, indicated that the electrochemical reactions were controlled by a mixed mechanism between charge and mass transfer.

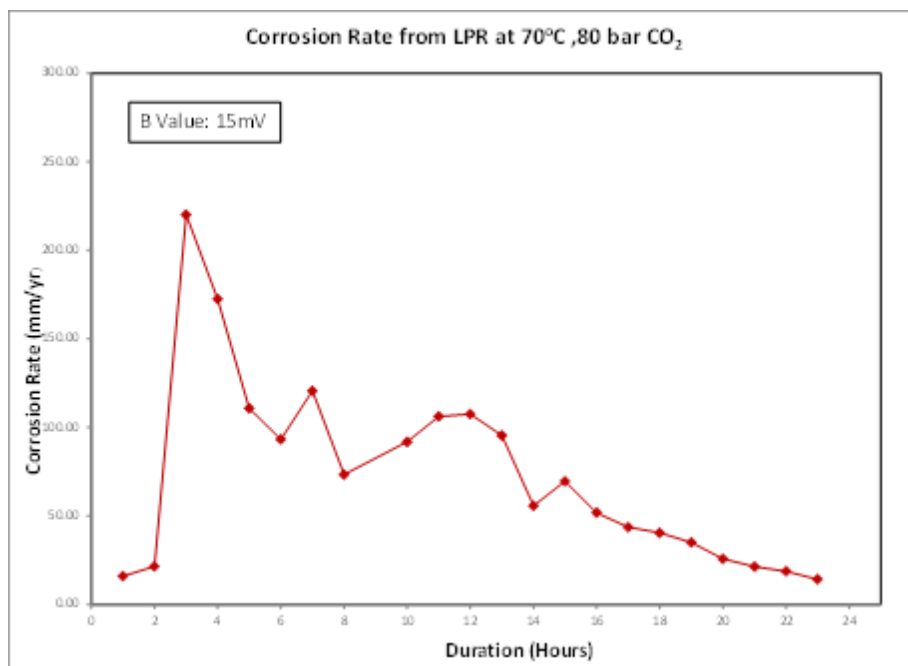


Figure 25: Corrosion rate with time by linear polarization resistance at 70°C and 80 bar of CO_2 in absence of corrosion inhibitor.

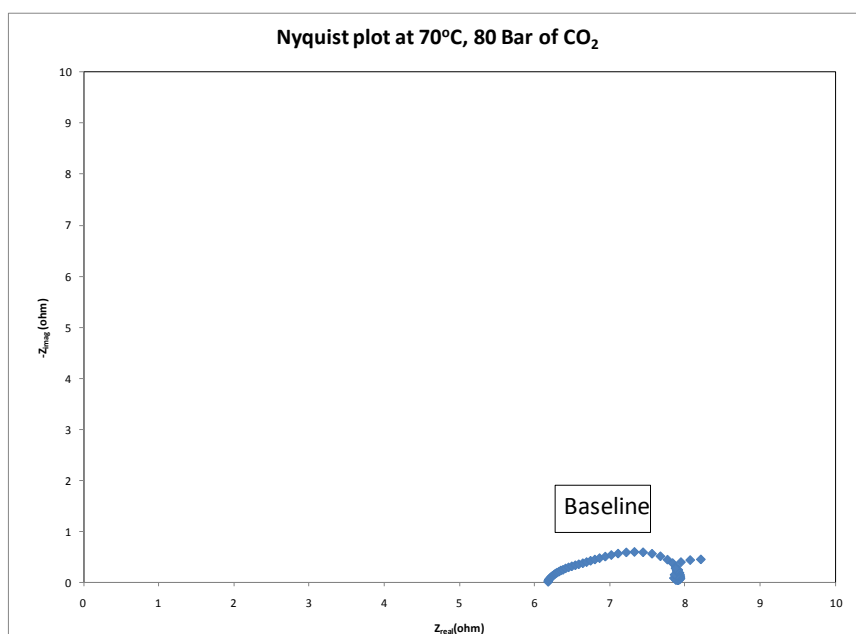


Figure 26: Solution resistance (R_s) and polarization resistance (R_p) by electrochemical impedance spectroscopy at 70°C and 80 bar of CO₂ in absence of corrosion inhibitor.

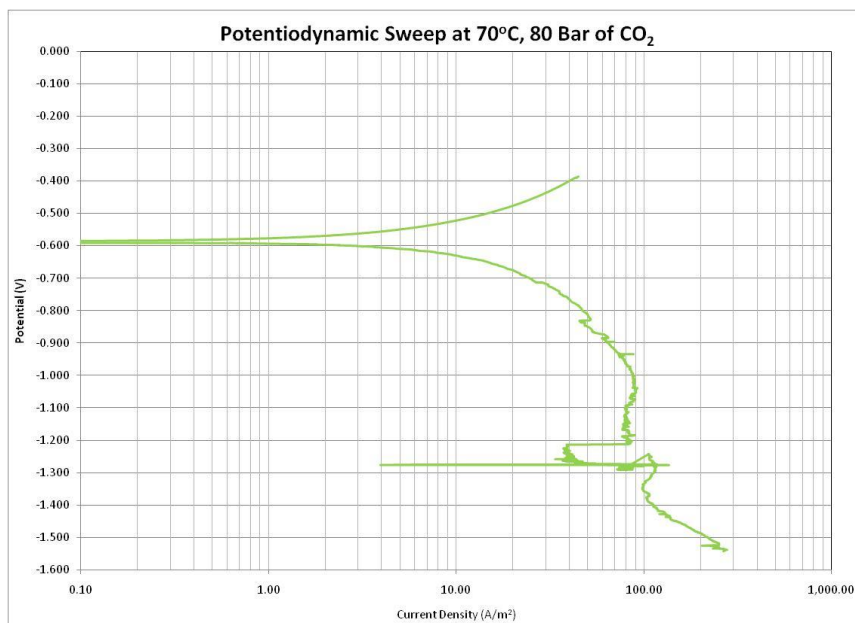


Figure 27: Potentiodynamic sweep at 70°C and 80 bar of CO₂ in absence of corrosion inhibitor.

Surface analysis on the surface of specimen by SEM and EDS

Ferrous ion (Fe²⁺) from the iron oxidation and dissolution reaction reacts with carbonate anion (CO₃²⁻) in the solution to form iron carbonate (FeCO₃), also known as siderite. The saturation of FeCO₃ in the solution increased over time until it reaches supersaturation. Once the concentrations of aqueous species become supersaturated, FeCO₃ deposition occurs on the metal surface. This can protect the metal surface from reducible species, or oxidants, and hinder the corrosion process. Figure 28 and Figure 29 show SEM and EDS data for the prismatic siderite crystals on the metal surface. These figures indicate, for the pure CO₂ system, iron carbonate formed on the metal surface.

According to the EDS, the detected elements in the corrosion product layer were iron (Fe), oxygen (O) and carbon (C), as shown in Figure 29; the detailed composition of

which is shown in Table 4. Figure 30 and Figure 31 show the surface morphology of steel and its elemental composition after the corrosion product layer was removed using Clarke solution. These figures show no evidence of pitting or localized corrosion attack on the metal surface. All the metal loss at this condition is due to general corrosion.

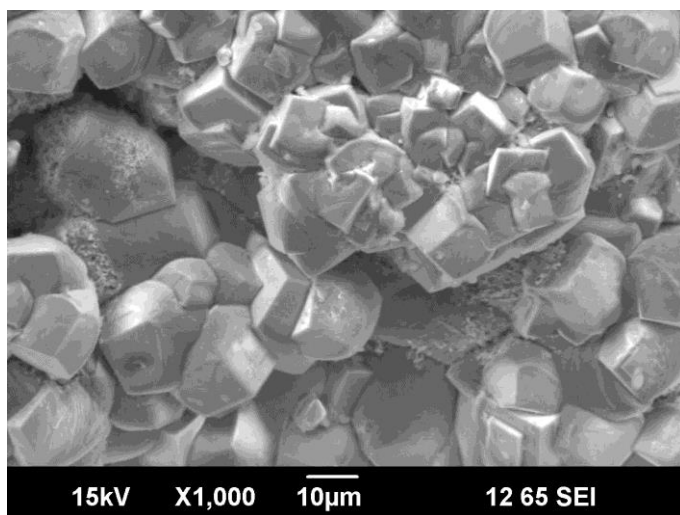


Figure 28: Surface of weight loss coupon at x1000 magnification for experiment condition of 70°C and 80 bar of CO₂ in absence of corrosion inhibitor.

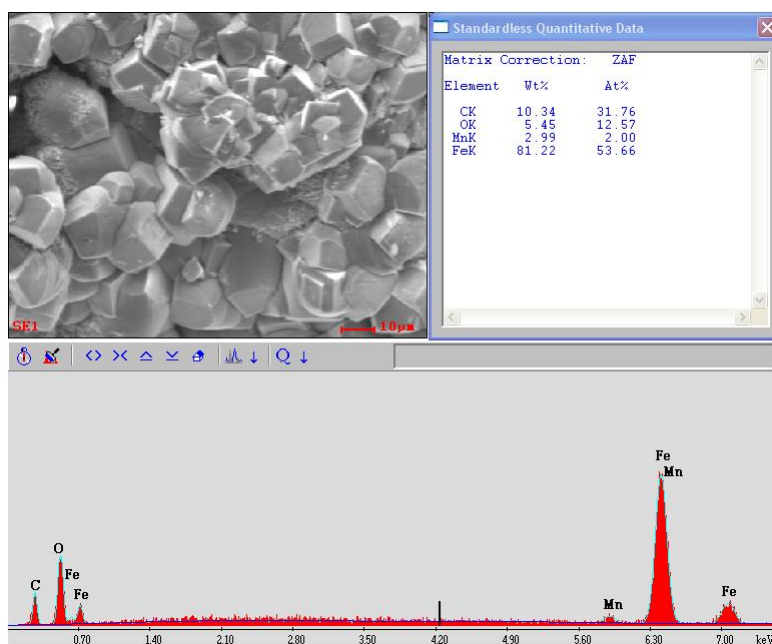


Figure 29 : Corrosion product layer composition by EDS at x1000 magnification for experiment condition of 70°C and 80 bar of CO₂ in absence of corrosion inhibitor.

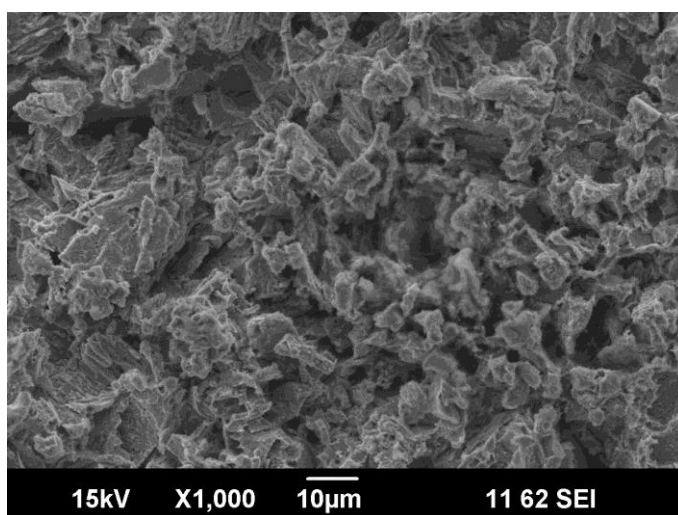


Figure 30: Surface of weight loss coupon at x1000 magnification after corrosion product was removed by Clarke solution for experiment condition of 70°C and 80 bar of CO₂ in absence of corrosion inhibitor.

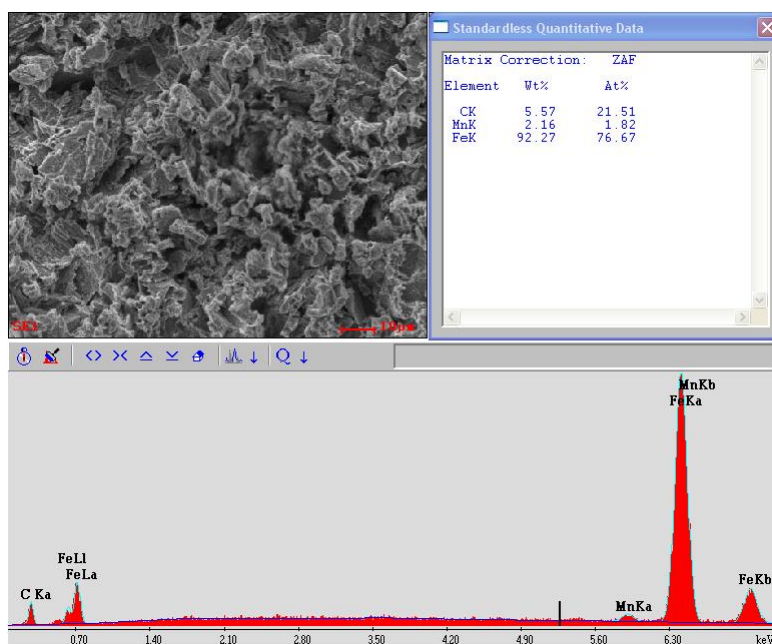


Figure 31 : Composition of bare surface by EDS at x1000 magnification after corrosion product was removed by Clarke solution for experiment condition of 70°C and 80 bar of CO₂ in absence of corrosion inhibitor.

Imidazoline-type corrosion inhibitor (K1)

Corrosion behavior in the presence of different concentrations of an imidazoline-type generic corrosion inhibitor, referred to as K1, was studied at a temperature of 70°C and CO₂ pressure of 80 bar. Figure 32 to Figure 34 show the electrochemistry results for corrosion inhibitor K1 at 5 different concentrations, *i.e.*, 50ppm, 100ppm, 400ppm, 800ppm and 1500ppm. Corrosion inhibitor was injected before pressurizing the autoclave to the required condition. Corrosion rate results from LPR show that the imidazoline-type inhibitor didn't reach a desirable corrosion rate at a practical concentration that could be applied in field operations. The lowest corrosion rate that can be achieved by K1 is 0.2mm/yr, but at 1500ppm; this took more than 20 hours achieve. A 100ppm

concentration of corrosion inhibitor reduced the corrosion rate to 0.5mm/yr after 24 hours.

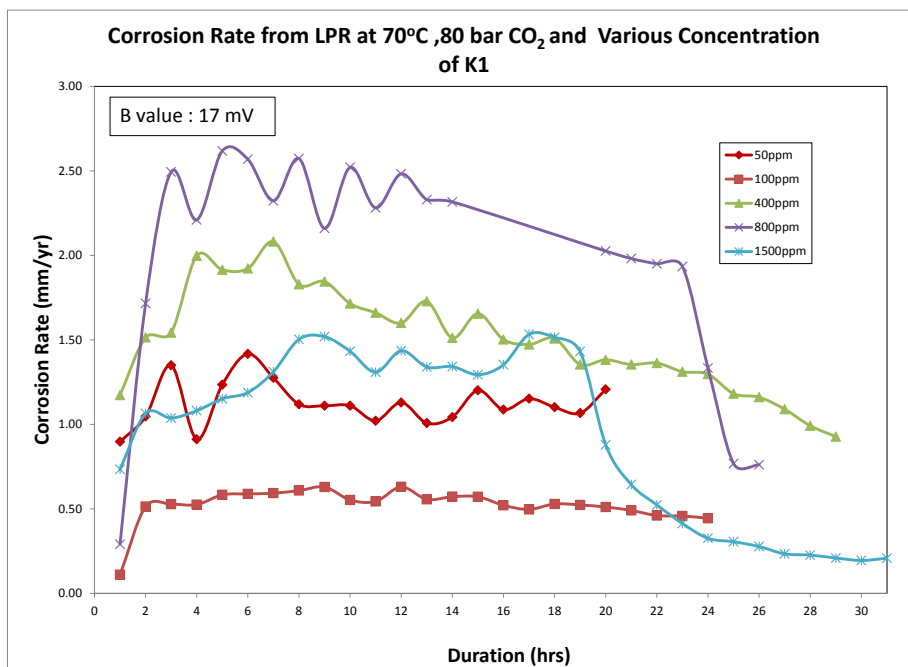


Figure 32: Corrosion rate with time by linear polarization resistance at 70°C, 80 bar of CO₂ and various concentrations of corrosion inhibitor K1.

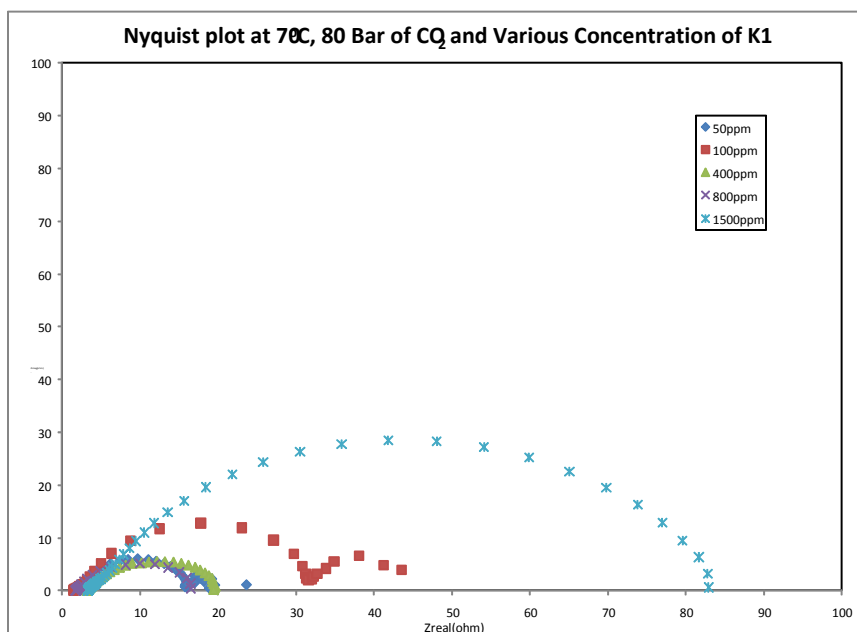


Figure 33: Solution resistance (R_s) and Polarization resistance (R_p) by electrochemical impedance spectroscopy at 70°C, 80 bar of CO₂ and various concentrations of corrosion inhibitor K1.

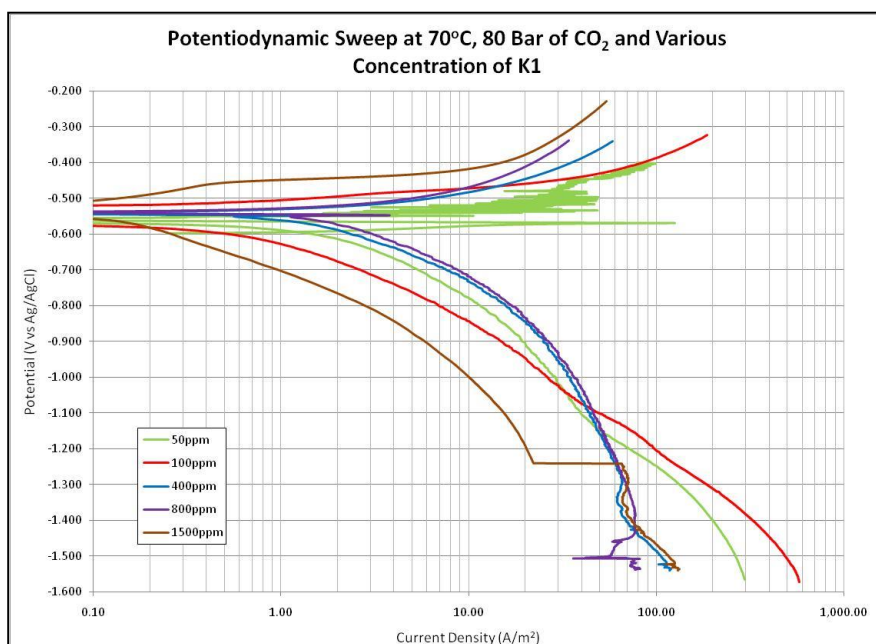


Figure 34: Result of potentiodynamic sweep at 70°C, 80 bar pressure of CO₂ and various concentrations of corrosion inhibitor K1.

The semicircles from the Nyquist plots can be used to measure solution resistance and polarization resistance for the corrosion rate calculation. The EIS technique was applied at the end of experiments and Figure 33 showed the polarization resistance increase with increasing inhibitor injected in the test solution. Corrosion rate can be calculated from the polarization resistance using Equation [30]. Solution resistance obtained from Electrochemical Impedance Spectroscopy (EIS) is used in the calculation of corrosion rate from the Linear Polarization Resistance (LPR) test. The Tafel slope in Figure 34 showed that the anodic and cathodic curves were controlled by charge transfer between steel and reducible species. Corrosion current density moved to the left with increasing concentration of K1.

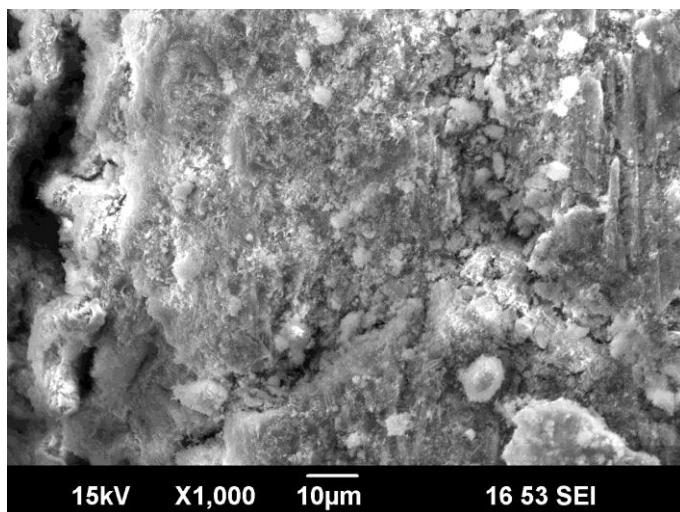


Figure 35: Surface of weight loss coupon at x1000 magnification and experiment condition of 70°C, 80 bar of CO₂ and 50ppm of K1.

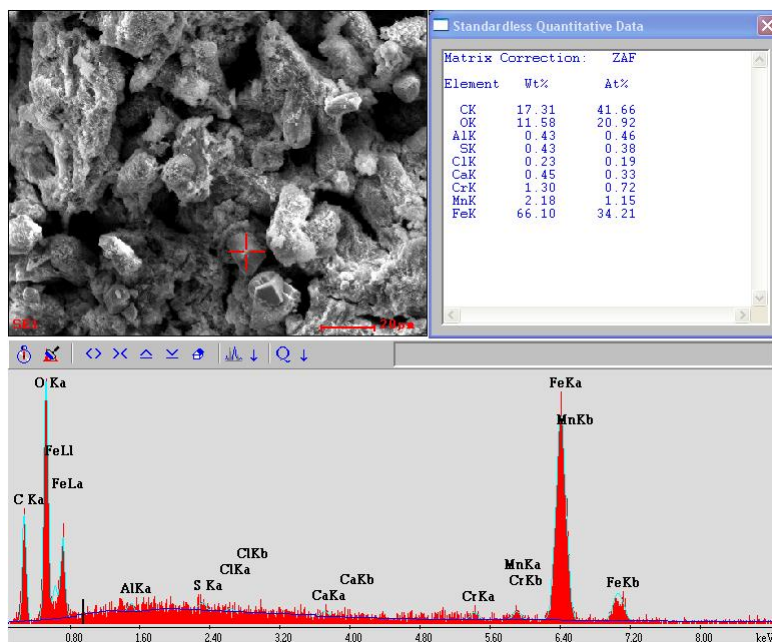


Figure 36: Composition of corrosion product layer by EDS at x1000 magnification and experiment condition of 70°C, 80 bar of CO₂ and 50ppm of K1.

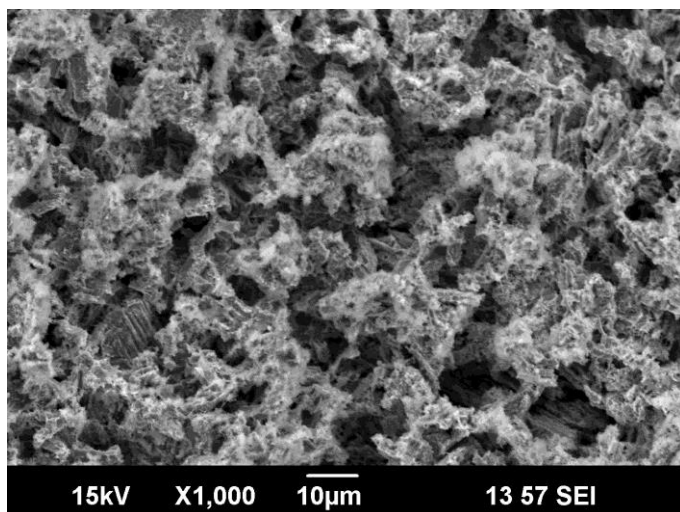


Figure 37: Surface of weight loss coupon at x1000 magnification after corrosion product was removed by Clarke solution and experiment condition of 70°C, 80 bar of CO₂ and 50ppm of K1.

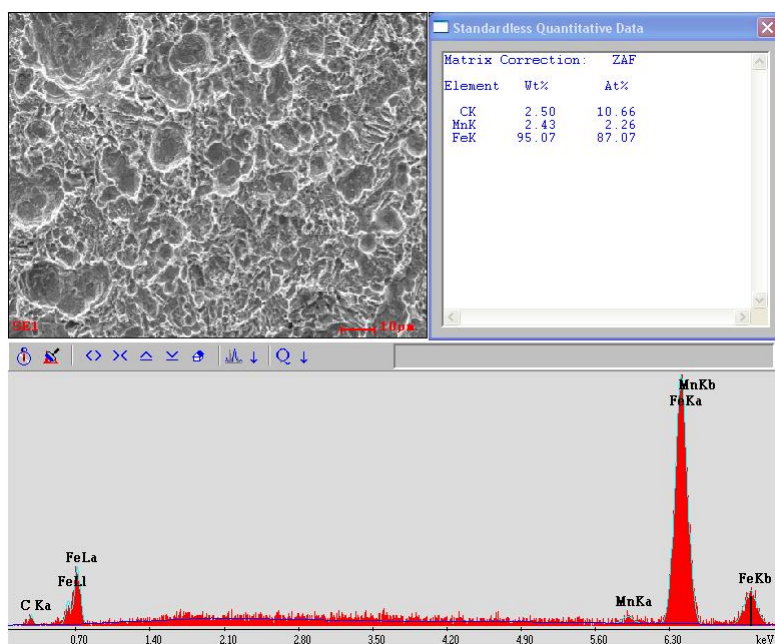


Figure 38: Composition of bare surface by EDS at x1000 magnification after corrosion product was removed by Clarke solution for experiment condition of 70°C, 80 bar of CO₂ and 50ppm of K1.

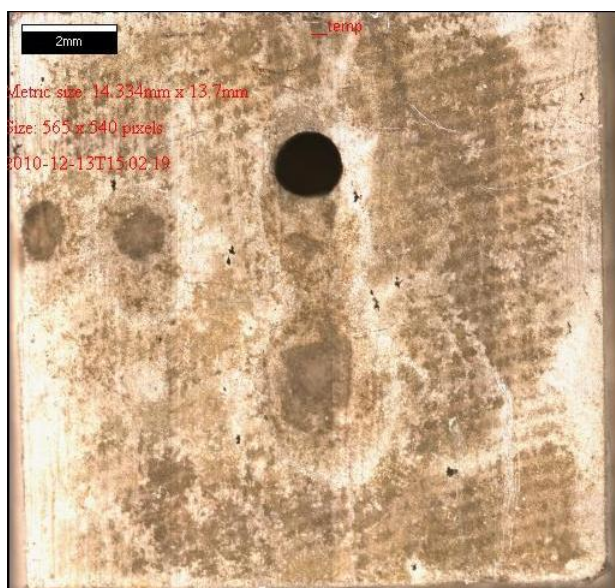


Figure 39: Surface image for experiment condition of 70°C, 80 bar of CO₂ and 50ppm of K1 and after immersion in Clarke solution.

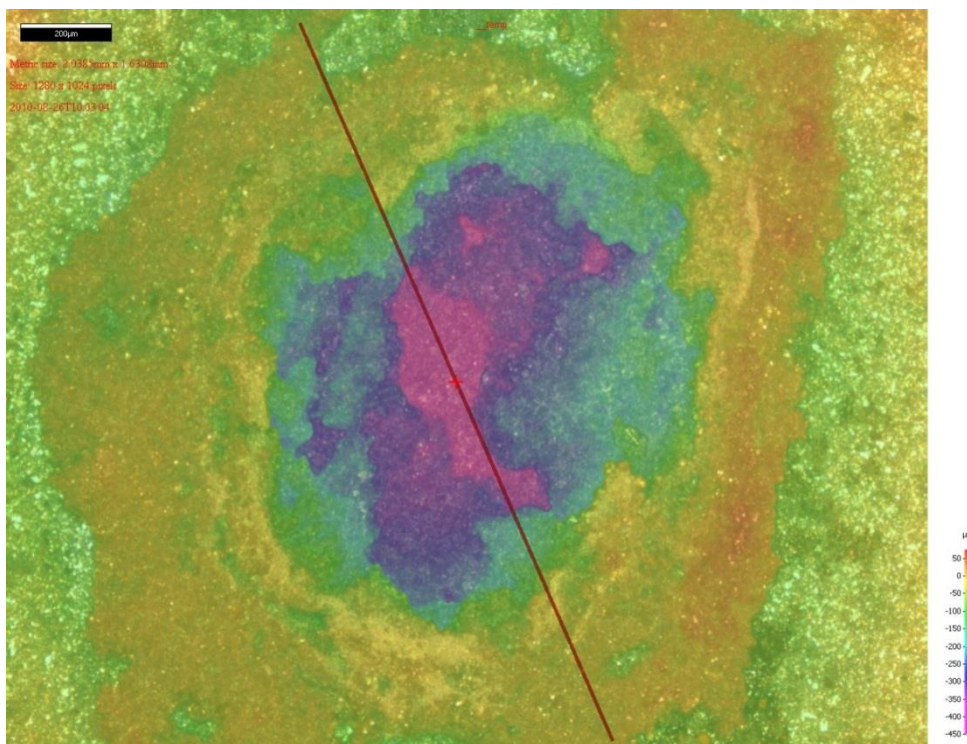


Figure 40: Depth profile of pitting on the steel surface after corrosion product was removed using Clarke solution.

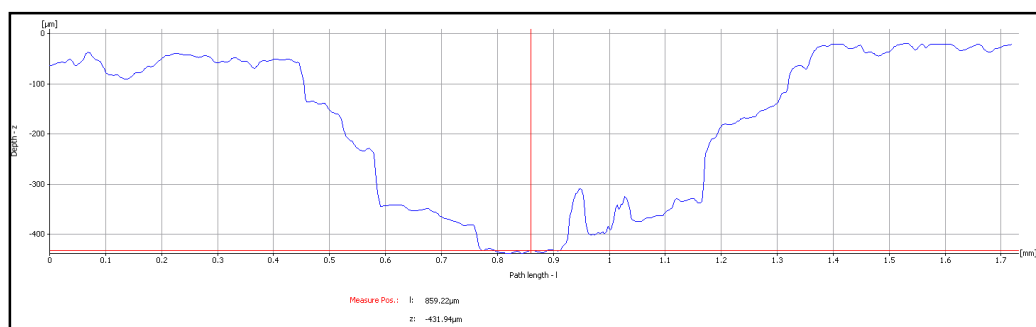


Figure 41 : Corrosion Inhibitor K1; Cross-section of pitting using infinite focus microscopy after corrosion product layer was removed using Clarke solution.

The surface morphologies for 50ppm K1 inhibited surface specimens are shown in Figure 35 to Figure 41. These images show that some areas were attacked by corrosion

and some areas protected by corrosion inhibitor. Figure 36 shows the elements on the metal surface by EDS analysis. Iron, carbon and alloying elements in specimens, such as chromium and manganese, were detected in the corrosion product. Figure 37 to Figure 41 show the surface morphology after corrosion product was removed using Clarke solution. Grooving and pitting attack were visible on the specimens, even by the naked eye. Data for elemental composition on the metal surface obtained by EDS analysis are shown in Figure 37 and Figure 38. Figure 39 shows severe pitting on the metal surface. Further analysis by IFM was conducted to measure the depth profile of pitting and to calculate penetration rate. The depth profile and cross-section of pitting are shown in Figure 40 and Figure 41.

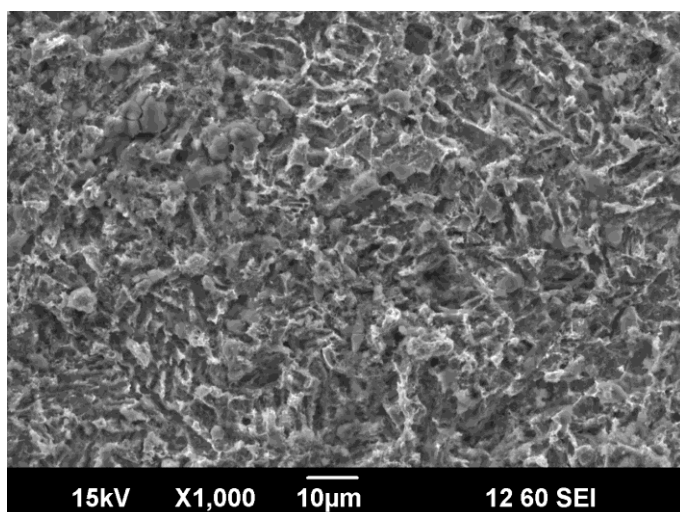


Figure 42: Surface of weight loss coupon at x1000 magnification and experiment condition of 70°C, 80 bar of CO₂ and 100ppm of K1.

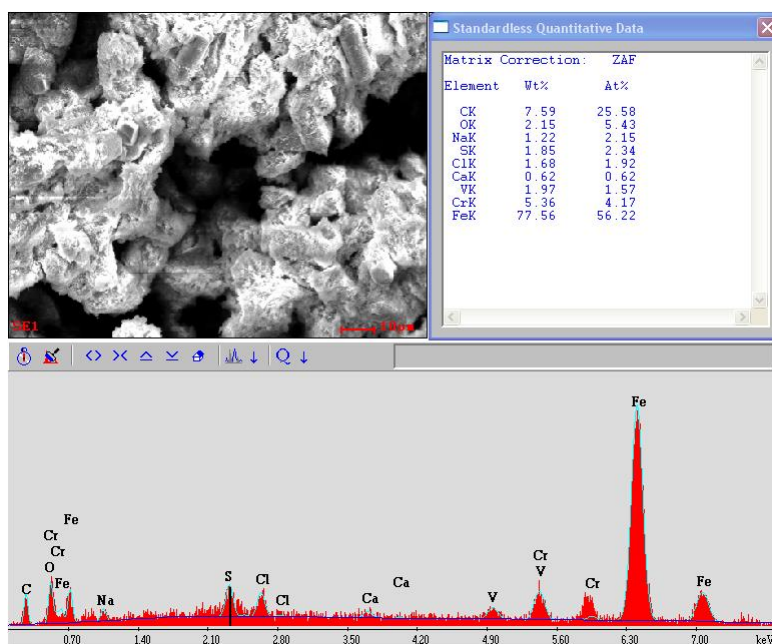


Figure 43 : Composition of corrosion product layer by EDS at x1000 magnification and experiment condition of 70°C, 80 bar of CO₂ and 100ppm of K1.

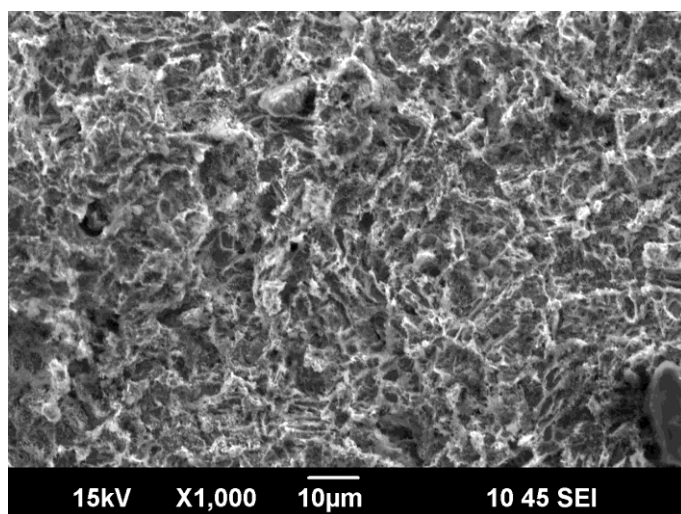


Figure 44: Surface of weight loss coupon at x1000 magnification after corrosion product layer was removed by Clarke solution and experiment condition of 70°C, 80 bar of CO₂ and 100ppm of K1.

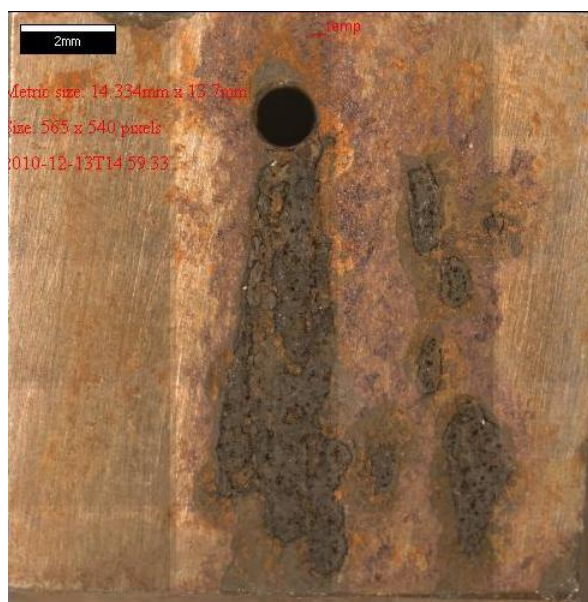


Figure 45: Surface image for experiment condition of 70°C, 80 bar of CO₂ and 100ppm of K1 after immersion in Clarke solution.

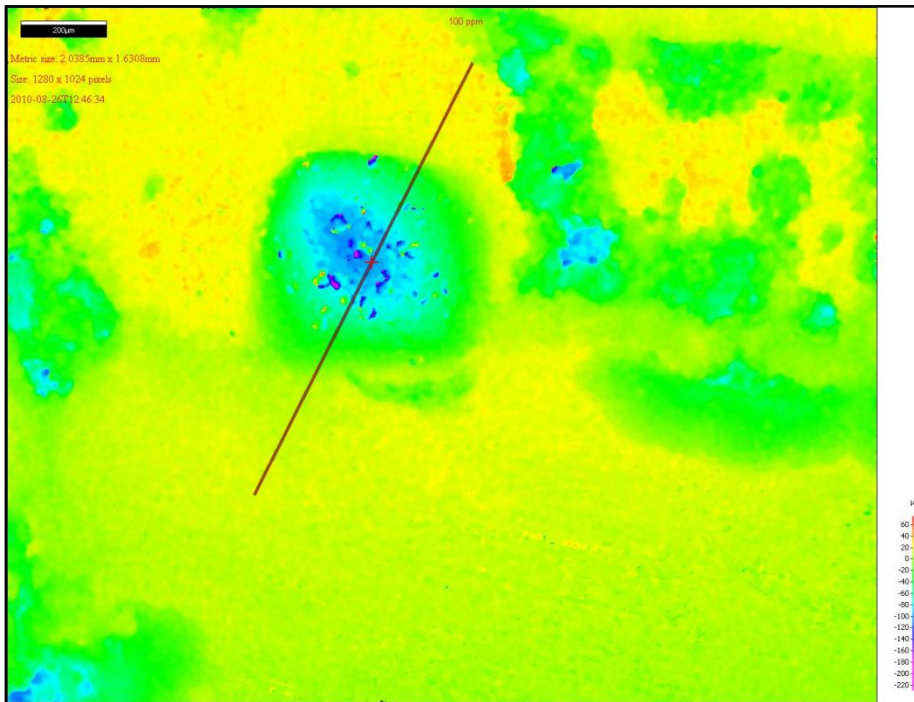


Figure 46: Depth profile of pitting on the steel surface after corrosion product layer was removed using Clarke solution.

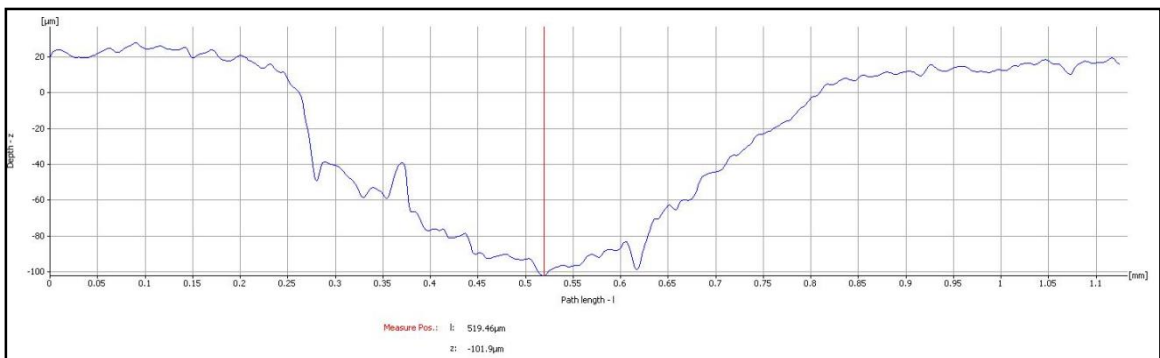


Figure 47: Cross-section of pitting using infinite focus microscopy after film was removed using Clarke solution.

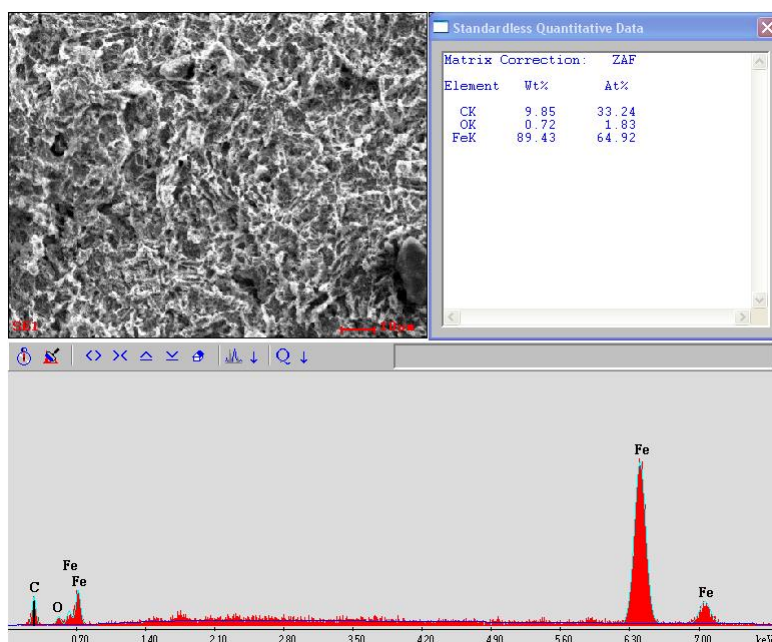


Figure 48: Composition of bare surface by EDS at x1000 magnification after corrosion product was removed by Clarke solution and experiment condition of 70°C, 80 bar of CO₂ and 100ppm of K1.

Surface morphologies of inhibited surface specimens at 100ppm K1 are shown in Figure 42 to Figure 48. Again, the metal surface is not fully protected by the corrosion inhibitor. Figure 43 shows the results of EDS elemental analysis of corrosion products, with a significant concentration of carbon detected but only a limited concentration of oxygen. The results suggest that the corrosion product on the surface mainly correspond to iron carbide mixed with some traces of X65 alloying elements such as chromium and vanadium; given the low oxygen concentration a small amount of iron carbonate, or some oxide, could be present. The sulfur detected from the EDS data would likely be the result of external contamination. No thiosulfate or any other sulfur-containing species were added in the K1 experimental system. Surface morphologies after corrosion product

removal by Clarke solution are shown in Figure 44 to Figure 48. Pitting and localized corrosion was observed on the metal surface and is shown clearly in Figure 45. Further testing by IFM profilometry was done to measure the depth profile and pitting rate. The depth profile and cross-section of the pitting are shown in Figure 46 and Figure 47. Figure 48 shows the result from EDS analysis after immersion in Clarke solution and the metal surface was free from any corrosion product.

Surface morphologies of inhibited surface specimens at 400ppm of corrosion inhibitor K1 are shown in Figure 49 to Figure 53. Figure 49 and Figure 50 show the surface morphology and composition of the specimen after severe corrosion in the high pressure CO₂ environment.

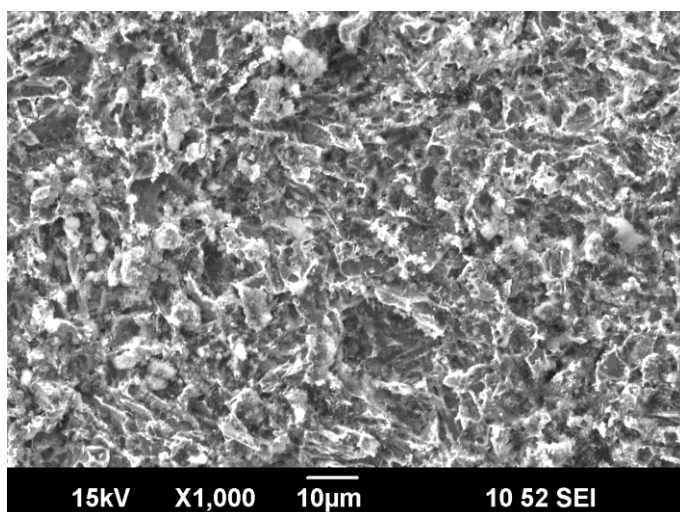


Figure 49: Surface of weight loss coupon at x1000 magnification and experiment condition of 70°C, 80 bar of CO₂ and 400ppm of K1.

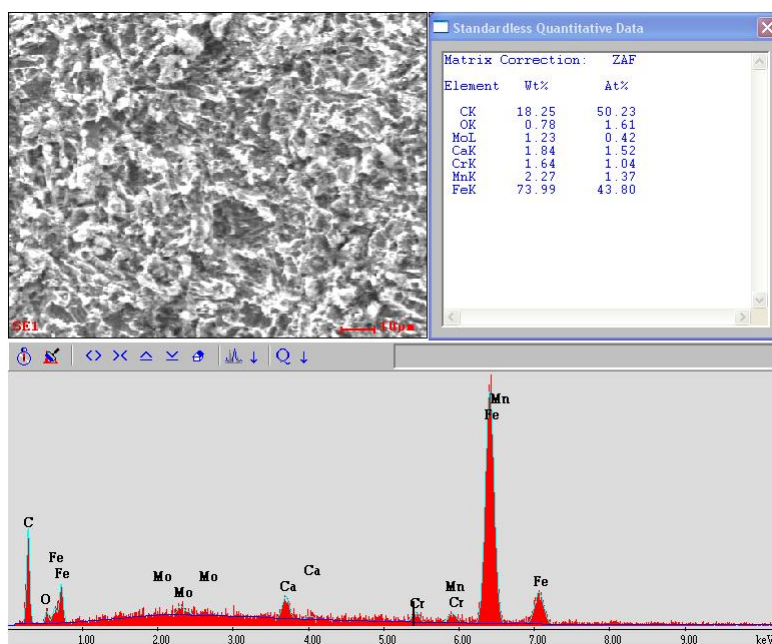


Figure 50: Composition of corrosion product layer by EDS at x1000 magnification and experiment condition of 70°C, 80 bar of CO₂ and 400ppm of K1.

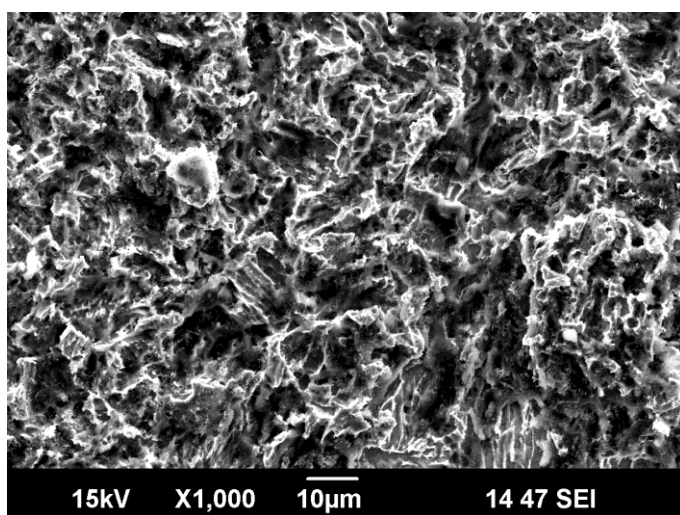


Figure 51: Surface of weight loss coupon at x1000 magnification after film was removed by Clarke solution for experiment condition of 70°C, 80 bar of CO₂ and 400ppm of K1.

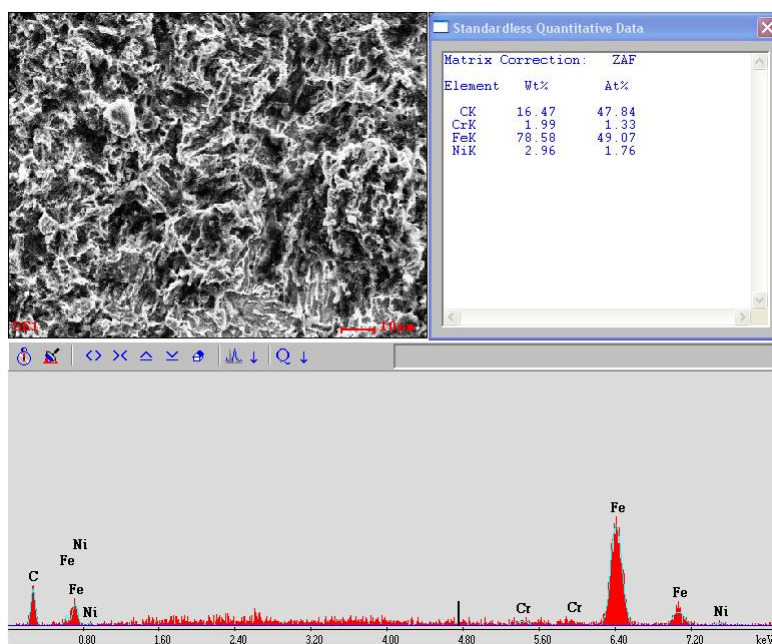


Figure 52 : Composition of bare surface by EDS at x1000 magnification after corrosion product was removed by Clarke solution for experiment condition of 70°C, 80 bar of CO₂ and 400ppm of K1.

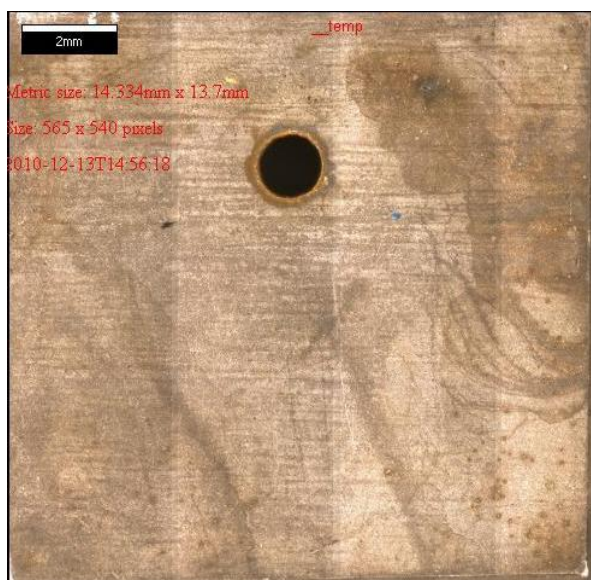


Figure 53: Surface image for experiment condition of 70°C, 80 bar of CO₂ and 400ppm of K1 and after immersion in Clarke solution.

Again, the EDS data was consistent with iron carbide being dominant on the steel surface, with only a trace of oxygen detected. EDS data also shows the alloying elements in X65 such as chromium, molybdenum and manganese. Figure 51 to Figure 53 show the surface after immersion in Clarke solution to remove the corrosion product on the surface of the specimen. These figures show no localized corrosion on the surface of the rectangular specimen. At this concentration of K1, the specimen is only attacked by general corrosion.

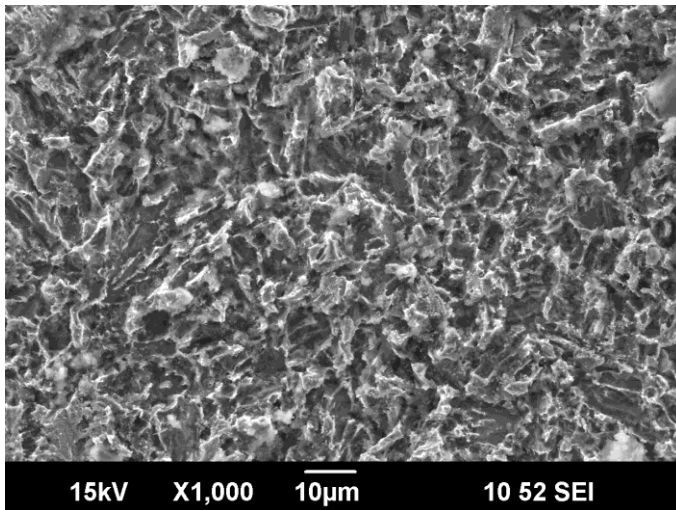


Figure 54: Surface of weight loss coupon at x1000 magnification and experiment condition of 70°C, 80 bar of CO₂ and 800ppm of K1.

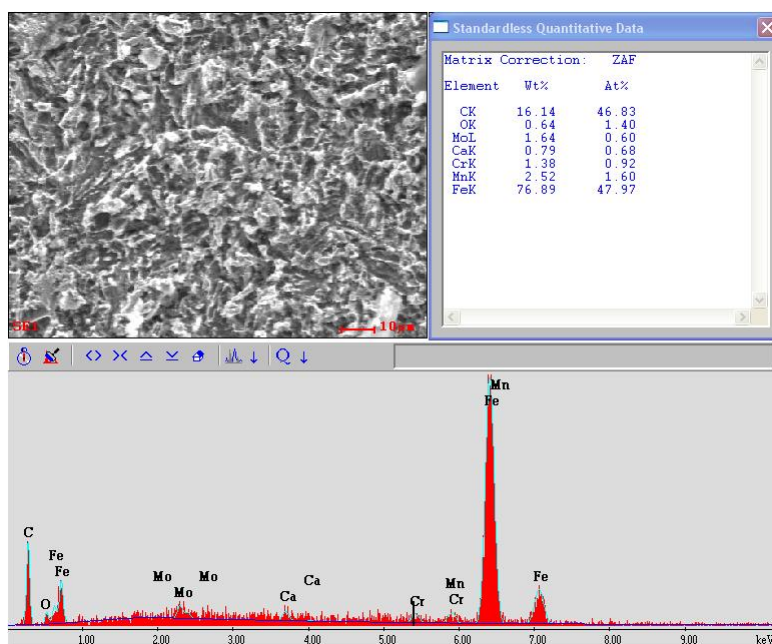


Figure 55: Composition of corrosion product layer by EDS at x1000 magnification and experiment condition of 70°C, 80 bar of CO₂ and 800ppm of K1.

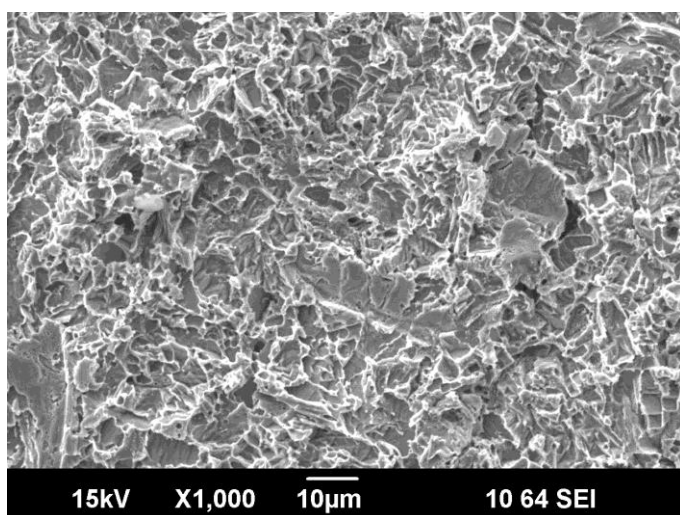


Figure 56: Surface of weight loss coupon at x1000 magnification after corrosion product was removed by Clarke solution for experiment condition of 70°C, 80 bar of CO₂ and 800ppm of K1.

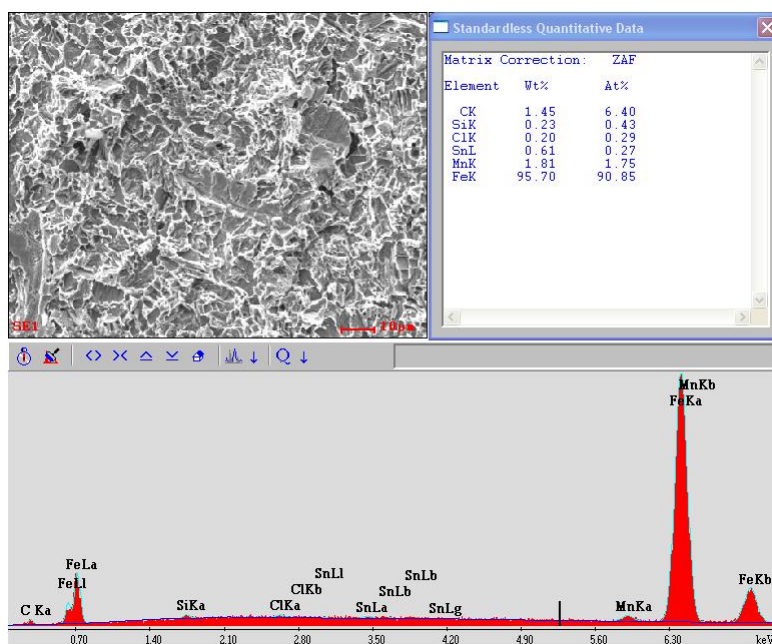


Figure 57: Composition of bare surface by EDS at x1000 magnification after corrosion product was removed by Clarke solution for experiment condition of 70°C, 80 bar of CO₂ and 800ppm of K1.

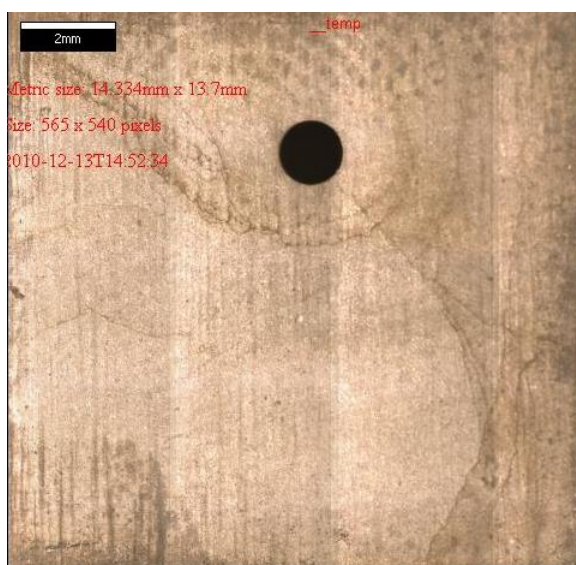


Figure 58: Surface image for experiment condition of 70°C, 80 bar of CO₂ and 800ppm of K1 and after immersion in Clarke solution.

Surface morphology of inhibited surface specimens at 800ppm of corrosion inhibitor K1 are shown in Figure 54 to Figure 58. Figure 54 and Figure 55 show the surface morphology and the composition of corrosion products after experiment completion. EDS data again indicates dominant iron and carbon, with only trace oxygen. Again, this is consistent with iron carbide. As observed previously, the alloying elements in X65 such as molybdenum, chromium and manganese are also found from EDS analysis. Figure 56 to Figure 58 show the surface after immersion in Clarke solution to remove the corrosion product from the surface of the specimens. Figure 58 shows no localized corrosion on the surface of the rectangular specimen. At this concentration of K1, the specimen was only attacked by general corrosion. Note that Figure 57 shows a trace of tin (Sn) from the Clarke solution treatment on the surface due to improper cleaning after film removal treatment.

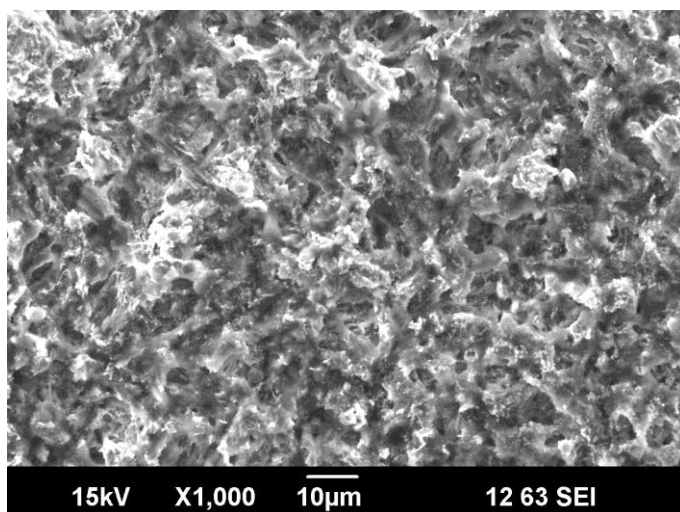


Figure 59: Surface of weight loss coupon at x1000 magnification and experiment condition of 70°C, 80 bar of CO₂ and 1500ppm of K1.

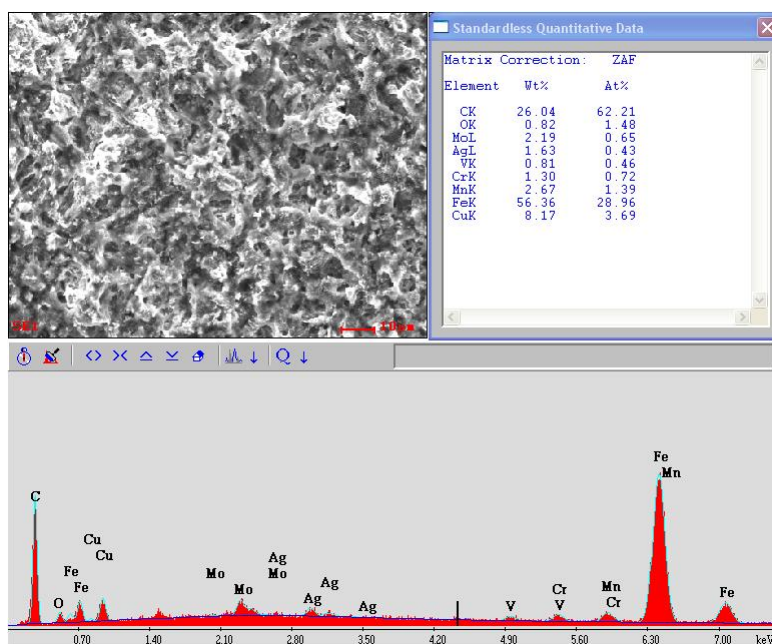


Figure 60: Composition of corrosion product layer by EDS at x1000 magnification and experiment condition of 70°C, 80 bar of CO₂ and 1500ppm of K1.

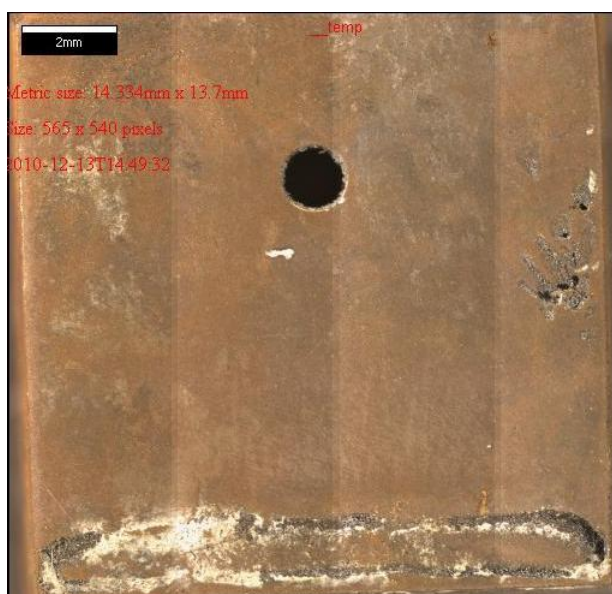


Figure 61: Surface image for experiment condition of 70°C, 80 bar of CO₂ and 1500ppm of K1 and after immersion in Clarke solution.

Surface morphology of inhibited surface specimens at 1500ppm of corrosion inhibitor K1 are shown in Figure 59 to Figure 61. Figure 59 and Figure 60 show the surface morphology and the nature of the corrosion products after experiment completion. Consistent with the previous data, EDS showed carbon and iron to be dominant on the X65 specimen, with a small concentration of oxygen and the alloying elements (Cr, Mo, Mn and V) from the steel. Figure 61 showed the surface after immersion in Clarke solution to remove the corrosion product from the surface. This shows no localized corrosion on the surface. At this concentration of K1, the specimen was only attacked by general corrosion. At this concentration of K1, 1500ppm is not economical to apply in the field.

Imidazoline-type corrosion inhibitor plus thiosulfate (K4)

Four different concentrations of K4 were tested at 70°C and 80 bar pressure of CO₂, corresponding to 50, 100, 200 and 400ppm. Figure 62 to Figure 64 show the results obtained by LPR, EIS and potentiodynamic sweep. Generally, the LPR result showed that K4 performed better than K1. The plots showed that the corrosion rates were lower and superior inhibitor persistence was observed with increased concentration of K4. Corrosion rate for the LPR test was calculated using equation 29 to equation 31. Polarization resistance from LPR readings was corrected with respect to solution resistance measured by EIS. Figure 62 shows that the desired corrosion rate can be reached at least at 200ppm of K4; at concentrations of 200ppm and 400ppm, this inhibitor gives a longer protection to the metal surface.

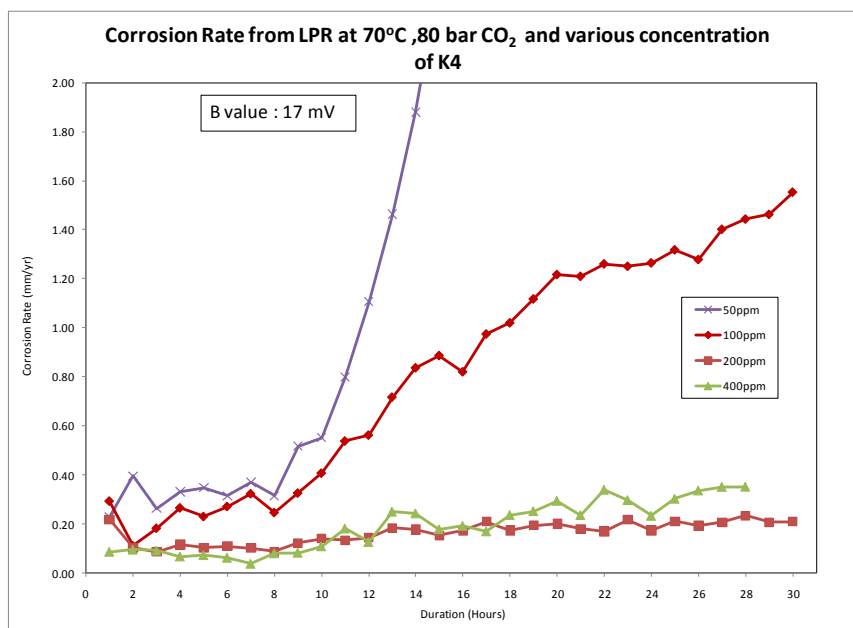


Figure 62: Corrosion rate with time by linear polarization resistance at 70°C, 80 bar of CO₂ and various concentrations of corrosion inhibitor formulation K4.

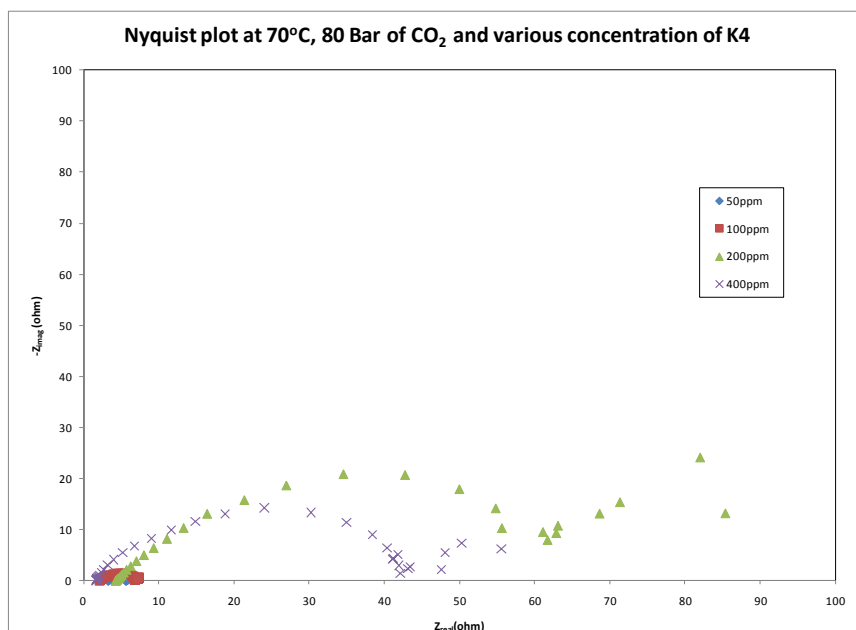


Figure 63: Solution resistance (R_s) and Polarization resistance (R_p) by electrochemical impedance spectroscopy at 70°C, 80 bar of CO₂ and various concentrations of corrosion inhibitor formulation K4.

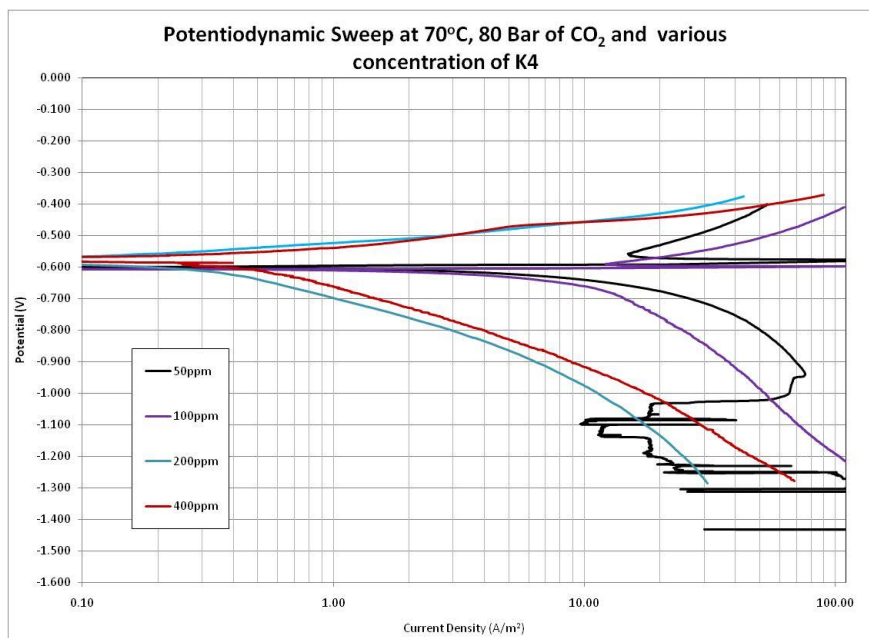


Figure 64: Potentiodynamic sweeps at 70°C, 80 bar pressure of CO₂ and various concentration of corrosion inhibitor K4.

EIS results showed the polarization resistance of corrosion inhibitor K4 and solution resistance. The addition of concentrations of corrosion inhibitor increases the diameter of semicircles of the Nyquist plots as shown in Figure 63. Figure 64 shows that the electrochemical reaction was controlled by charge transfer between iron and reducible species such as H₂CO₃ and H⁺. The increasing of corrosion inhibitor concentration moved the cathodic and anodic polarization curve to the lower corrosion current density, as shown in Figure 64.

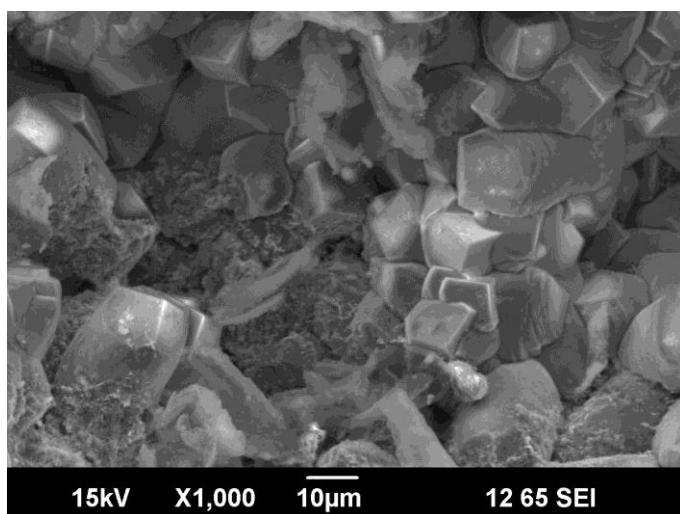


Figure 65: Surface of weight loss coupon at x1000 magnification and experiment condition of 70°C, 80 bar of CO₂ and 50ppm of K4.

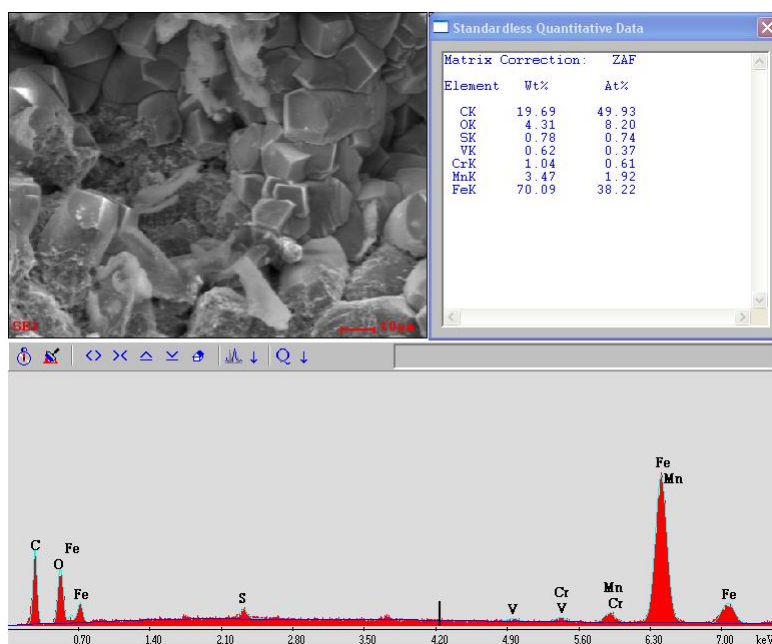


Figure 66: Composition of corrosion product layer by EDS at x1000 magnification and experiment condition of 70°C, 80 of CO₂ and 50ppm of K4.

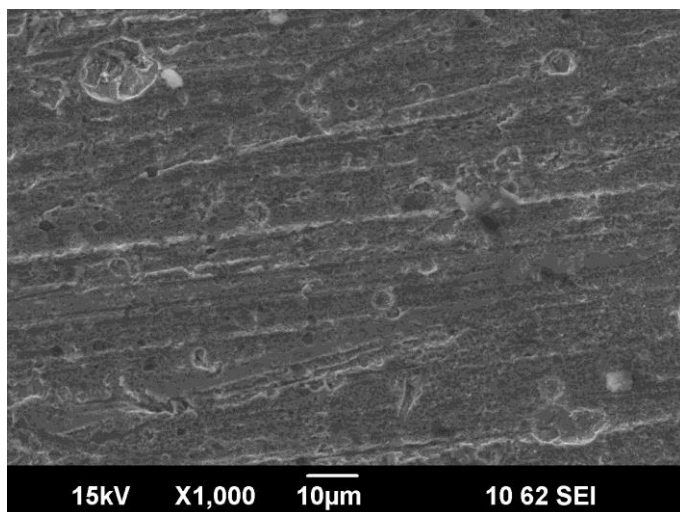


Figure 67: Surface of weight loss coupon at x1000 magnification after corrosion product was removed by Clarke solution for experiment condition of 70°C, 80 bar of CO₂ and 50ppm of K4.

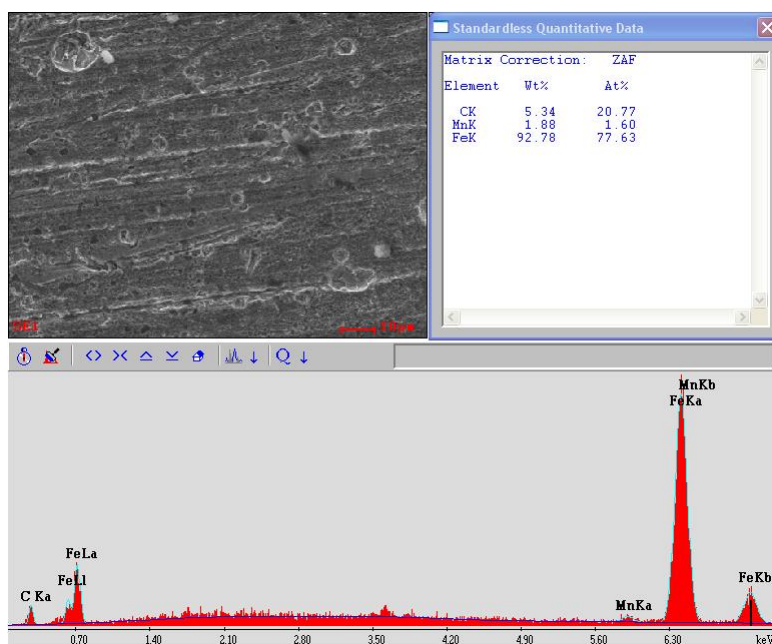


Figure 68: Composition of bare surface by EDS at x1000 magnification after corrosion product layer was removed by Clarke solution for experiment condition of 70°C, 80 bar of CO₂ and 50ppm of K4.

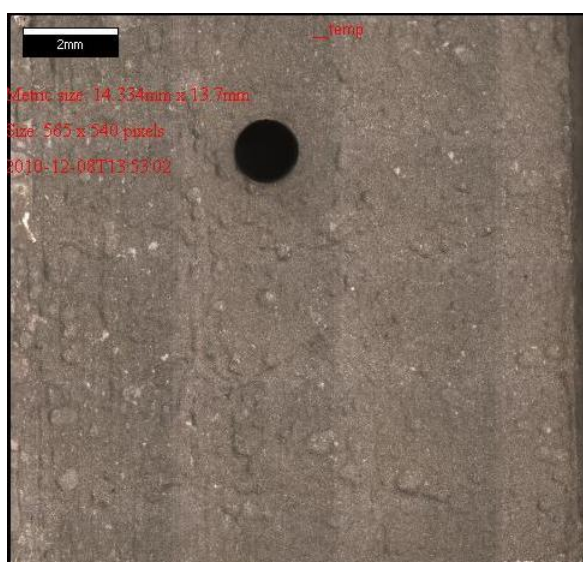


Figure 69: Surface image for experiment condition of 70°C, 80 bar CO₂ and 50ppm of K4 and after immersion in Clarke solution.

Surface morphology of 50 ppm inhibited surface specimens is shown in Figure 65 and Figure 66. The SEM and EDS analysis were performed immediately after sample removal from the autoclave. The images show some areas attacked by corrosion and some protected by corrosion inhibitor at 50ppm of K4. Note the presence of a crystal morphology consistent with FeCO_3 formation. Figure 66 shows the elements on the metal surface by EDS analysis with iron and carbon dominant, but with a relatively higher concentration of oxygen and a trace of sulfur. Considering the SEM, this composition could be consistent with iron carbide located beneath, and adjacent to, iron carbonate. Alloying elements in the X65 specimen, such as chromium and manganese, also were detected as the corrosion product by EDS analysis. The detected sulfur was likely present on the specimen surface as part of the protective layer derived from thiosulfate, one of the components in K4. Figure 67 to Figure 69 show the surface morphology after corrosion product was removed using Clarke solution. Iron, carbon and manganese were detected by EDS analysis, as shown in Figure 68. Figure 69 shows an image of a region of the rectangular coupon surface after the corrosion product layer was removed using Clarke solution. This shows only attack by general corrosion.

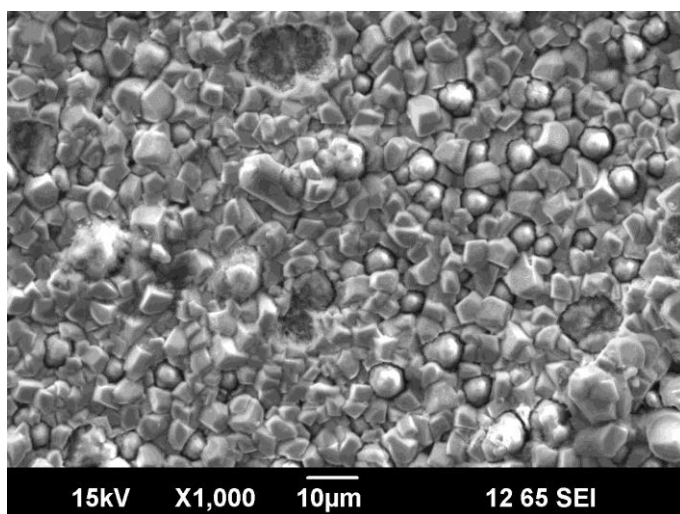


Figure 70: Surface of weight loss coupon at x1000 magnification and experiment condition at 70°C, 80 of CO₂ and 100ppm of K4.

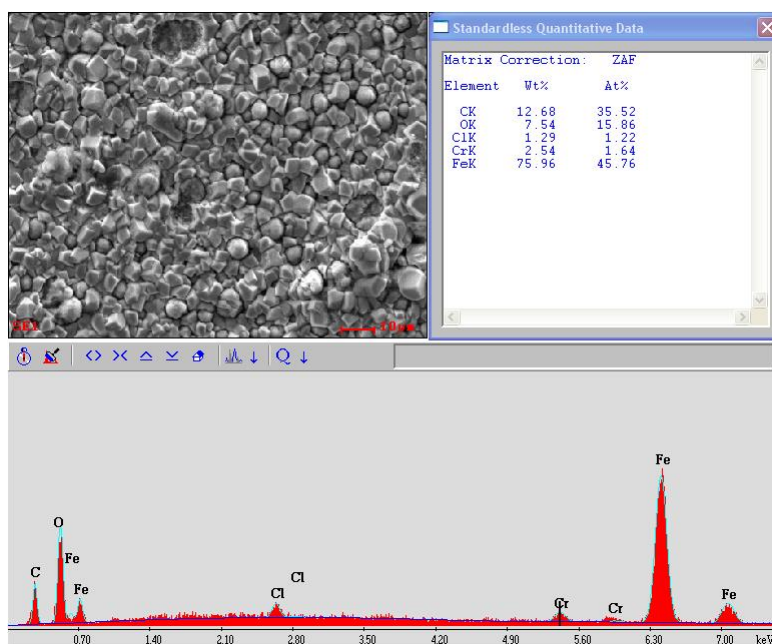


Figure 71: Composition of corrosion product layer by EDS at x1000 magnification and experiment condition of 70°C, 80 bar of CO₂ and 100ppm of K4.

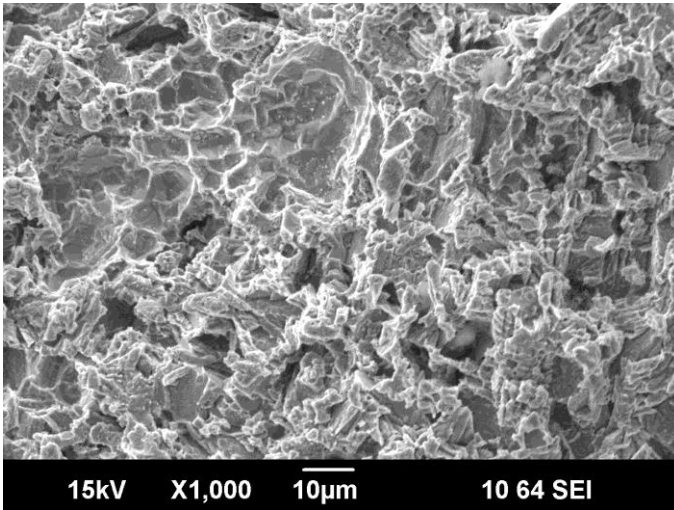


Figure 72: Surface of weight loss coupon at x1000 magnification after corrosion product was removed by Clarke solution and experiment condition of 70°C, 80 bar of CO₂ and 100ppm of K4.

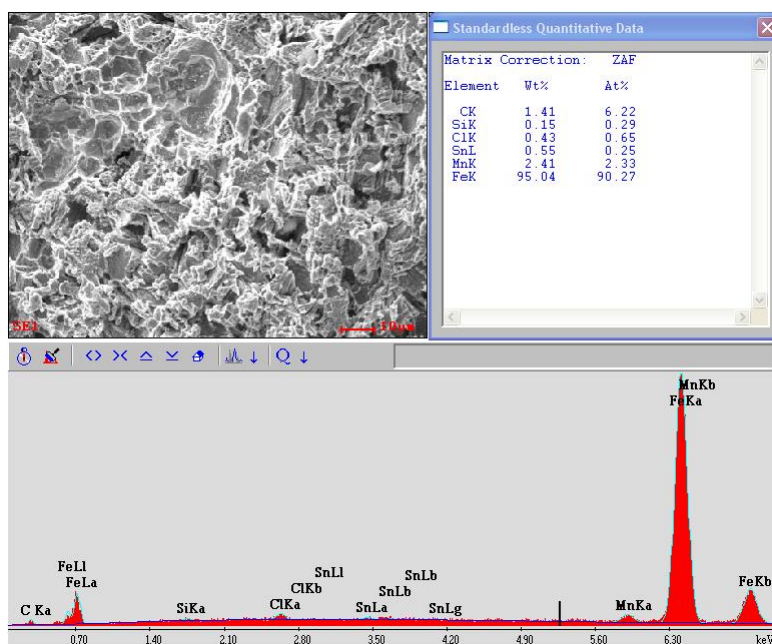


Figure 73: Composition of bare surface by EDS at x1000 magnification after corrosion product was removed by Clarke solution for experiment condition of 70°C, 80 bar of CO₂ and 100ppm of K4.

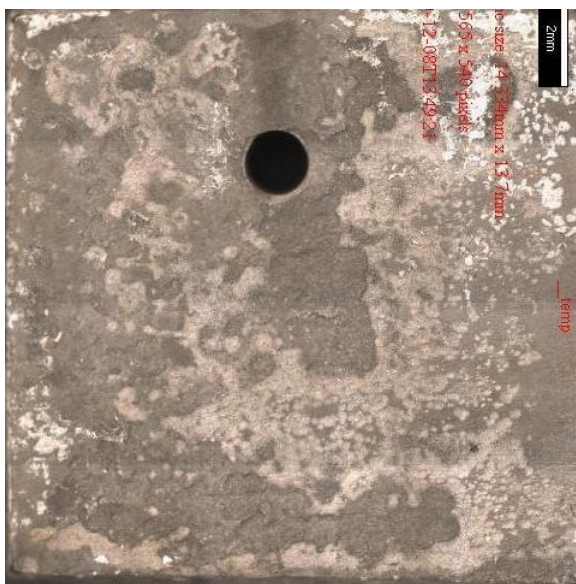


Figure 74: Surface image for experiment condition of 70°C, 80 bar of CO₂ and 100ppm of K4 and after immersion in Clarke solution.

Surface morphology of 100 ppm inhibited surface specimens is shown in Figure 70 to Figure 74. These images show some areas have undergone attack by corrosion and other areas were protected by corrosion inhibitor at 100ppm of K4. EDS shows iron, carbon and oxygen with the alloying element chromium, Figure 71. Figure 72 and Figure 74 show the surface morphology after corrosion product removal using Clarke solution. Elemental composition is shown in Figure 73, with an observed surface enrichment with respect to iron carbide being consistent with the data. This figure also shows a trace of tin from the Clarke solution on the surface of specimen. Figure 74 shows the surface of the specimen is free from localized attack and was only attacked by general corrosion.

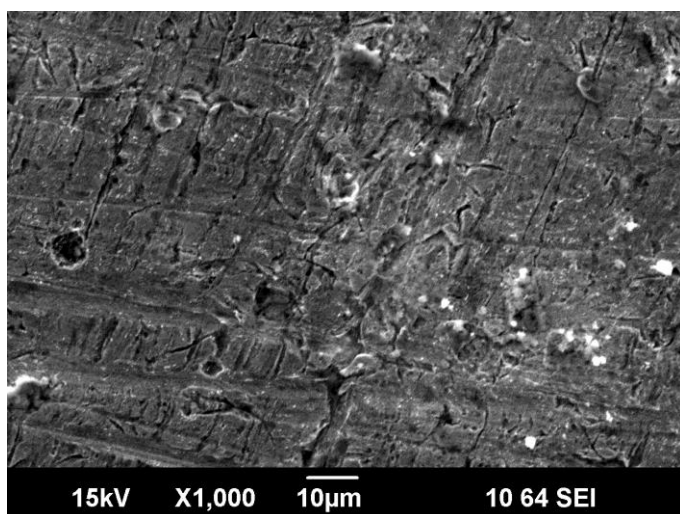


Figure 75: Surface of weight loss coupon at x1000 magnification and experiment condition of 70°C, 80 bar of CO₂ and 200ppm of K4.

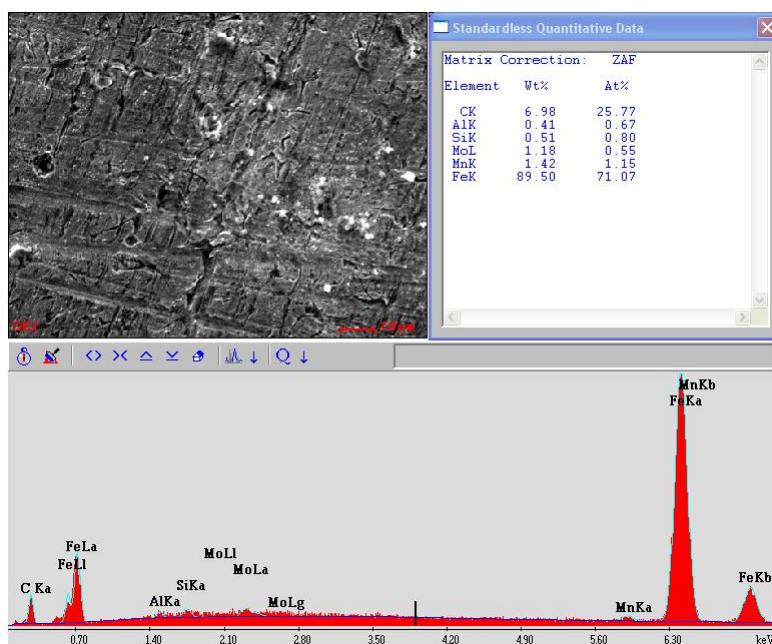


Figure 76: Composition of corrosion product layer by EDS at x1000 magnification and experiment condition of 70°C, 80 bar of CO₂ and 200ppm of K4.

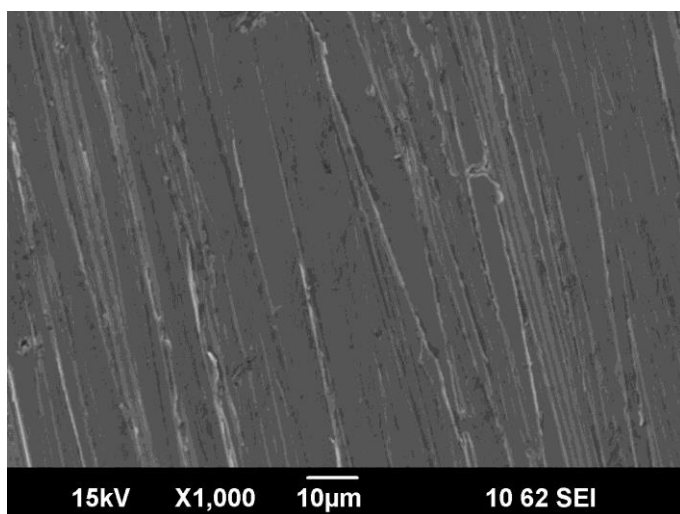


Figure 77: Surface of weight loss coupon at x1000 magnification after film was removed by Clarke solution for experiment condition of 70°C, 80 bar of CO₂ and 200ppm of K4.

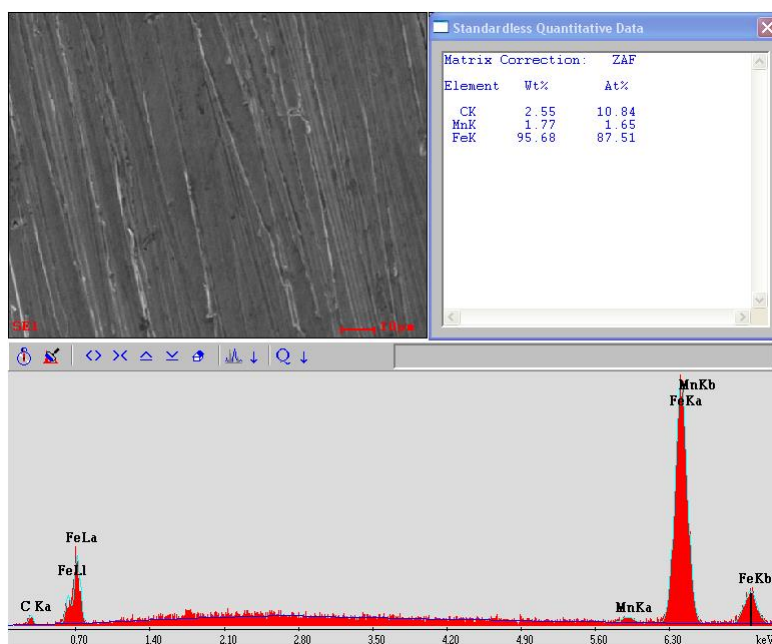


Figure 78: Composition of bare surface by EDS at x1000 magnification after corrosion product was removed by Clarke solution for experiment condition of 70°C, 80 bar of CO₂ and 200ppm of K4.

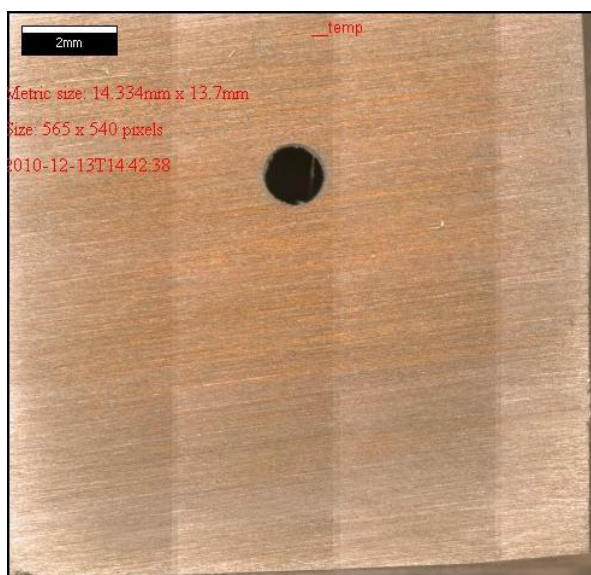


Figure 79: Surface image for experiment condition of 70°C, 80 bar of CO₂ and 200ppm of K4 and after immersion in Clarke solution.

Surface morphology of 200 ppm inhibited surface specimens are shown in Figure 75 to Figure 79. These images show the surface of specimens are less affected by corrosion attack due to the protection by corrosion inhibitor at 200ppm of K4. These results are also supported by electrochemistry measurement from LPR, potentiodynamic sweep and EIS, as shown in Figure 62, Figure 63 and Figure 64. Figure 76 shows that the composition at the metal surface is dominated by iron and carbon, with minor concentrations of alloying elements such as molybdenum and manganese; note the absence of oxygen. Figure 77 to Figure 79 show the specimen after corrosion product removal using Clarke solution. Figure 79 shows the polishing marks still appearing on the specimen surface, implying less attack by corrosive species. The metal was well protected by corrosion inhibitor at 200ppm of K4.

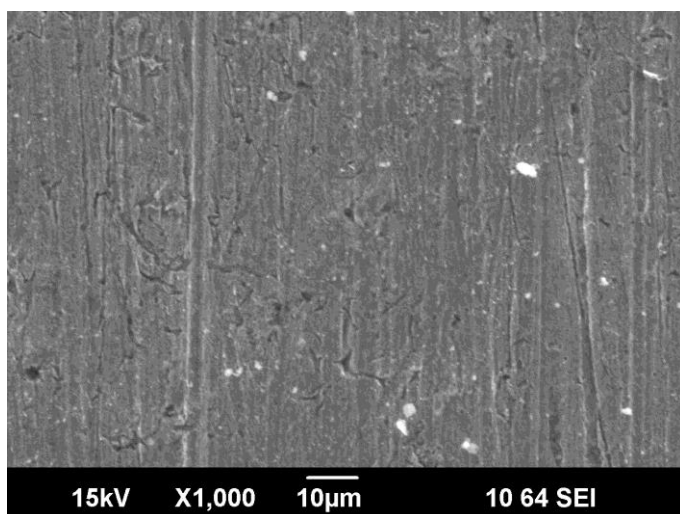


Figure 80: Surface of weight loss coupon at x1000 magnification and experiment condition of 70°C, 80 bar of CO₂ and 400ppm of K4.

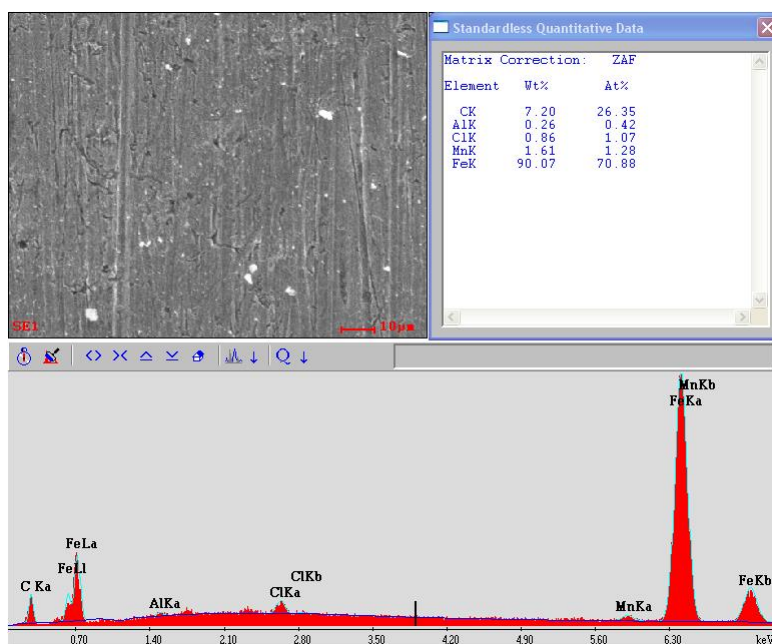


Figure 81: Composition of corrosion product layer by EDS at x1000 magnification for experiment condition of 70°C, 80 bar of CO₂ and 400ppm of K4.

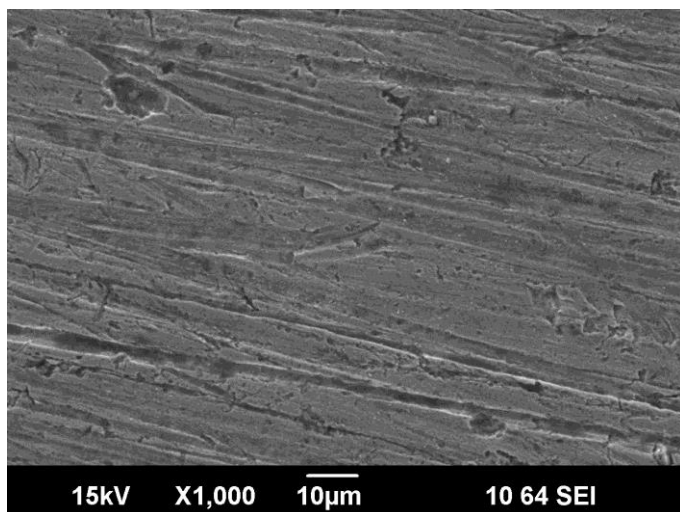


Figure 82: Surface of weight loss coupon at x1000 magnification after corrosion product was removed by Clarke solution and experiment condition at 70°C, 80 bar of CO₂ and 400ppm of K4.

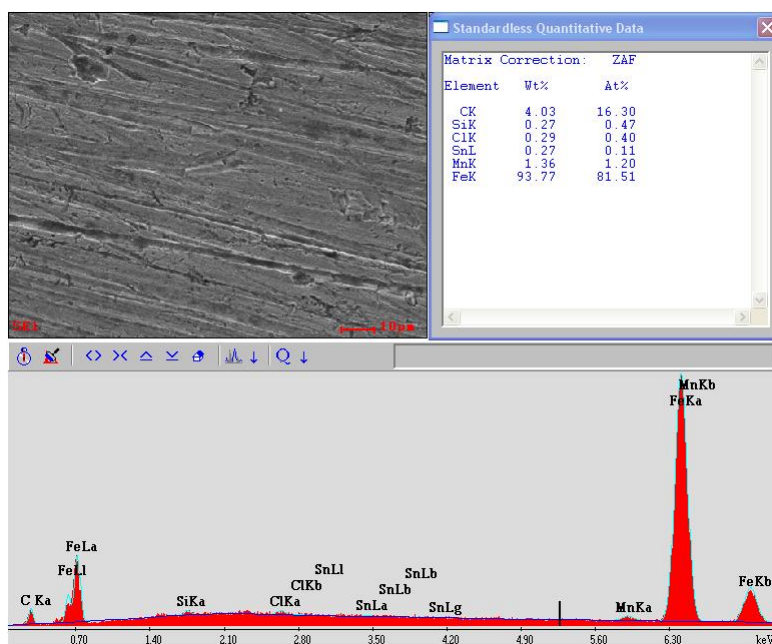


Figure 83: Composition of bare surface by EDS at x1000 magnification after corrosion product was removed by Clarke solution and experiment condition of 70°C, 80 bar of CO₂ and 400ppm of K4.

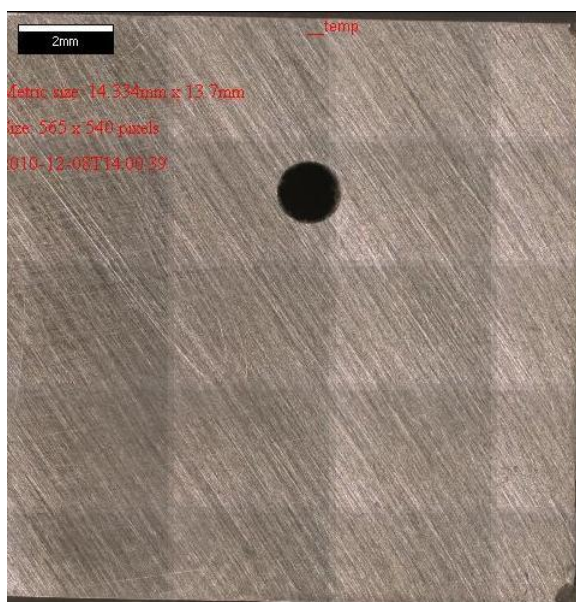


Figure 84: Surface image for experiment condition at 70°C, 80 bar of CO₂ and 400ppm of K4 and after immersion in Clarke solution.

Surface morphology of 400ppm inhibited surface specimens is shown in Figure 80 and Figure 84. These images show that the surfaces of specimens are even less affected by corrosion attack due to the high level of protection afforded by 400 ppm of corrosion inhibitor K4. These results are also supported by electrochemistry measurements by LPR, potentiodynamic sweeps and EIS, as shown in Figure 62, Figure 63 and Figure 64. Iron and carbon are again dominant on the metal surface of the X65, as shown in Figure 81. The alloying element manganese was also detected. Figure 82 to Figure 84 show the specimen surface after corrosion product was removed using Clarke solution. Again, a trace of tin was observed stemming from the Clarke solution treatment, as shown in Figure 83. The surface characteristics of specimens showed that the metal was well protected by corrosion inhibitor when injecting 400ppm of K4.

CHAPTER 7: CONCLUSIONS

The experimental set-up and measurement techniques used in this study were successful in accurately determining the mutual solubility of CO₂-H₂O systems at high pressures. Experimental data obtained in the solubility study agree with model predictions. pH measurements using the high pressure, high temperature pH probe tend to overestimate simulated data. The model prediction falls beyond the range of accuracy of the pH probe (± 0.2 pH units). The error from pH measurement may be due to resistance effects relating to the glass surface, improvements may be made by using a 1 wt. % NaCl electrolyte instead of deionized water.

Localized corrosion was observed at 50ppm and 100ppm for imidazoline-type inhibitor K1 and the penetration rate was 146 mm/yr and 43.8 mm/yr, respectively. No pitting was observed at 400 and 800ppm of K1. General corrosion rates can be reduced to 1 mm/yr by adding 50ppm of K1 and are further reduced to 0.45mm/yr by adding 100ppm. No specific trending was observed by potentiodynamic sweep, EIS and LPR.

K4, which is K1 with the addition of thiosulfate, has the capability to further reduce corrosion rate compared with K1. Specific trending was observed in LPR over time. No localized corrosion was observed on the surface of specimens even at 50ppm of K4. It is concluded that K4 can reduce general corrosion rate below 0.2mm/yr by adding 400ppm into the system. Corrosion rate over time by LPR shows a film persistency of around 8 to 10 hours after injection of corrosion inhibitor.

CHAPTER 8: RECOMMENDATION FOR FURTHER STUDIES

Organic compounds such as imidazoline-type corrosion inhibitor (K1) have the potential to be highly soluble in supercritical CO₂ (104). The effect of an organic solvent on imidazoline-type of corrosion inhibitor was studied by Xiong in his dissertation, he showed a significant impact on its adsorption to the metal surface (85). The organic solvent shows a significant effect on inhibitor removal compared to flow (85). On the other hand, K4 contained about 6.28% of thiosulfate, as shown in Figure 2, which shows superior suppression of the corrosion rate to below 0.2mm/yr. Thiosulfate ion is an inorganic-type corrosion inhibitor, which will resist becoming dissolved in supercritical CO₂. Further testing using thiosulfate only, without any imidazoline but in the presence of supercritical CO₂, should be performed to further shed the light on the observed inhibition. In addition, surface characterization using other techniques such as X-ray Photoelectron Spectroscopy (XPS) and Time of Flight Secondary Ion Mass Spectroscopy (ToFSIMS) are required to investigate further the mechanisms relating to thiosulfate's action at the metal surface.

REFERENCES

1. J. Gale, J. Davison. *Transmission of carbon dioxide—safety and economic considerations.*: Energy, 2004. Volume 29, pp 1319–1328.
2. D. Coleman, J. Davison, C. Hendriks, O. Kaarstad, M. Ozaki. *Transport of carbon dioxide.*: IPCC Special Report on Carbon dioxide Capture and Storage.
3. P.N. Seevam, M.J. Downie, J.M. Race. *The next generation carbon dioxide pipeline.* Calgary : 7th Int. Pipeline Conference, 2008.
4. J. Serpa, J. Morbee, E. Tzimas. *Technical and economic characteristics of a carbon dioxide transmission pipeline infrastructure.* The Netherlands : European Commission, 2011.
5. Y.S. Choi, S. Nesic, D. Young. *Effect of impurities on the corrosion behaviour of carbon dioxide transmission pipeline steel in supercritical carbon dioxide-water environments.*: Environmental Science & Technology, 2010. Volume 44, pp 9233-9238.
6. A. Oosterkamp, J. Ramsen. *State-of-the-art overview of carbon dioxide pipeline transport with relevance to offshore pipelines.*: Polytec, 2008.
7. D.P. Connell. *Carbon dioxide capture options for large point sources in the Midwestern United States: An assessment of candidate technologies.* South Park, PA : Consol Energy, 2005.
8. A. Dugstad, S. Clausen, B. Morland,. *Transport of dense phase carbon dioxide in C-steel pipelines – when is corrosion an issue?* New Jersey : Corrosion Conference, 2011. Paper 11070.
9. G. de-Koeijer. *Snøhvit LNG plant and carbon dioxide transport R&D.* Porsgrunn : Statoil, 2008.

10. Politec. *Draft report: Preparation for workshop 'Best practice pipeline transmission of carbon dioxide'*. Haugesund, Norway : s.n., 2008.
11. M. Nimtz, M. Klatt, B. Wiese, M. Kuhn , H.J. Krautz. *Modelling of the carbon dioxide process and transport chain in CCS systems—Examination of transport and storage processes.*: Geochemistry, 2010. Volume 70, pp 185-192.
12. F. Eldevik, B. Graver, L.E. Torbergsen, O.T. Saugerud. *Development of a guideline for safe, reliable and cost efficient transmission of carbon dioxide in pipelines.* : DNV, 2009. pp. 1579-1585.
13. P. Atkins, J. de Paula. *Elements of Physical Chemistry 4th Edition*. New York : Oxford University Press, 2007.
14. R. Doctor, A. Palmer, D. Coleman, J. Davison, C. Hendriks, O. Kaarstad, M. Ozaki, M. Austell, R. Pichs-Madruga, S. Timashev. *Transport of carbon dioxide.* : IPCC.
15. DNV: Practice, Recommended. *Design and Operation of carbon dioxide pipelines.* : DET NORSKE VERITAS, 2010. DNV-RP-J202.
16. M.F. Mohamed, A.M. Nor, M.F. Suhor, M. Singer, Y.S. Choi, S. Nestic. *Water chemistry for corrosion prediction in high pressure carbon dioxide environments.* : NACE Conference, 2011. 11375.
17. S. Nestic, M. Nordsveen, R. Nyborg, A. Stangeland. *A mechanistic model for carbon dioxide corrosion of mild steel in the presence of protective iron carbonate films—Part 1: theory and verification.* : Corrosion Journal, 2002. pp. Vol. 59, No. 5.
18. R. Nyborg. *Overview of carbon dioxide corrosion models for wells and pipelines.* : NACE Conference, 2002. 02233.

19. S. Paul, R. Shepherd, A. Bahrami, P. Woollin. *Material selection for supercritical carbon dioxide*. Gateshead, UK : TWI, 2010.
20. C. de Waard, D.E. Milliams. *Carbonic acid corrosion of steel*. : Corrosion Journal, 1975. Volume 31, pp 177-181.
21. —. *Prediction of carbonic acid corrosion in natural gas pipelines*. Bedford : BHRA Fluid Engineering, September 1975.
22. L.G.S. Gray, B.G. Anderson. *Mechanisms of carbon steel corrosion in brines containing dissolved carbon dioxide at pH 4*.: NACE Conference, 1989.
23. S. Netic, J. Postlethwaite, S. Olsen. *An electrochemical model for prediction of corrosion of mild steel in aqueous carbon dioxide solutions*.: Corrosion Journal, 1994.
24. S.Netic. *Key issues related to modeling of internal corrosion of oil and gas- A review*.: Corrosion Science, 2007. Volume 49, pp 4308–4338.
25. E.W. Klechka. *Use of corrosion inhibitors on the Trans Alaska Pipeline*. : Material Performance, January 2001. pp. 1-9.
26. J.W. Palmer. *Corrosion control by film forming inhibitors*. : NACE Conference, 2006. 06119.
27. S.D. Kapusta. *Corrosion inhibitor testing and selection for E&P: Auser's perspective*. : NACE Conference, 1999. 99016.
28. C. Canto. *Effect of wall shear stress on corrosion inhibitor film performance*. Athens : Ohio University, 2009.
29. X. Yao. *AFM investigation of corrosion inhibitors*. Athens : Ohio University, 2009.
30. O. Olivares-Xometl, N.V. Likhanova, M.A. Dominguez-Aguilar, J.M. Hallen, L.S. Zamudio, E. Arce. *Surface analysis of inhibitor films formed by imidazolines and amides*

on mild steel in an acidic environment. : Applied Surface Science, 2006. Volume 252, pp. 2139-2152..

31. S.M. Hesjevik, S. Olsen, M. Seiersten. *Corrosion at high carbon dioxide pressure.* : Corrosion Conference, 2003. 03345.

32. G. Schmitt, M. Kriek-Defrain. *pH static experiments in high pressure carbon dioxide corrosion of steel. Effect on scale morphology and chemical composition, corrosion rate, pitting susceptible and inhibitor performance.* : 11th International Corrosion Congress, 1990. Paper no. 480, pp 529,.

33. K.O. Kongshaugi, M. Seiersten. *Baseline experiments for the modelling of corrosion at high carbon dioxide pressure.*: NACE Conference, 2004. 04630.

34. M. Seiersten, S. M. Hesjevik, S. Olsen. *Corrosion at high carbon dioxide pressure.* . : NACE Conference, 2003. 03345.

35. L.G.S. Gray, B.G. Anderson. *Effect of pH and temperature on the mechanism of carbon steel corrosion by aqueous carbon dioxide.*: NACE Conference, 1990.

36. N. Spycher, K. Pruess, J. Ennis-King. *Carbon dioxide-water mixtures in the geological sequestration of carbon dioxide. 1. Assessment and calculation of mutual solubilities from 12 to 100 deg C and up to 600 bar.*: Geothermal Reservoir Engineering, 2003. Volume 67, pp 3015-3031.

37. R.V. Eldik, D.A. Palmer. *Effect of Pressure on the kinetics of the dehydration of carbonic acid and the hydrolysis of carbon dioxide in carbon dioxide aqueous solution.* : Journal of Solution Chemistry, 1982. Volume 11.

38. D. Li, Z. Duan. *The speciation equilibrium coupling with phase equilibrium in the water-carbon dioxide-sodium chloride system from 0 to 250 deg C, from 0 to 1000 bar, and from 0 to 5 molality of NaCl.* : Chemical Geology, 2007. Volume 244, pp 730-751.
39. Z. Duan, D. Li. *Coupled phase and aqueous species equilibrium of the water-carbon dioxide-sodium chloride-calcium carbonate systems from 0 to 250 deg C, 1 to 1000 bar with NaCl concentrations up to saturation of halite.* : Elsevier Geochimica et Cosmochimica Acta, 2008. Volume 72, pp 5128-5145.
40. J.T. Edsall. *Carbon dioxide, carbonic acid, and bicarbonate ion: physical properties and kinetics of interconversion.* Washington, D.C : National Aeronautics and Space Administration (NASA SP-188), 1969. pp. 15-34.
41. B. Meyssami, M.O. Balaban, A.A. Teixeira. *Prediction of pH in model systems pressurized with carbon dioxide.* : Biotechnology Progress, 1992. Volume 2, pp 149-154.
42. L.M. Raff. *Principles of physical chemistry.* New Jersey : Prentice Hall, 2001.
43. D.G. Skamenca, D.P. Tassios. *An Improved Redlich Kwong Equation of State in the supercritical region.* : Ind. Eng. Chem. Process Des. Dev, 1971. Volume 10, pp 59-64.
44. R. De Marco, W. Durnie, A. Jefferson, B. Kinsella. *Surface analysis of adsorbed carbon dioxide corrosion inhibitors.* : Corrosion Journal, 2001. Volume 57, Number 01.
45. M.J.J. Simon-Thomas. *Corrosion inhibitor selection - Feedback from the field.* : NACE Conference, 2000. 00056.
46. D.I. Horsup, J.C. Clark, B.P. Binks, P.D.I. Fletcher, J.T. Hicks. *The fate of oilfield corrosion inhibitors in multiphase systems.* : Corrosion Journal, 2010. Volume 66, Issue 3.

47. H.J. Chen, T. Hong, W.P. Jepson. *High temperature corrosion inhibition performance of imidazoline and amide.*: NACE Conference, 2000. 00035.
48. M.J. Rosen. *Surfactants and interfacial phenomena 3rd Edition.* : Wiley-Interscience, 2004.
49. R.H. Hausler, T.G. Martin, D.W. Stegmann, M.B. Ward. *Development of a corrosion inhibition model 1: Laboratory studies.*: NACE Conference, 1999. 99002.
50. V.S. Sastri. *Green corrosion inhibitor.* New Jersey : John Wiley and Sons, 2011.
51. NACE Resource Center. *NACE.* [Online] 12 28, 2011.
<http://events.nace.org/library/corrosion/Inhibitors/Processes.asp>.
52. L. Wang, M. Zhu, F.C. Yang, C.W. Gao. *Study of a triazole derivative as corrosion inhibitor for mild steel in phosphoric acid solution.*: International Journal of Corrosion, 2012. Volume 2012.
53. M.W. Kendig, R.D. Buchneit. *Corrosion inhibition of aluminum and aluminum alloys by solubles chromates, chromated coating, and chromates-free coating.* : Corrosion Journal, 2003. Vol 59, No. 5.
54. H.H. Hassan, E. Abdelghani, M.A. Amin. *Inhibition of mild steel corrosion in hydrochloric acid solution by triazole derivatives Part 1. Polarization and EIS studies.* : Electrochimica Acta., 2002. Volume 52, pp 6359-6366.
55. E. McCafferty. *Introduction to corrosion science.* London : Springer, 2010.
56. U. Ergun, D. Yuzer, K.C. Emregul. *The inhibitory effect of bis-2, 6-(3,5-dimethylpyrazolyl)pyridine on the corrosion behaviour of mild steel in HCl solution.* : Materials chemistry and physics, 2008. Volume 109, pp. 492-499.

57. E. Bayol, T. Gurten, A. Ali-Gurten, M. Erbil. *Interactions of some Schiff base compounds with mild steel surfaces in hydrochloric acid solution.* : Materials Chemistry and Physics, 2008. Volume 112, pp 624-630.
58. K. Aramaki, J. Uehara,. *Surface-enhanced raman spectroscopy study on adsorption of some sulfur-containing corrosion inhibitors on iron in hydrochloric acid solutions.* : J. Electrochem. Soc, 1991. Volume 138, pp 3245-3251.
59. S. E. Nataraja, T. V. Venkatesha, K. Manjunatha, B. Poojary, M. K. Pavithra, H. C. Tandon. *Inhibition of the corrosion of steel in hydrochloric acid solution by some organic molecules containing the methylthiophenyl moiety.* : Corrosion Science, 2011. Volume 53, pp. 2651-2659..
60. E. M. Gutman, L. N. Petrov. *Adsorption of corrosion inhibitors on mercury and steel.* : Fiziko-Khimicheskaya Mekhanika Materialov, 1966. Volume 3.
61. W. Li, Q. He, C. Pei , B. Hou. *Experimental and theoretical investigation of the adsorption behaviour of new triazole derivatives as inhibitors for mild steel corrosion in acid media.* : Electrochem. Acta, 2007. Volume 52, pp 6386–6394.
62. E.E. Oguzie. *Corrosion inhibition of mild steel in hydrochloric acid solution by methylene blue dye.*: Pigment & Resin Technology, 2005. Volume 38, pp 359-365.
63. R.I. Masel. *Principles of adsorption and reaction on solid surfaces.*: Wiley Interscience., 1996.
64. T.S.Y. Choong, T.G. Chuah, A. Idris , Y. L. Lai, S.Y. Quek. *A film-pore-surface concentration dependent model for adsorption of dye onto activated..* : Jurnal Teknologi, 2005. Volume 42, pp 47-66.

65. B.V. Babu, V. Ramakrishna. *Modeling of adsorption isotherm constant using regression analysis & neural networks*. : IIT-Bombay.
66. K.F. Khaled, S.S. Abdel-Rehim. *Electrochemical investigation of corrosion and corrosion inhibition of iron in hydrochloric acid solutions*. : Arabian Journal of Chemistry, 2010. Volume 4, pp 397-402.
67. W.H. Durnie, B.J. Kinsella, R. De Marco, A. Jefferson. *A study of the adsorption properties of commercial carbon dioxide corrosion inhibitor formulations*. : Journal of Applied Electrochemistry, 2001. Volume 31, pp 1221-1226.
68. E.O. Timmermann. *A BET-like three sorption stage isotherm*. : J. Chem. Soc., Faraday Trans. 1, 1989. Volume 85, pp 1631-1645.
69. U. Siripatrawan, P. Jantawat. *BET Model to determine moisture sorption isotherms of rice cereal*. : Food Sci Tech Int, 2006. Volume 12, pp 459-465.
70. Y.J. Tan, S. Bailey, B. Kinsella. *An investigation of the formation and destruction of corrosion inhibitor films using electrochemical impedance spectroscopy (EIS)*. : Corrosion Science, 1996. Volume 38, pp 1545-1561.
71. R. De Marco, W. Durnie, A. Jefferson, B. Kinsella, A. Crawford. *Persistence of carbon dioxide corrosion inhibitors*. : Corrosion Journal, 2002. Volume 58, pp 354-363.
72. R.B. Bird, W.E. Stewart, E.N. Lightfoot. *Transport phenomena second edition*. New York : John Wiley, 2002.
73. E. Gulbrandsen, A. Grana. *Testing of carbon dioxide corrosion inhibitor performance at high flow velocities in jet impingement geometry. Effects of mass transfer and flow forces*. : Corrosion Journal, 2007. Vol. 63, pp 1009-1020.

74. J.L Mora-Mendoza, J.G Chacon-Nava, G. Zavala-Olivares, M.A Gonzales - Nunez, S.Turgoose. *Influence of turbulent flow on the localized corrosion process of mild steel with inhibited aqueous carbon dioxide systems.* : Corrosion Journal, 2002. Volume 58, Number 07.
75. A. Gulcen. *Inhibitor effect of N,N'-methylenediacrylamide on corrosion behavior of mild steel in 0.5M HCl.* : Materials Chemistry & Physics, 2008. pp. 234-238. Volume 112, pp 234-238.
76. X. Zhang, F. Wang, Y. He, Y. Du. *Study of the inhibition mechanism of imidazoline amide on carbon dioxide corrosion of armco iron.* : Corrosion Science, 2001. Volume 43, pp 1417-1431.
77. A. Popova, E. Sokolova, S. Raicheva, M. Christov. *AC and DC study of the temperature effect on mild steel corrosion in acid media in the presence of benzimidazole derivatives.*: Corrosion Science, 2003. Volume 45, pp 33-58.
78. V. Jovancicevic, Y.S. Ahn, J. Dougherty, B. Alink,. *Carbon dioxide corrosion inhibition by sulfur-containing organic compounds.* : NACE Conference, 2000. 00007.
79. V. Jovancicevic, S. Ramachandran, P. Prince. *Inhibition of carbon dioxide corrosion of mild steel by imidazolines and their precursors.* : NACE Conference, 1998. 98018.
80. S. Ramachandran, V. Jovancicevic, P. Prince. *Inhibition of carbon dioxide of mild steel by imidazoline and their precursors.* : Corrosion Science, 1999. Volume 5, pp 449-455.
81. D.A. Lopez, S.N. Simison, S.R.de Sanchez. *Inhibitors performance in carbon dioxide corrosion EIS studies on the interaction between their molecular structure and steel microstructure.* : Electrochimica Acta, 2003. Volume 48, pp 845 – 854.

82. G. Zhang, C. Chen, M. Lu, C. Chai, Y. Wu. *Evaluation of inhibition efficiency of an imidazoline derivative in carbon dioxide-containing aqueous solution.* : Materials Chemistry & Physics, 2007. Volume 105, pp 331–340.
83. K. Oppenlaender, K. Stork, K. Barthold. *Imidazoline based corrosion inhibitors which inhibit corrosion caused by carbon dioxide and hydrogen sulfide.* : US Patent, 1983. US4388214 A.
84. N.J. Phillips, J.P. Renwick, J.W. Palmer, A.J. Swift. *The synergistic effect of sodium thiosulphate on corrosion inhibitors.* Geilo : Norske Sivilingeniørers Forening, 1996.
85. X. Yao. *AFM studies of the metallicity of single-walled carbon nanotubes and corrosion inhibitor adsorption.* Athens : Ohio University, 2011.
86. M.D. Lay, K. Varazo, J.L. Stickney. *Formation of sulfur atomic layers on gold from aqueous solutions of sulfide and thiosulfate: Studies using EC-STM, UHV-EC, and TLEC.* : Langmuir, 2003. Volume 19, pp 8416-8427..
87. P. Lowmunkhong, D. Ungtharak, P. Sutthivaiyakit. *Tryptamine as a corrosion inhibitor of mild steel in hydrochloric acid solution.* : Corrosion Science, 2010. Volume 52, pp 30-36.
88. M. Akhtar, A.L. Abdelhady, M.A. Hadi, P. O' Brien. *Deposition of iron sulfide thin films by AACVD from single source precursors.*: Journal of Crystal Growth, 2012. Volume 346, pp 106-112..
89. M. Kappes, G.S. Frankel, N. Srinidhar, R.M. Carranza. *Corrosion behaviour of carbon steel in acidified, thiosulfates-containing brines.* : Corrosion Journal, 2012. Volume 68, pp. 872-884.

90. G.S. Frankel, M. Kappes,, N. Srinidhar, R.M. Carranza. *Reaction paths of thiosulfate during corrosion of carbon steel in acidified brines.* : Journal of Electrochemical Society, 2012.
91. W. Sun. *Dissertation: Kinetics of iron carbonate and iron sulfide scale formation in carbon dioxide/hydrogen sulfide corrosion.* : Ohio University, 2006.
92. G. Rayner-Canham, T. Overton. *Descriptive Inorganic Chemistry, Third Edition.* New York : W.H. Freeman & Company, 2002.
93. D.Y. Peng, D.B. Robinson. *A new two-constant equation of state.* : Ind. Eng. Chem., 1976. Vol. 15, pp 59-64.
94. N. Spycher, K. Pruess, J. Ennis-King. *Carbon dioxide-water mixtures in the geological sequestration of carbon dioxide. I. Assessment and calculation of mutual solubilities from 100 deg C and up to 600 bar.* : Geochimica et Cosmochimica Acta, 2003. Volume 67, pp 3015-3031.
95. N. Spycher, K. Pruess. *Carbon dioxide-water mixtures in the geological sequestration of carbon dioxide. II. Partitioning in chloridebrines at 12–100 deg C and up to 600 bar.:* Geochimica et Cosmochimica Acta, 2005. Volume 69, pp 3309–3320.
96. S. Nesic, M. Nordsveen, R. Nyborg, A. Stangeland. *A mechanistic model for carbon dioxide corrosion with protective iron carbonate films.:* NACE Conference, 2001. 01040.
97. J.O'M Bockris, D. Drazic. *The electrode kinetics of the deposition and dissolution of iron.* : Electrochimica Acta, 1961. 325-326.
98. M. Yarrison, K.R. Cox, W.G. Chapman. *Measurement and modeling of the solubility in water in supercritical methane and ethane from 310 and 477 K and pressures from 3.4 to 110 MPa.* Houston, Texas : Rice University, 2006. pp. 6770-6777.

99. J. Gibson. *Moisture monitor series 35, single channel hygrometer-User's manual*.
Biierica : GE Infrastructure Sensing, 2004.
100. *Standard practice for laboratory immersion corrosion testing of metals.*: ASTM
International, 2004. ASTM G31.
101. *Standard practice for preparing, cleaning, and evaluating corrosion test specimens*.
: ASTM, 2003.
102. K.K. Chokshi. *Thesis: A study of inhibitor-scale interaction in carbon dioxide
corrosion of mild steel*. Athens : Ohio University, 2004.
103. G. Zhang, C. Chen, M. Lu, C. Chai, Y. Wu. *Evaluation of inhibition efficiency of an
imidazoline derivative in carbon dioxide-containing aqueous solution*. : Materials
Chemistry & Physics, 2007. Volume 105, pp 331-340.
104. J.A. Hyatt. *Liquid and supercritical carbon dioxide as organic solvents*. : J. Org.
Chem, 1984. Volume 50, pp 3246–3246.
105. G.Y. Elewady, I.A. El-Said, A.S. Fouda,. *Anion surfactants as corrosion inhibitors
for aluminum dissolution in HCl solutions*. : Int J Electrochem Science, 2008. Volume 3.
106. T.P. Zhao, G.N. Mu. *The adsorption and corrosion inhibition of anion surfactants
on aluminium surface in hydrochloric acid*. : Corrosion Science, 1999. Volume 41, pp
1937-1944.
107. W. Sun, S. Nesic. *Kinetics of iron sulfides and mix iron sulfides/carbonate scale
precipitation in carbon dioxide/hydrogen sulfide corrosion*.: NACE Conference, 2006.
06644.

APPENDIX A: NOMENCLATURE

Symbol	Name
ppm	Parts per million
G	Gibbs free energy, kJ/mol
G^0	Standard Gibbs free energy, kJ/mol
V	Volume, m^3
K_{sol}	Equilibrium constant for solubility of CO_2 in water, Molar/Bar
K_{hy}	Equilibrium constant for hydration of CO_2 , per second
K_{ca}	Equilibrium constant for dissociation of H_2CO_3 , $Kmol/m^3$
K_{bi}	Equilibrium constant for dissociation of HCO_3^- , $kmol/m^3$
K_{wa}	Equilibrium constant for dissociation of water, $kmol/m^3$
C_{CO_2}	Concentration of CO_2 in bulk solution, $kmol/m^3$
$C_{H_2CO_3}$	Concentration of H_2CO_3 in bulk solution, $kmol/m^3$
$C_{HCO_3^-}$	Concentration of HCO_3^- in bulk solution, $kmol/m^3$
$C_{CO_3^{2-}}$	Concentration of CO_3^{2-} in bulk solution, $kmol/m^3$
C_{H^+}	Concentration of H^+ in bulk solution, $kmol/m^3$
C_{OH^-}	Concentration of OH^- in bulk solution, $kmol/m^3$

P_{CO_2}	Partial pressure of CO ₂ in bar.
P_{H_2O}	Partial pressure of water in bar.
y_{H_2O}	Mole fraction of water in carbon dioxide gas phase
x_{CO_2}	Mole fraction of carbon dioxide in water
$K_{H_2O}^\circ$	Equilibrium constant for solubility of CO ₂ in water,
$K_{CO_2}^\circ$	Equilibrium constant for solubility of water in CO ₂
\bar{V}_{H_2O}	Average partial molar volume for water in cm ³ /mol
$\bar{V}_{CO_2}(\text{gas})$	Average partial molar volume for CO ₂ in gas form, cm ³ /mol
$\bar{V}_{CO_2}(\text{liq})$	Average partial molar volume for CO ₂ in liquid form, cm ³ /mol
R	Gas constant which is 83.1447 bar.cm ³ /mol.K
T	Temperature in Celsius or Kelvin.
ϕ_{CO_2}	Fugacity coefficient for CO ₂ . Dimensionless.
ϕ_{H_2O}	Fugacity coefficient for H ₂ O. Dimensionless.
a_{CO_2}	Attraction parameter for pure CO ₂ . Bar.cm ⁶ .K ^{0.5} .mol ⁻²
a_{H_2O}	Attraction parameter for pure H ₂ O.
$a_{H_2O-CO_2}$	Attraction parameter for binary CO ₂ - H ₂ O. Bar.cm ⁶ .K ^{0.5} .mol ⁻²
b_{CO_2}	Repulsion parameter for CO ₂ .cm ³ /mol
b_{H_2O}	Repulsion parameter for H ₂ O.cm ³ /mol

$\rho_{\text{H}_2\text{O}}$	Density of water, g/cm^3 .
-----------------------------	-------------------------------------

APPENDIX B: SUPPORTING FIGURES

Figure 85 to Figure 88 show additional SEM and EDS results for the surfaces of corrosion coupons for the testing at 70°C and 80 bar of CO₂ in the absence of corrosion inhibitor. Surface analyses in the presence of corrosion inhibitor K1 (imidazoline-type corrosion inhibitor) are shown in Figure 89 to Figure 106. Figure 107 to Figure 122 show results from the surface analysis for experiments conducted in the presence of corrosion inhibitor K4 (imidazoline-type corrosion inhibitor plus thiosulfate).

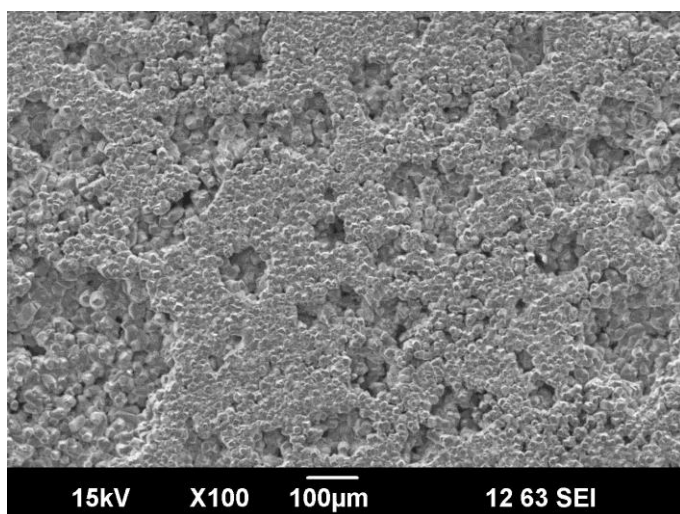


Figure 85: Surface of weight loss coupon at x100 magnification for experiment condition of 70°C and 80 bar of CO₂ in absence of corrosion inhibitor.

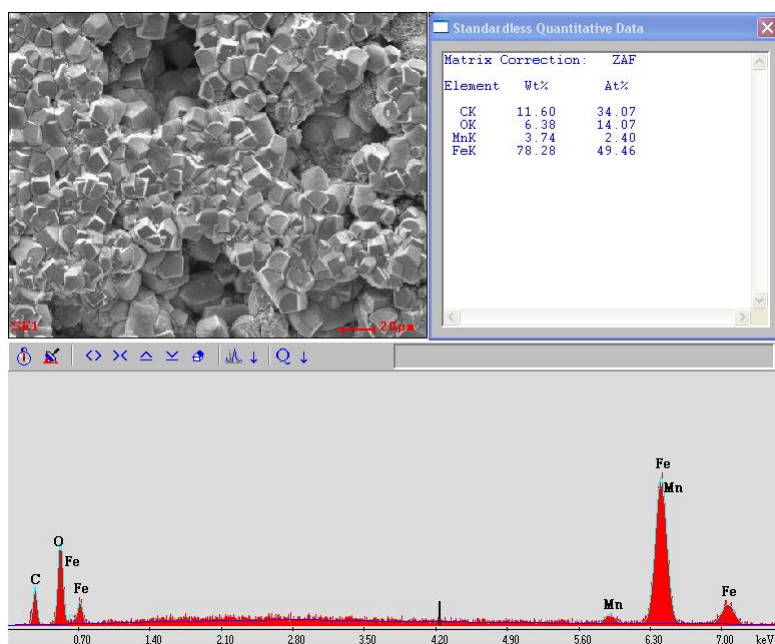


Figure 86: Corrosion product layer composition by EDS at x100 magnification for experiment condition of 70°C and 80 bar of CO₂ in absence of corrosion inhibitor.

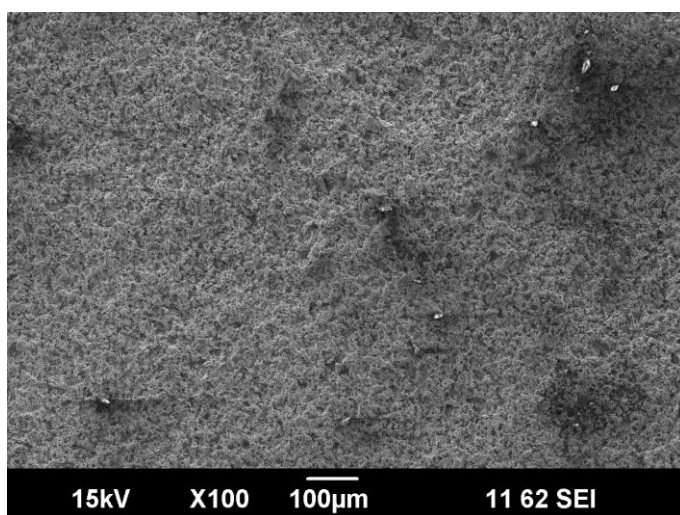


Figure 87: Surface of weight loss coupon at x100 magnification after corrosion product was removed by Clarke solution for experiment condition of 70°C and 80 bar of CO₂ in absence of corrosion inhibitor.

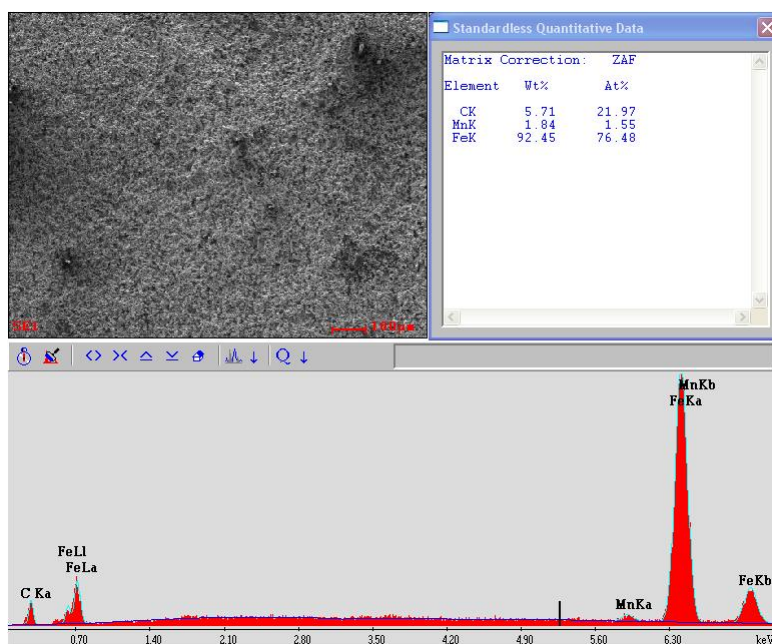


Figure 88: Composition of bare surface by EDS at x100 magnification after corrosion product was removed by Clarke solution for experiment condition of 70°C and 80 bar of CO₂ in absence of corrosion inhibitor.

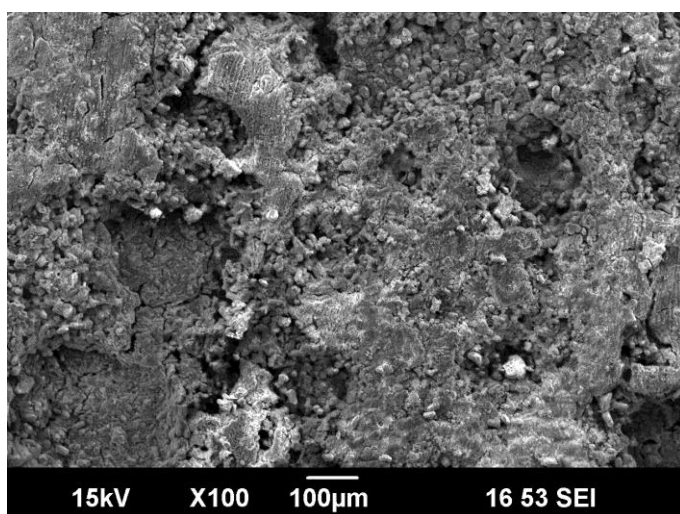


Figure 89: Surface of weight loss coupon at x100 magnification and experiment condition of 70°C, 80 bar of CO₂ and 50ppm of K1.

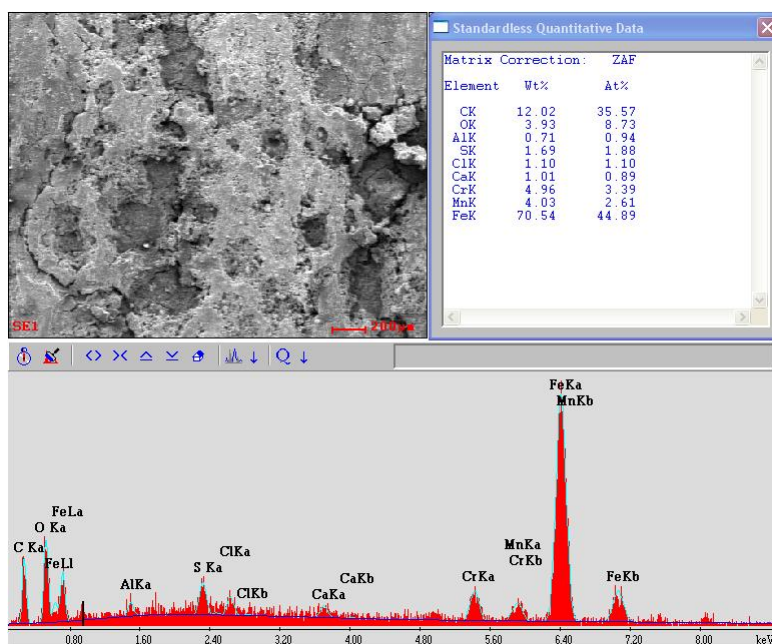


Figure 90: Composition of corrosion product layer by EDS at x100 magnification and experiment condition of 70°C, 80 bar of CO₂ and 50ppm of K1.

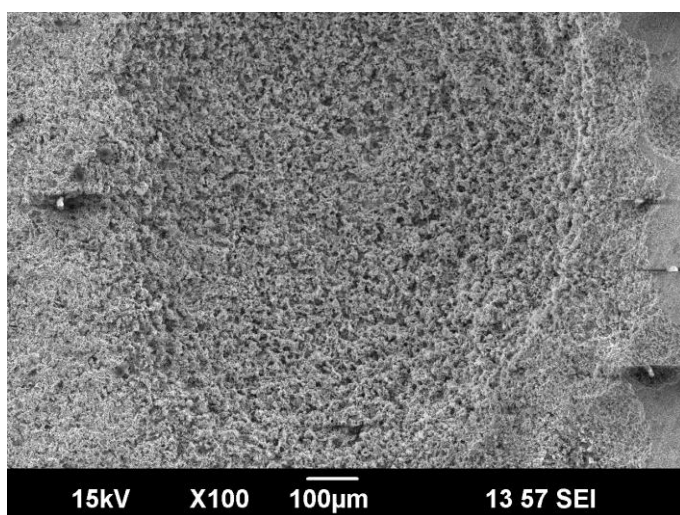


Figure 91: Surface of weight loss coupon at x100 magnification after corrosion product was removed by Clarke solution for experiment condition of 70°C, 80 bar of CO₂ and 50ppm of K1.

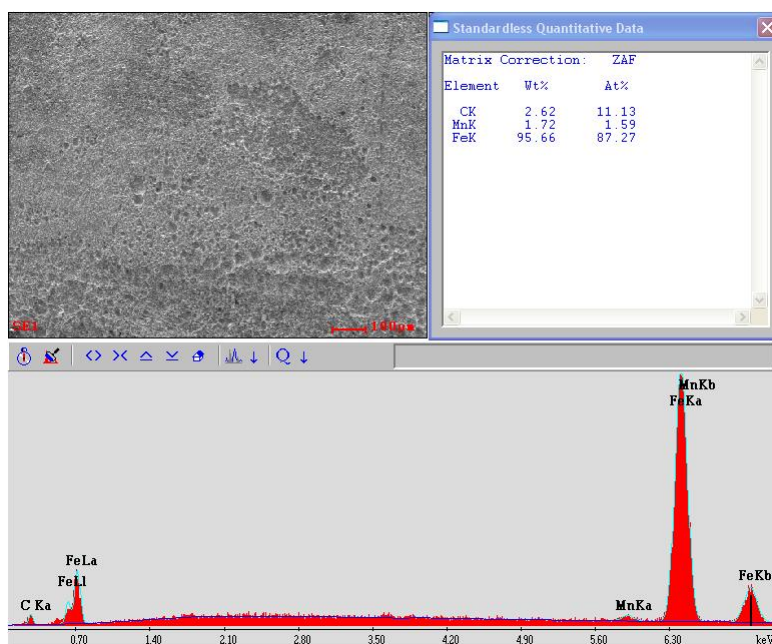


Figure 92: Composition of bare surface by EDS at x100 magnification after corrosion product was removed by Clarke solution and experiment condition of 70°C, 80 bar of CO₂ and 50ppm of K1.

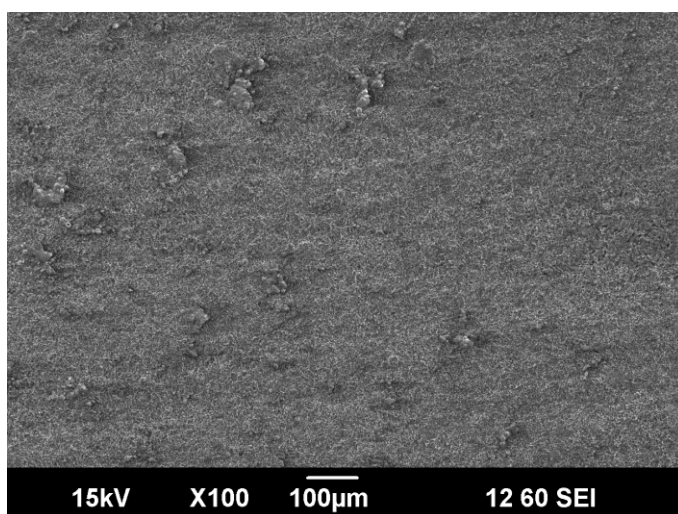


Figure 93: Surface of weight loss coupon at x100 magnification and experiment condition of 70°C, 80 bar of CO₂ and 100ppm of K1.

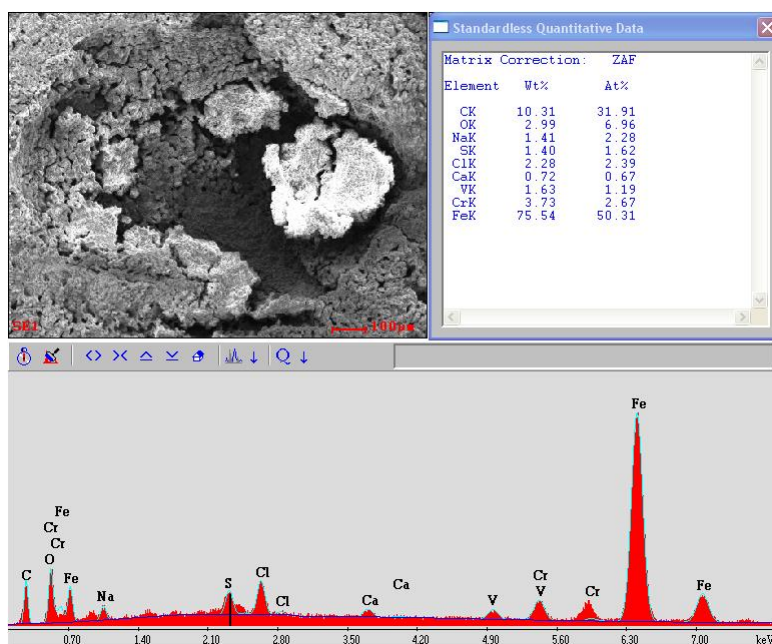


Figure 94 : Composition of corrosion product layer by EDS at x100 magnification and experiment condition of 70°C, 80 bar of CO₂ and 100ppm of K1.

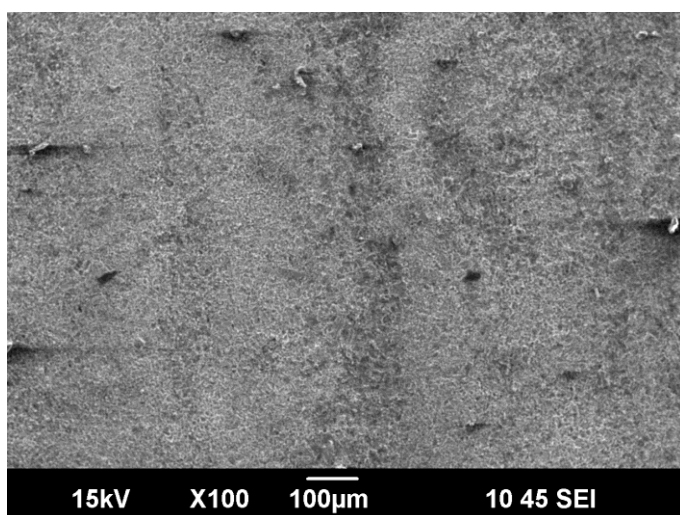


Figure 95: Surface of weight loss coupon at x100 magnification after corrosion product layer was removed by Clarke solution and experiment condition of 70°C, 80 bar of CO₂ and 100ppm of K1.

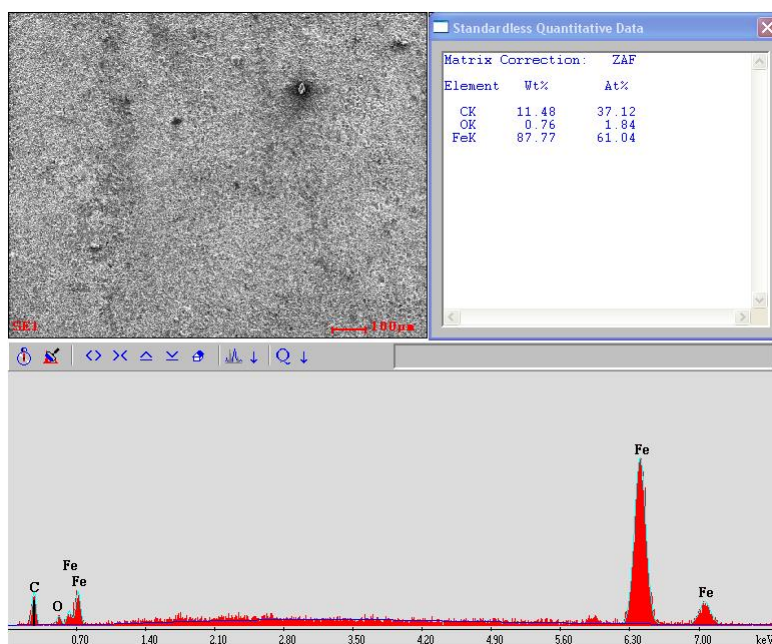


Figure 96: Compositional of bare surface by EDS at x100 magnification after film was removed by Clarke solution. The experiment condition was 70°C, 80 bar of CO₂ and 100ppm of K1.

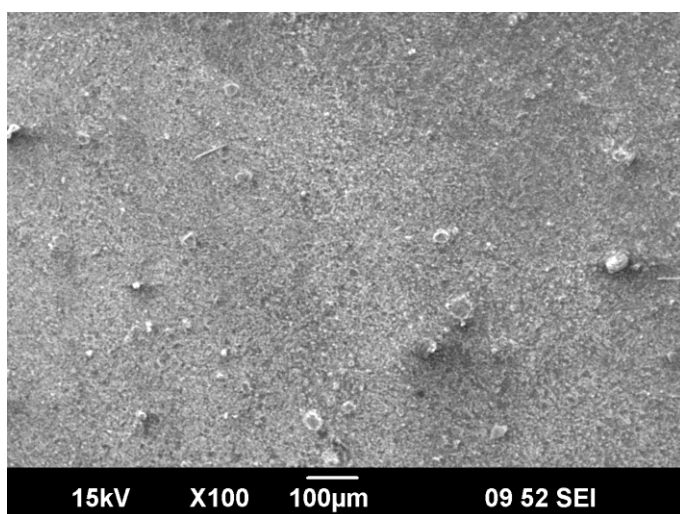


Figure 97: Surface of weight loss coupon at x100 magnification and experiment condition of 70°C, 80 bar of CO₂ and 400ppm of K1.

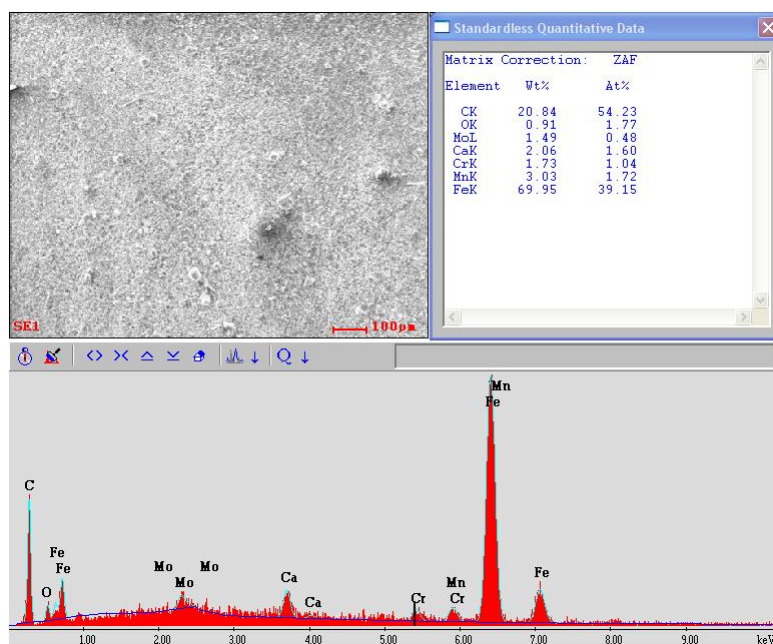


Figure 98: Composition of corrosion product layer by EDS at x100 magnification and experiment condition at 70°C, 80 bar of CO₂ and 400ppm of K1.

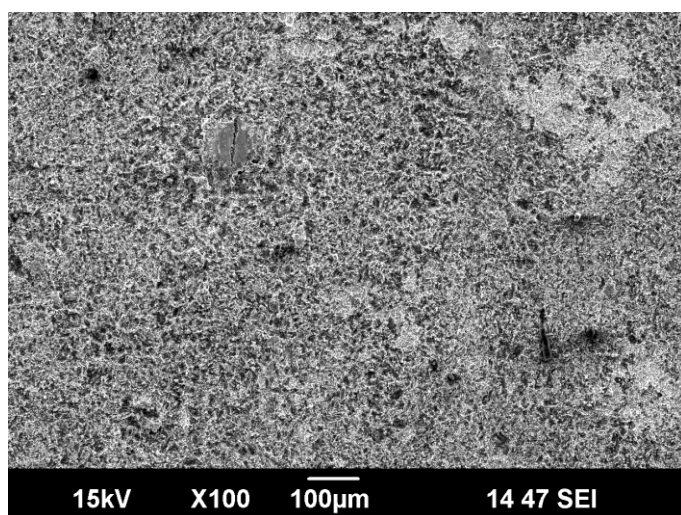


Figure 99: Surface of weight loss coupon at x100 magnification after film was removed by Clarke solution and experiment condition of 70°C, 80 bar of CO₂ and 400ppm of K1.

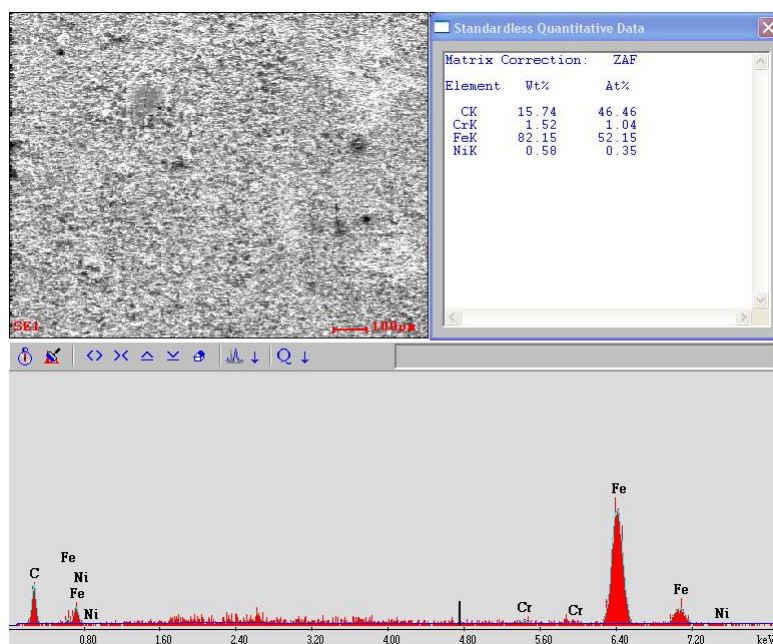


Figure 100: Composition of bare surface by EDS at x100 magnification after corrosion product was removed by Clarke solution for experiment condition of 70°C, 80 bar of CO₂ and 400ppm of K1.

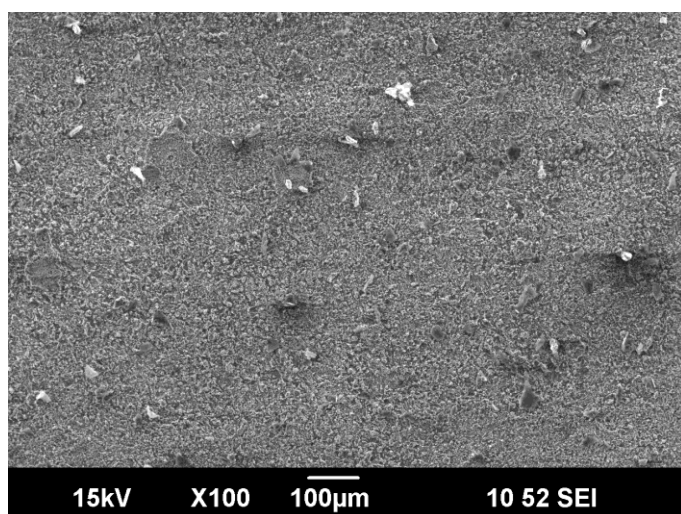


Figure 101: Surface of weight loss coupon at x100 magnification and experiment condition of 70°C, 80 bar of CO₂ and 800ppm of K1.

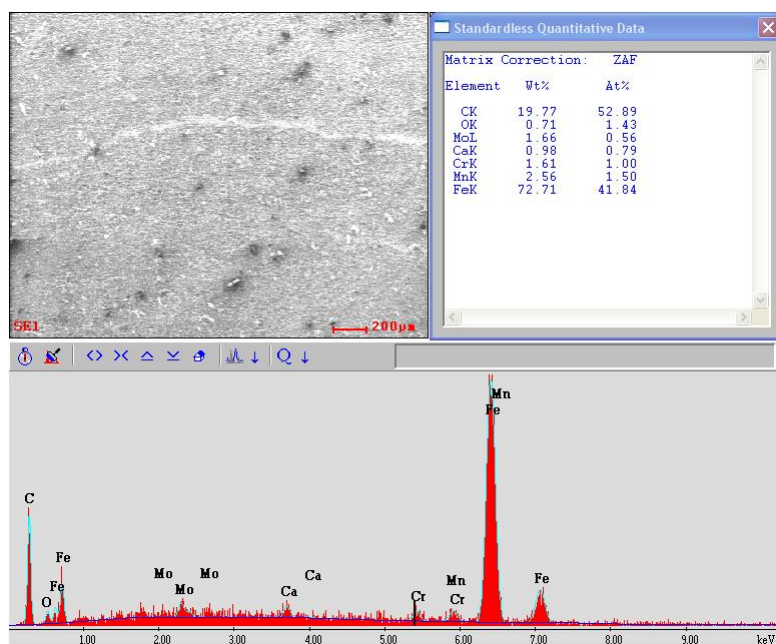


Figure 102: Composition of corrosion product layer by EDS at x100 magnification and experiment condition of 70°C, 80 bar of CO₂ and 800ppm of K1.

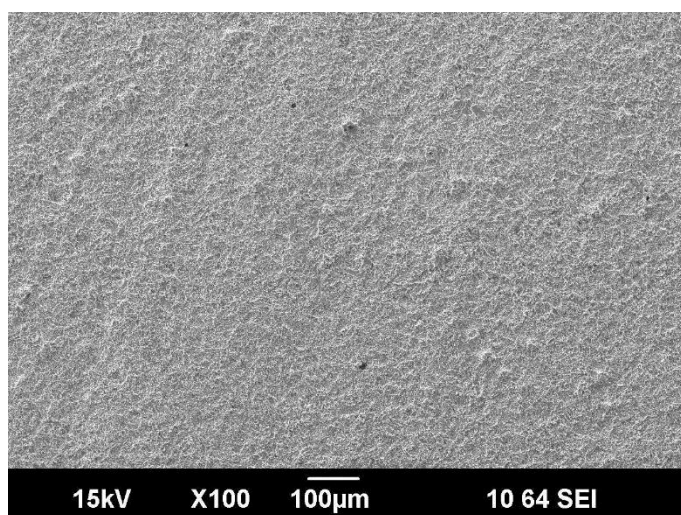


Figure 103: Surface of weight loss coupon at x100 magnification after corrosion product was removed by Clarke solution for experiment condition of 70°C, 80 bar of CO₂ and 800ppm of K1.

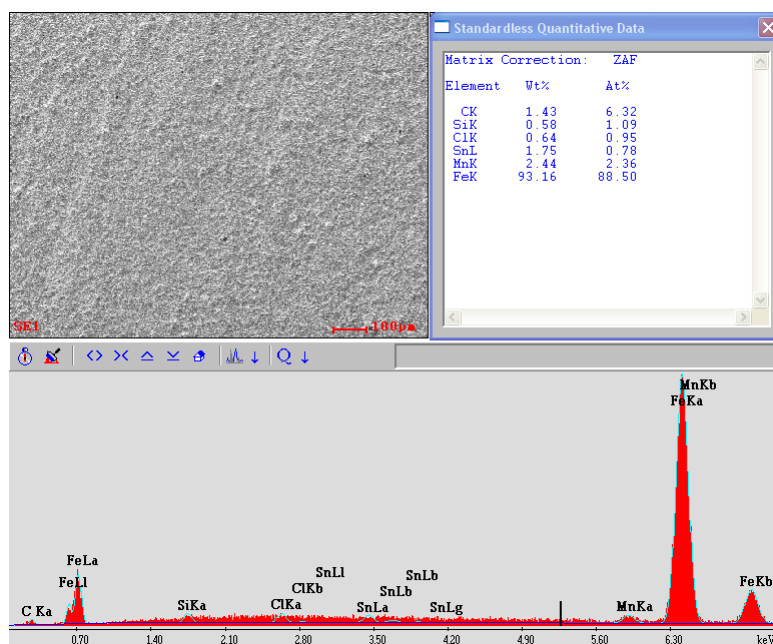


Figure 104: Composition of bare surface by EDS at x100 magnification after corrosion product was removed by Clarke solution for experiment condition of 70°C, 80 bar of CO₂ and 800ppm of K1.

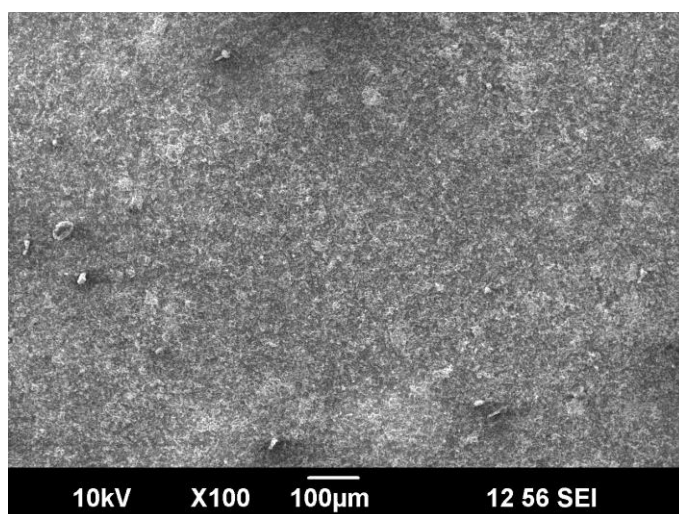


Figure 105: Surface of weight loss coupon at x100 magnification and experiment condition of 70°C, 80 bar of CO₂ and 1500ppm of K1.

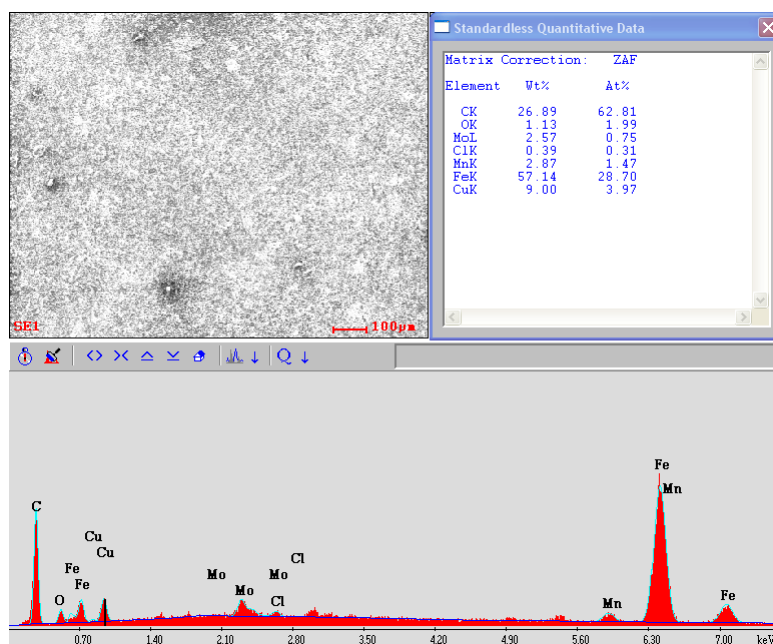


Figure 106: Composition of corrosion product layer by EDS at x100 magnification and experiment condition of 70°C, 80 bar of CO₂ and 1500ppm of K1.

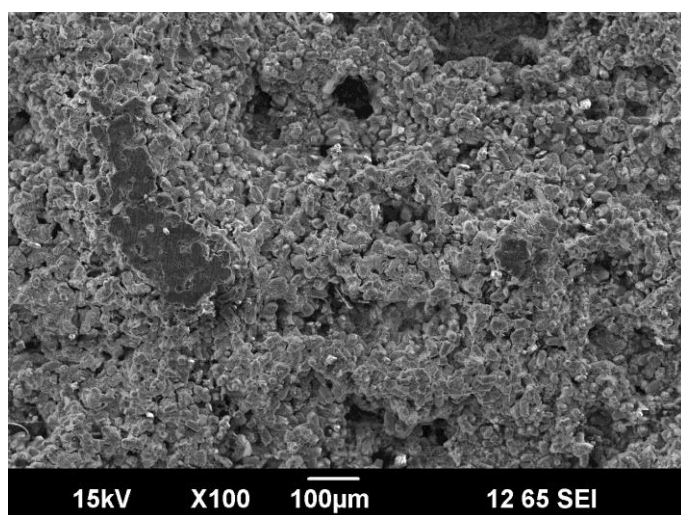


Figure 107: Surface of weight loss coupon at x100 magnification and experiment condition of 70°C, 80 bar of CO₂ and 50ppm of K4.

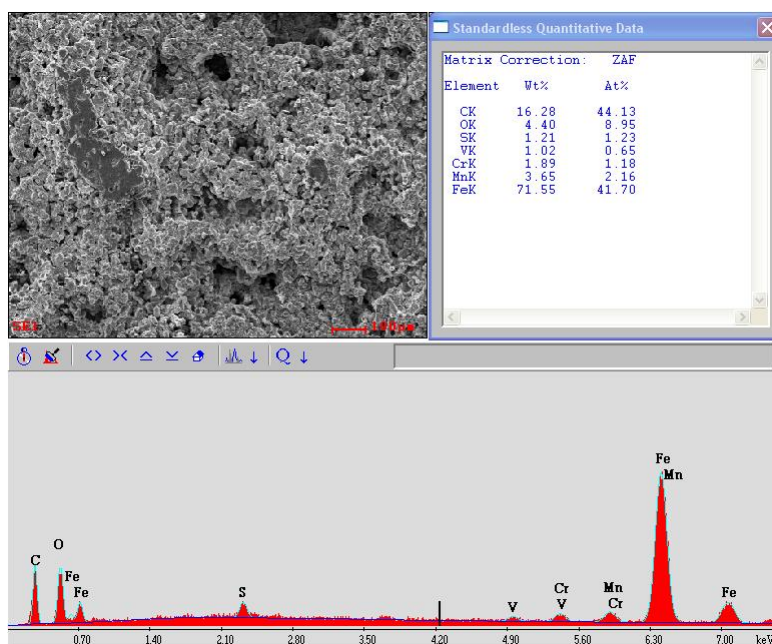


Figure 108: Composition of corrosion product layer by EDS at x100 magnification and experiment condition of 70°C, 80 bar of CO₂ and 50ppm of K4.

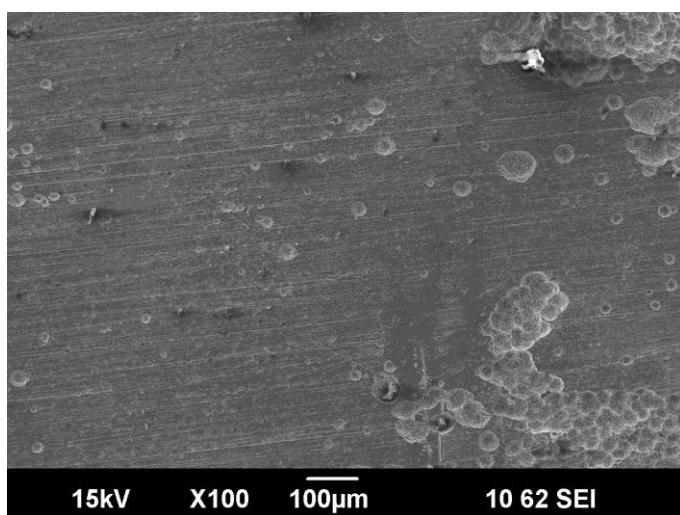


Figure 109: Surface of weight loss coupon at x100 magnification after corrosion product was removed by Clarke solution for experiment condition of 70°C, 80 bar of CO₂ and 50ppm of K4.

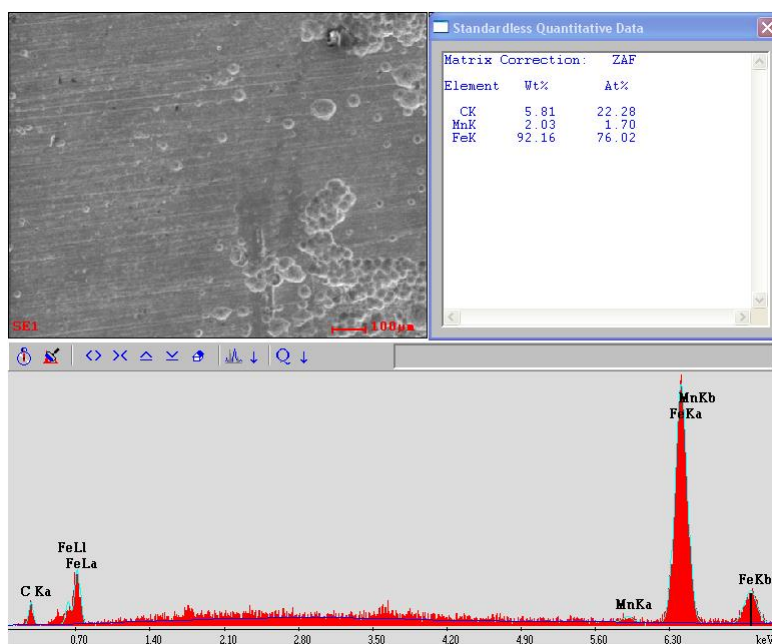


Figure 110: Composition of bare surface by EDS at x100 magnification after corrosion product layer was removed by Clarke solution for experiment condition of 70°C, 80 bar of CO₂ and 50ppm of K4.

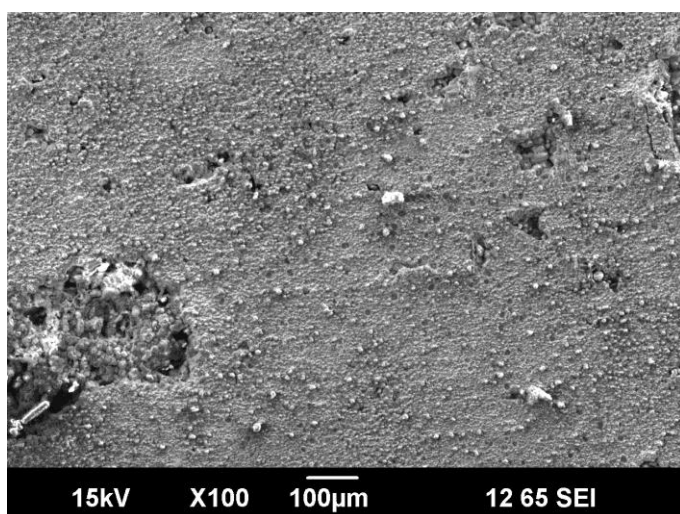


Figure 111: Surface of weight loss coupon at x100 magnification and experiment condition at 70°C, 80 of CO₂ and 100ppm of K4.

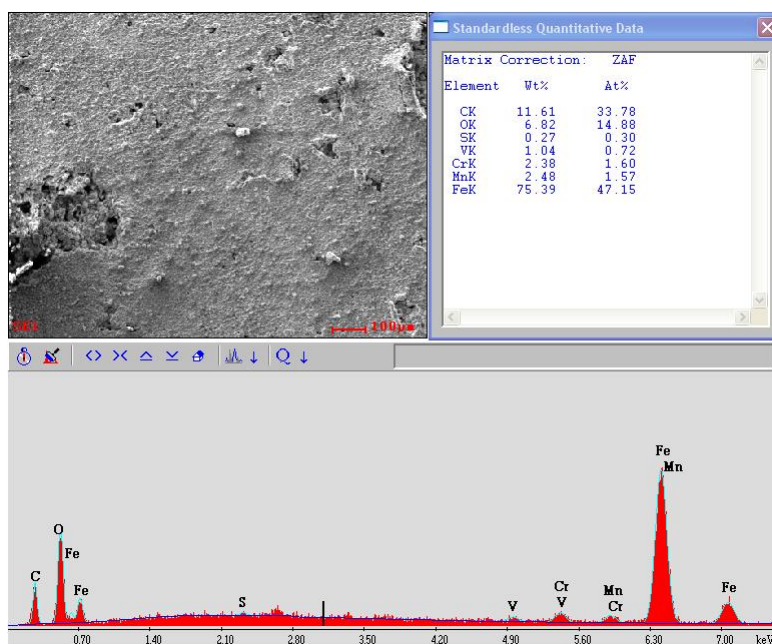


Figure 112: Composition of corrosion product layer by EDS at x100 magnification and experiment condition of 70°C, 80 bar of CO₂ and 100ppm of K4.

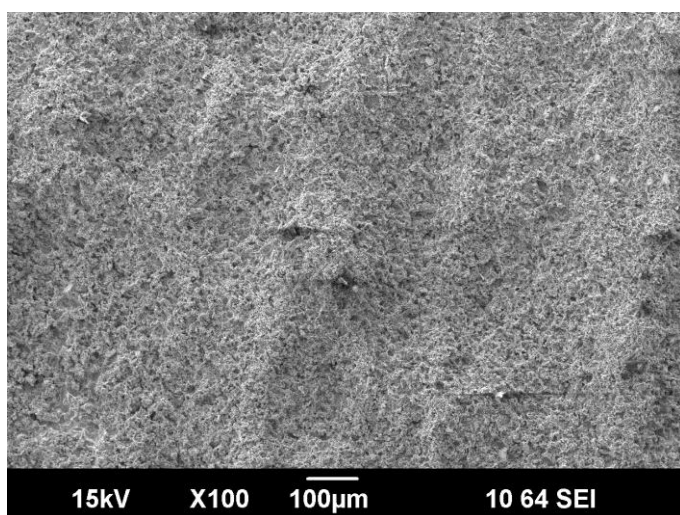


Figure 113: Surface of weight loss coupon at x100 magnification after corrosion product was removed by Clarke solution and experiment condition of 70°C, 80 bar of CO₂ and 100ppm of K4.

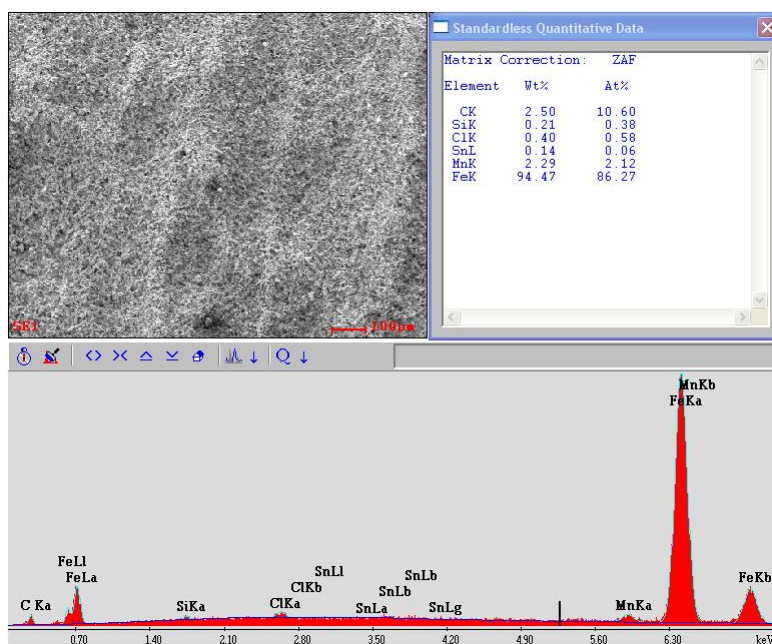


Figure 114: Composition of bare surface by EDS at x100 magnification after corrosion product was removed by Clarke solution for experiment condition of 70°C, 80 bar of CO₂ and 100ppm of K4.

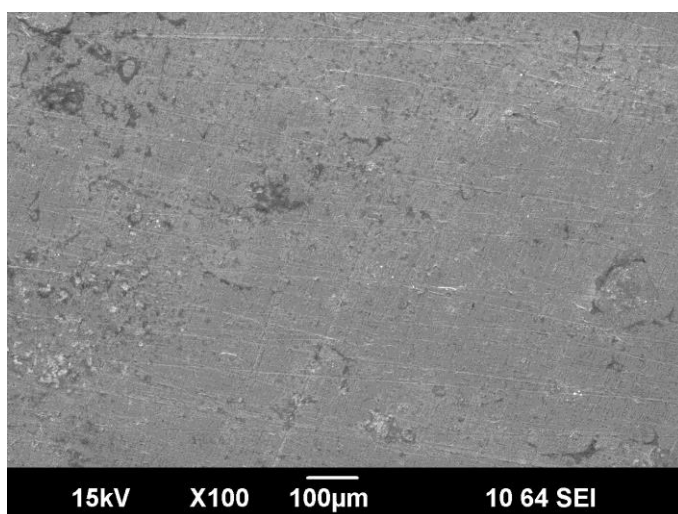


Figure 115: Surface of weight loss coupon at x100 magnification and experiment condition at 70°C, 80 bar of CO₂ and 200ppm of K4.

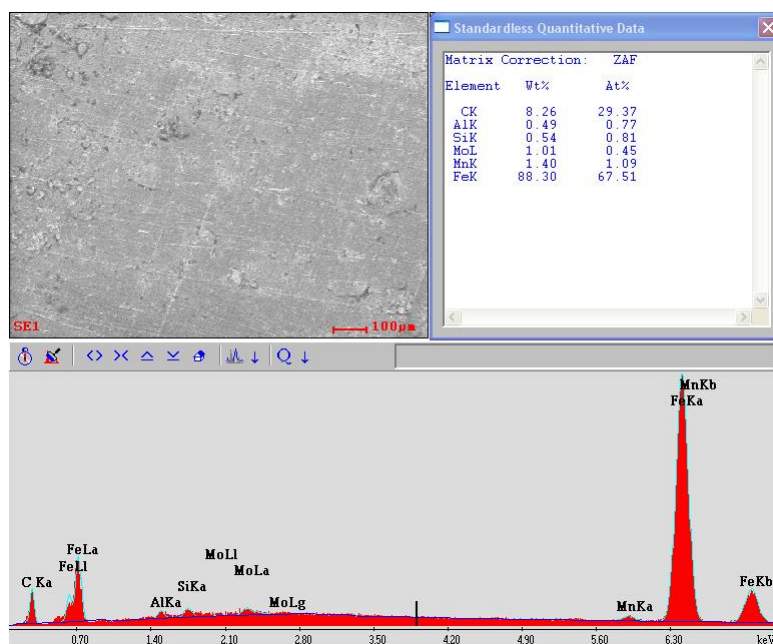


Figure 116: Composition of corrosion product layer by EDS at x100 magnification and experiment condition of 70°C, 80 bar of CO₂ and 200ppm of K4.

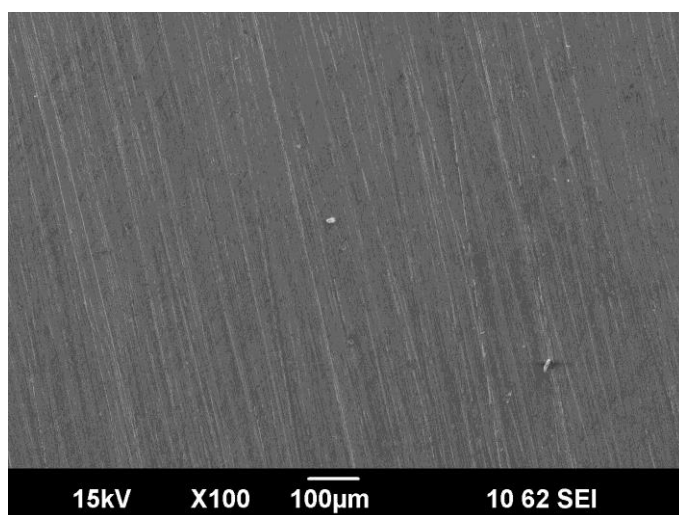


Figure 117: Surface of weight loss coupon at x100 magnification after film was removed by Clarke solution for experiment condition of 70°C, 80 bar of CO₂ and 200ppm of K4.

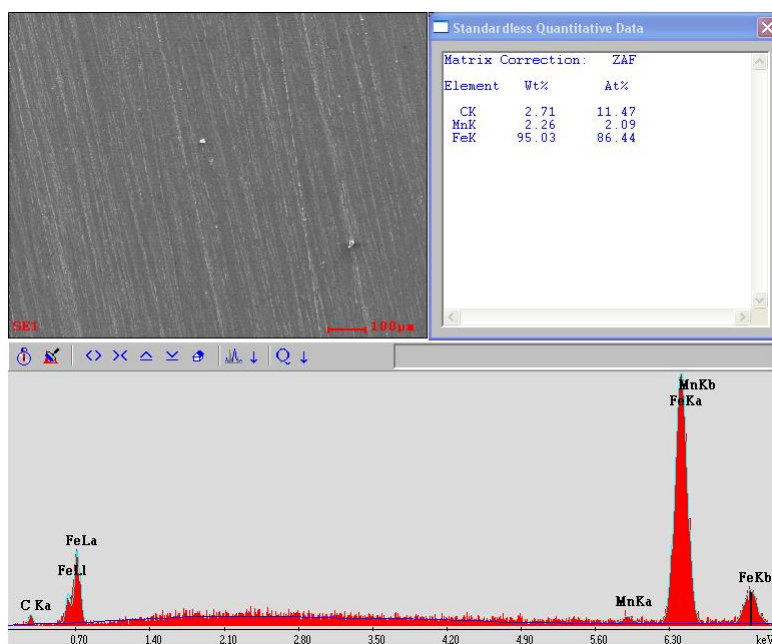


Figure 118: Composition of bare surface by EDS at x100 magnification after corrosion product was removed by Clarke solution for experiment condition of 70°C, 80 bar of CO₂ and 200ppm of K4.

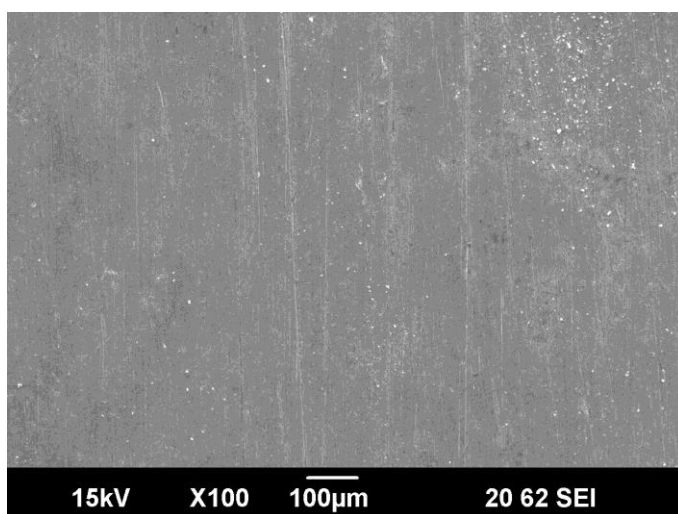


Figure 119: Surface of weight loss coupon at x100 magnification for experiment condition at 70°C, 80 bar of CO₂ and 400ppm of K4.

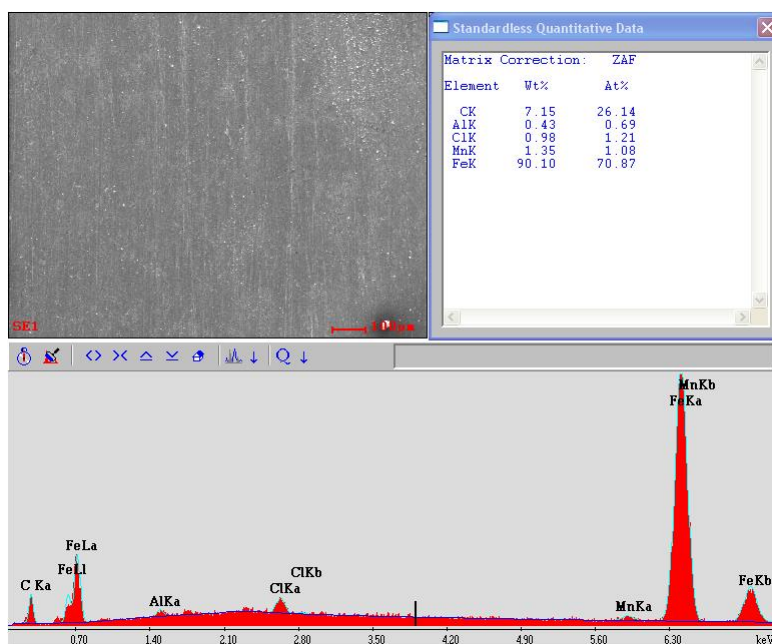


Figure 120: Composition of corrosion product layer by EDS at x100 magnification and experiment condition of 70°C, 80 bar of CO₂ and 400ppm of K4.

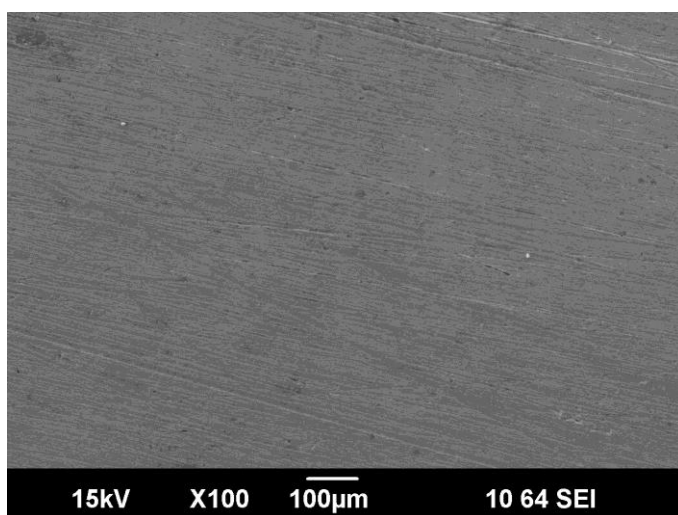


Figure 121: Surface of weight loss coupon at x100 magnification after corrosion product was removed by Clarke solution and experiment condition of 70°C, 80 bar of CO₂ and 400ppm of K4.

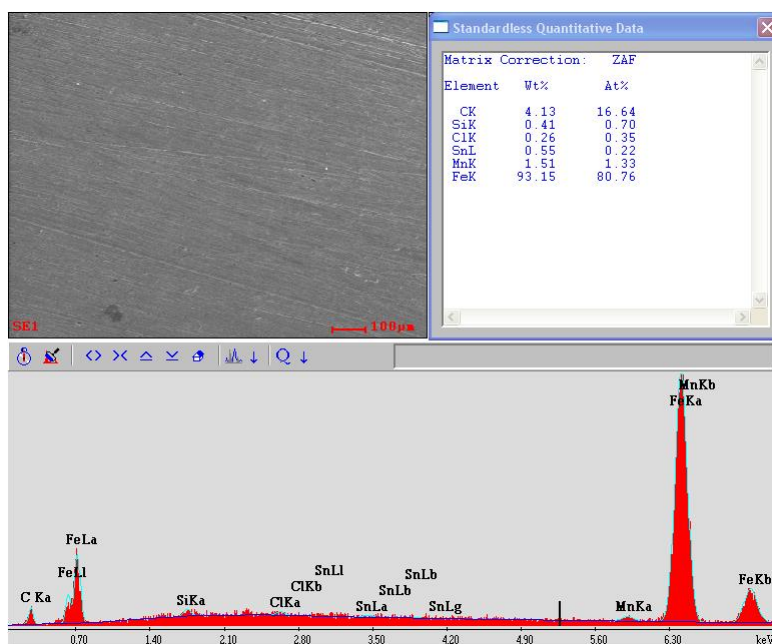


Figure 122: Composition of bare surface by EDS at x100 magnification after corrosion product was removed by Clarke solution and experiment condition at 70°C, 80 bar of CO₂ and 400ppm of K4.



OHIO
UNIVERSITY

Thesis and Dissertation Services